Characterization Study of Plasma Spray Attachment of Intrinsic Fabry-Perot Interferometric Sensors in Power Generation Applications

Amanda R. Krause

Thesis submitted to the faculty of the Virginia Polytechnic Institute and State University in partial fulfillment of the requirements for the degree of

Master of Science

In

Materials Science and Engineering

Gary Pickrell, Committee Chair
Carlos Suchicital
William Reynolds, Jr.

June 11, 2012
Blacksburg, VA

Keywords: plasma spray coatings, fiber optic sensors, attachment method

Characterization Study of Plasma Spray Attachment of Intrinsic Fabry-Perot Interferometric Sensors in Power Generation Applications

Amanda R. Krause

ABSTRACT

The purpose of this study is to characterize the plasma spray deposits used for attaching intrinsic Fabry-Perot interferometric fiber optic strain sensors. The deposits must maintain adhesion at elevated temperatures without distorting the sensors' signals. Two different material systems were tested and modeled, a nickel based alloy and yttria-stabilized zirconia. The material properties of the deposits and the thermal stresses in the system were evaluated to determine attachment lifetime of the sensors. The encapsulated sensors' signals were collected before and after plasma spraying and at elevated temperatures. The material properties of the deposits were evaluated by electron microscopy, energy dispersive x-ray spectroscopy, scratch testing, thermal fatigue testing, and nanoindentation. The thermal stresses were evaluated by Raman spectroscopy and from finite element analysis in COMSOL® Multiphysics®. Several of the sensors broke during encapsulation due to the plasma spray processing conditions and the signals experienced distortion at elevated temperatures. The sensors can be treated to remove this interference to allow for this deposit attachment. The nickel based alloy's ductility and lamellar microstructure allowed for non catastrophic relaxation mechanisms to relieve induced thermal stresses. The yttria stabilized zirconia failed catastrophically at elevated temperatures due its lack of compliance to mismatches in thermal expansion. A high melting point metallic deposit, similar to the nickel based alloy, is desirable for fiber optic sensor attachment due to its ductility, thermal expansion, and dominant relaxation mechanisms. The processing conditions may need to be optimized to allow for the sensors' protection during encapsulation.

Acknowledgements

I would like to thank my adviser Dr. Pickrell for his encouragement and guidance on this project. I have really enjoyed working with him and have learned so much under his direction. I also would like to thank my committee members, Dr. Reynolds and Dr. Suchicital, for their advice and support. I would also like to express my sincere gratitude to the Materials Science and Engineering Department at Virginia Tech and to many of the faculty who have encouraged and inspired me. A special thanks to MesoScribe Technologies, Inc. who has provided funding and is an essential participant in my research.

I would like to thank my research group for their support and help in the laboratory. Specifically, I would like to thank Neal Pfeiffenberger for teaching me how to use COMSOL® and providing constant support. I would also like to thank Brian Scott and Adam Floyd for their help setting up experiments and their recommendations. I would also like to thank Dr. Bodnar and Charles Farley in the Geosciences Department, Steve McCartney at the Nanoscale Characterization and Fabrication Laboratory, and Mac McCord in the Engineering Science and Mechanics Department for teaching me about the characterization techniques and for their time and help on this project. I am grateful to Cheng Ma, Xiaohua Lei, and Tyler Shillig at the Center for Photonics Technology for their help with collecting and analyzing the sensors' signals. I also want to thank Drew Griffith at CSM Instrument for completing the scratch testing.

I want to thank my family and friends, whose moral support and encouragement has helped me tremendously throughout this project. I am very grateful for their help and know that I would not be where I am without them. I would also like to say a special thanks to my parents, Tom and Mickie Krause, my brothers, Thomas and Nathan, and Andrew Doerfler.

Table of Contents

List of Figures

List of Tables

1. Introduction

Fiber optic sensor networks are being implemented in the power generation, aerospace, and building construction industries to obtain accurate and continuous strain data [1-5]. Conventional strain sensors such as resistance or non-contact gages have many limiting attributes and are undesirable due to their size and resolution. Strain gages, which rely on electrical transmission, can be influenced by electromagnetic fields or mechanical vibration. Fiber optic strain sensors do not require electrical transmission but instead rely on light transmission. Silica fibers operate at temperatures up to 800^{o}C while resistance strain gages are limited to temperatures below 350^{o}C [6, 7]. Conventional strain gages are also susceptible to corrosion and prone to brittle failure [2]. In a field test, 26 conventional strain gages and 65 fiber optic sensors were attached to a bridge for strain measurement. After continuous monitoring, 60% of the conventional sensors failed mechanically, but all of the fiber optic sensors remained intact [2]. The silica fibers proved to be flexible and to survive tensile forces in the field. The low loss of commercially available optical fibers makes them the best choice for strain measurement in many industrial applications [8, 9]. The attachment methods for these fiber optic sensors are susceptible to failure [7, 10, 11].

Fiber optic strain sensors need to maintain strong adhesion to the host structure for accurate measurements. The sensors can be implemented by embedding or surface attachment via adhesives, coatings, or mechanical devices [4-7, 12, 13]. All current methods can fracture the fiber during installation and allow for debonding from the host structure during use at high temperatures. Many studies have been completed to improve the bonding of embedded fibers, but little has been reported for optimizing surface attachment methods [2, 5, 14, 15]. Surface attachment can be desirable for process control information and also for ease of access to broken fibers [12]. The surface attachment method should not only maintain adhesion for long term operation in harsh environments but aid in the protection of the fiber. The power generation industry desires surface-attached fibers to aid in process control for

coal-fired boilers. However, very few attachment methods can withstand long term operation under thermal cycling conditions, and the temperature of coal-fired boilers' walls can fluctuate from 25^{o}C to 850^{o}C [16]. Plasma spray coatings have been studied for this purpose due to their application in thermal barrier coatings and strong adhesion to a wide range of surface shapes [5, 17, 18]. Coatings can be made of high melting point materials, including many ceramics and other corrosion resistant materials. The process can be applied to the rounded sides of the fiber and the host structure. However, processing parameters and thermal stresses can result in fiber fracture or detachment [4, 7]. The process must be optimized to maintain strain transfer fidelity for long term use under cyclic thermal loading.

The purpose of this study is to characterize the deposits used for attaching intrinsic Fabry-Perot interferometric fiber optic strain sensors. The fiber optic sensors were fabricated at Virginia Tech and then attached to steel substrates with MesoPlasma™ deposits by MesoScribe Technologies, Inc. The deposit must allow for accurate strain measurement at elevated temperatures. Two different material deposits were evaluated: a nickel based alloy and yttria (8wt%) stabilized zirconia, which have both been used extensively as plasma spray coatings in high temperature applications [18, 19]. The deposits must maintain strong adhesion to both the substrate and the fiber at elevated temperatures without destroying the sensor's signal [11, 12, 14]. The sensor signals were monitored before and after encapsulation and at elevated temperatures to ensure the sensors functionality in the deposits. Raman spectroscopy and finite element analysis calculations were used to assess thermal stresses in the system. The microstructure of the deposits was investigated by nanoindentation and electron microscopy. Scratch and thermal fatigue testing were completed to evaluate the failure mechanisms and the attachment lifetime for both material systems. The material properties and microstructure are important factors for the thermal stress distribution and dominant relaxation mechanisms, which will ultimately determine the operation lifetime of the sensor.

2. Literature Survey

2.1 Intrinsic Fabry-Perot Interferometric Sensors

Fiber optic sensors can provide instantaneous and accurate information while being cost-effective and simple to use [1, 2, 4, 12, 20]. Fabry-Perot interferometric (FPI) sensors have been developed to measure the environmental strain with the use of a cavity that has two reflective surfaces. Light will be partially reflected back from both surfaces toward the source. The two reflected light paths will experience constructive and destructive interference and produce a unique pattern dependent on the length of the cavity. The environmental strain is then measured by changes in the cavity length, which, if multiplied by the index of refraction, is also known as the optical path difference (OPD), which will change the sensor's signal frequency [1, 9, 10]. Extrinsic FPI sensors can utilize an air-filled cavity, because air has a different index of refraction than the fiber material. The cavity is commonly formed by an external tube that aligns the ends of two fibers with an air gap in between. The additional tubing can introduce stress concentrations. Other extrinsic FPI sensors have been designed that utilize different methods to create an air gap [1, 9, 10]. Intrinsic FPI sensors have an internal cavity along the length of the fiber. A single coherent fiber can be formed by fusing multiple fibers together. The end faces are metallically coated before fusion. The metal coatings act as the reflective surfaces along the light path. Changes in the distance between the metal surfaces will cause changes in the OPD, which can be measured to calculate the environmental strain [21]. The signals of FPI sensors are dependent on the reflection properties of each surface, the OPD, and the coupling efficiency of the reflected light back into the core of the fiber. Any fracture or bending at the sensor head can obstruct the signal or limit its resolution [20, 21].

The relative OPD calculation for an FPI sensor is provided by Equation 2.1.

$$OPD = \frac{\lambda_1 \lambda_2}{2(\lambda_1 - \lambda_2)} \tag{2.1}$$

λ_1 and λ_2 are the wavelengths of two adjacent peak locations in the sensor's signal [22]. This allows the OPD to be estimated without the entire interference spectrum. The Fourier transform of the signal can also be used to calculate the OPD by the location of the constructive interference peak. Additional harmonic peaks can be observed in the Fourier transform if the signal is distorted [23].

FPI fiber optic sensors and Fiber Bragg gratings have been extensively studied for use in industrial health monitoring systems [1, 8, 20]. Fiber Bragg gratings have been considered due to their low production cost but they do not provide the same resolution as FPI sensors [21, 24]. The extrinsic FPI sensors provide strain measurement data that is not influenced by significant temperature or transverse strain. However, the mechanical strength of the fiber is compromised due to stress concentrations at regions of contact with external parts needed to create the air cavity. Intrinsic FPI sensors are also weak at the metallic surfaces and are subject to temperature and transverse strain effects. FPI sensors have been designed that have internal air gaps for reflective surfaces. The air gaps are created by modifying the end faces of fibers by etching before fusing them together. These sensors are not subject to temperature and transverse strain effects or stress concentrations [1, 9, 10, 21, 22]. These fibers are called intrinsic FPI sensors because they have nearly homogenous diameters along their entire length and have an internal cavity.

2.2 Attachment Methods for Fiber Optic Sensors

2.2.1 Embedded Fibers

Fiber optic sensors are either surface-attached or embedded in structures for strain measurement. Embedment is a commonly researched method to enhance the understanding of stress in structures' interior [4, 11, 13, 14, 25]. The method also protects the fibers from corrosive or abrasive environments [2, 26]. Structural components with designed interior fiber optic networks can provide detailed information about the integrity of the structure during its lifetime. However, optical fibers are larger than conventional reinforcing fibers and can introduce stress concentrations into the component [27]. Previous studies show that the stress distribution can be optimized by altering the arrangement and thickness of the

fibers [11, 14, 25, 28]. Results also show that fibers with diameters smaller than125μm have little effect on the strength of the component. The stress concentrations are more likely to cause failure of the fiber or cause debonding at the fiber-host interface [21].

Ceramic and polymer coatings have been utilized for protection and to maintain adhesion for embedded fibers. However, these coatings can induce cracking and fracture due to differences in thermal expansion [11]. Broken embedded sensors are not easily replaced or repaired and, therefore, become useless for data acquisition and may call for reproduction of the structural component [1, 4, 12, 21]. Other surface-attachment methods have been developed for easier access to the sensors and for application in existing structures.

2.2.2 Ceramic Adhesives

Brush-on adhesives have been employed to surface-attach fiber optic sensors for strain measurement [4-7, 29, 30]. Ceramic adhesives can be used at high temperatures, allow for easy application and provide good contact with the host structure. But the fracture toughness of these ceramic materials limits the adhesion lifetime. The systems will exhibit cracking and buckling due to differences in thermal expansion with the host structure. These failure mechanisms will cause poor strain transfer fidelity prior to detachment [4, 7, 11, 29]. Researchers are continuing to strengthen these adhesives and make their thermal expansion coefficients (CTE) more compatible by using additives, such as SiC whiskers [6, 29].

Henkel studied an alumina cement to attach a fiber optic strain sensor to a titanium alloy substrate. The sensor reported reproducible strain measurements during five cyclic thermal loads, where the maximum temperature was 600^{o}C. The brush-on technique allowed for a homogenous application of the adhesive around the fiber and good contact with the substrate. Henkel also reported that the cement was prone to cracking and very brittle. Any fiber movement would cause fracture and detachment of the fiber [5]. Wnuk et al. also investigated ceramic cements for attachment of optical fibers and reported accurate strain

data at high temperatures. High silica content ceramic cements were chosen for this study to prevent low CTE mismatch with the silica fiber [6].

The adhesives are easy to use and apply, although requiring several days for room temperature curing [4, 6, 29]. They are known to provide reproducible strain measurements in high temperature applications but have not been tested for long term use [5, 30]. The brittle nature and low bond strength of these adhesives makes them less desirable for long term operation. Polymer adhesives and epoxies have been used extensively but will not be discussed in this paper since they are restricted to low temperature applications [3, 6, 28].

2.2.3 Mechanical Application

Optical fibers have been attached mechanically with use of brackets or other support systems [2]. These methods allow for simple, in-field installation to existing structures. However, the brackets for reproducible results can be very complicated, and some require fiber surface treatment [7]. Mechanical attachment is not often studied due to poor strain transfer fidelity and because it can be intrusive [4, 11].

2.2.4 Plasma Spray Coatings

The plasma spraying process is used as a fiber optic sensor attachment method because of its versatility with different materials and shaped surfaces [4-7]. The coating provides better adhesion than any other attachment process because it uses chemical and mechanical bonds [31].

Henkel also investigated the use of plasma spray coatings for attaching fiber optic sensors. After thermal loading, delamination was observed under the fiber, as seen in Figure 2.1 [5].

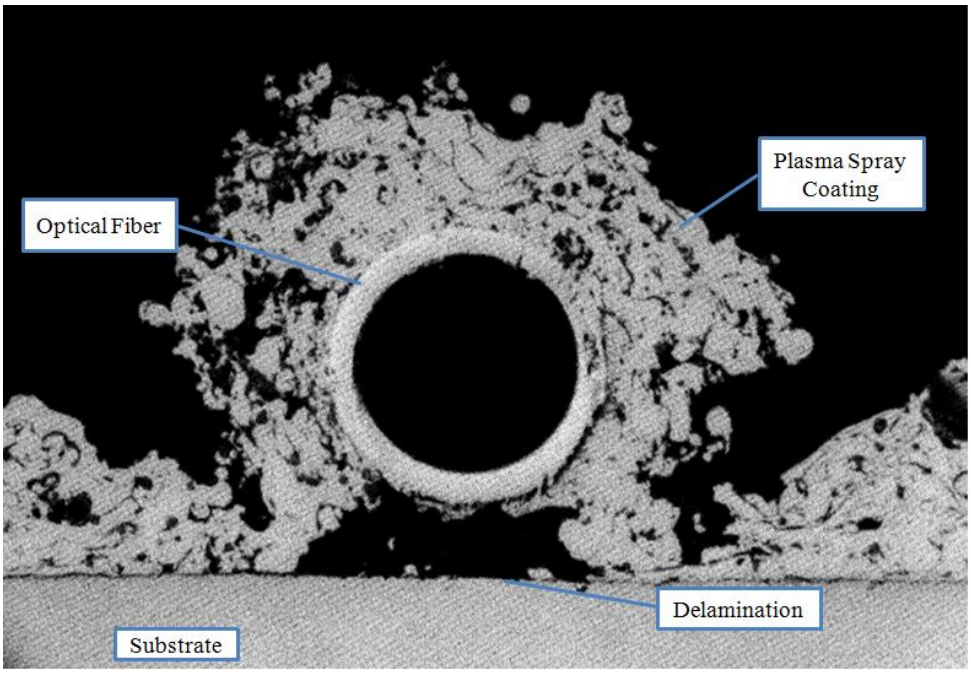

Figure 2.1: Image of an optical fiber attached by a plasma spray coating onto a titanium substrate. [Obtained from Henkel [5]. Modified by author. (Used under fair use, 2012)].

The plasma spray coating by Henkel had not been optimized and cracks and delamination have occurred causing the sensor to produce unreliable measurements. Plasma spray coatings are at risk for delamination from thermal loading due to a common CTE mismatch between the coating and the substrate. These thermal stresses and failures will be discussed in more detail in following sections.

Plasma spray coatings exhibit superior adhesion with the host structure compared to brush-on ceramic and polymer adhesives. However, the spraying process commonly causes fiber fracture [4, 7]. The destructive nature of the coating is caused by method's high velocity particles. Particles are melted, propelled and solidified onto a substrate at a rate of millions of particles/cm^2/s [18, 32]. A diagram of the plasma spray process is seen in Figure 2.2.

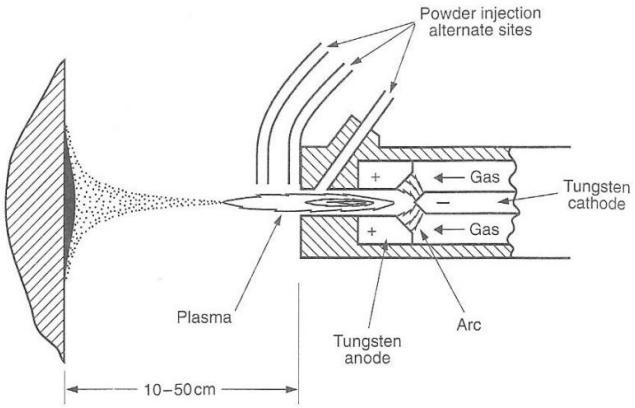

Figure 2.2: Schematic of the plasma spraying system. [Obtained from Stern [18]. Modified by author. (Used under fair use, 2012)].

The plasma spray gun creates an arc from a direct current that energizes an inert gas to the plasma state. The plasma plume then propels the feed powder toward the substrate while melting the powders [17, 18, 33]. There are many processing parameters that can be altered to control the quality of the coating, including the feed rate, current, spray distance, and the substrate temperature [32, 34-38]. These have been extensively studied and will not be discussed in this paper.

Plasma spray coatings are built by the repetition of powders splattered across the substrate surface [17, 18, 32-34, 38, 39]. The morphology of a splattered particle can be seen in Figure 2.3.

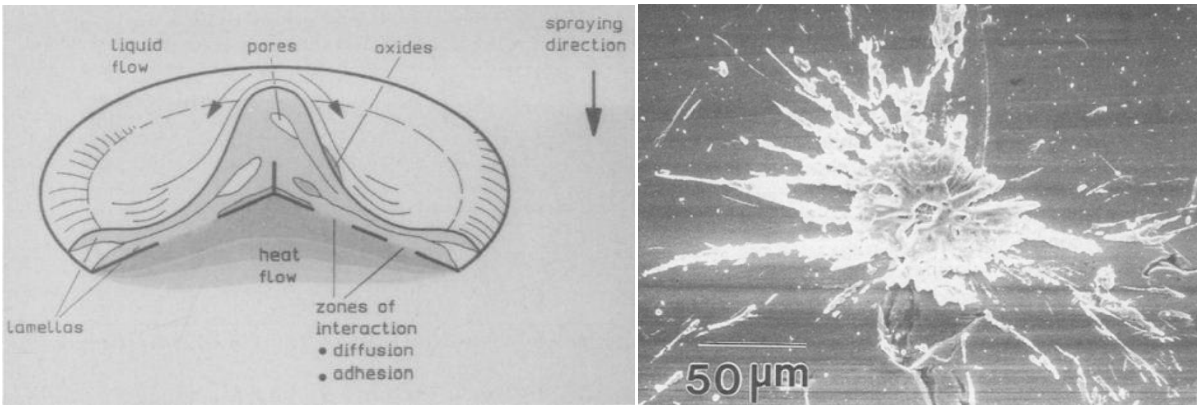

Figure 2.3: A (a) schematic [34] and (b) SEM image [32] of the morphology of a single splat produced by plasma spraying. [Obtained from Steffens et al. and Sampath et al. Modified by author. (Used under fair use, 2012)].

The splat structure is dependent on the extent of melting of the particle. Fully melted particles are well spread out and can contain pores depending on the material's viscosity [17, 18]. The splats can also deform the substrate at certain processing conditions as seen in Figure 2.4.

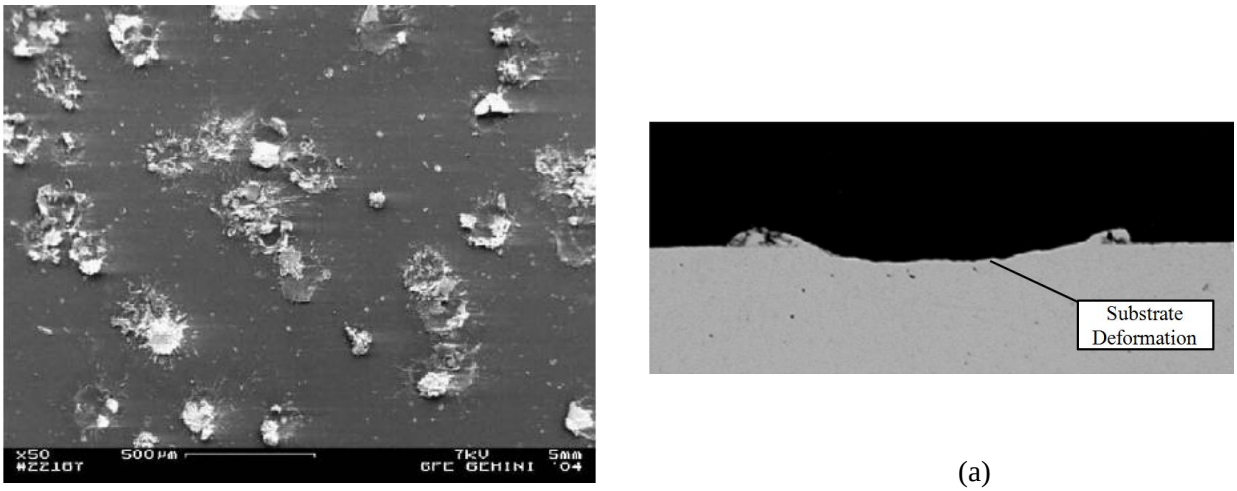

(b) (a)

Figure 2.4: Deformation of a Mg alloy substrate by plasma spraying Ni-5Al powders. The figure (b) is a cross section view of a splat seen in (a). [Obtained from Parco et al. [35]. Modified by author. (Used under fair use, 2012)].

Parco et al. reported that the substrate temperature and feed rate can control the extent of substrate deformation [35]. The processing parameters and materials can be altered to reduce the damage and produce well-adhered splats.

The splats build on top of one another to produce a lamellar structure parallel to the surface of the substrate. The cohesion of the lamellar structures is also dependent on processing parameters [32, 33, 36]. For this paper, adhesion will refer to the interfacial forces between the coating and the substrate and cohesion will refer to the interfacial forces between splats within the coating [18]. Figure 2.5 (a) shows a schematic for how the microstructure is formed.

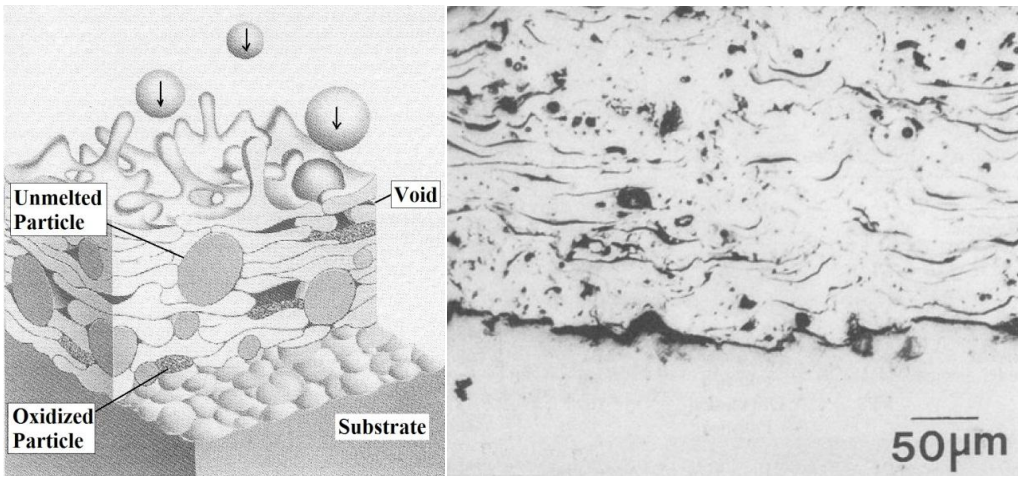

(a) (b)

Figure 2.5: A (a) schematic of lamellar microstructure produced from plasma spraying and (b) an SEM image of a cross section of a nickel plasma sprayed coating. [Obtained from Stern [18]. (Used under fair use, 2012)].

The lamellar microstructure is an important factor for the failure of the coatings because they control the formation and direction of cracks [40-43]. The interlamellar voids and porosity also play a large role in the material's relaxation mode under high stress.

Fiber attachment can be difficult because the high velocity particles cause the fiber to move during spraying. Previous researchers have found that restraining the fiber is necessary to allow for attachment by this method [5, 6]. Fracture of the fibers during processing must be minimized and the coating must provide protection and resist fracture during thermal loading. The processing parameters should be altered to produce the optimum porosity and lamellar structure to reduce thermal stresses.

2.3 Quenching and Thermal Stresses in Plasma Spray Coatings

2.3.1 Thermal Stresses Induced by Thermal Expansion

The common source of failure in plasma spray coatings in high temperature applications is thermal stresses imposed from a CTE mismatch [7, 18, 19, 44, 45]. Coatings are often ceramic or metallic materials with lower CTE values than the substrate material. These coating materials are chosen for the application due to their better durability at elevated temperatures and ability to protect the underlying

substrate or host structure [18, 33]. Therefore, a large CTE mismatch may be unavoidable at the coating-substrate interface.

During heating, the substrate is expanding faster than the coating. This puts the coating in radial tension at the interface and the substrate in compression. During cooling, the substrate is contracting faster than the coating, which imposes a compressive stress on the coating and a tensile stress on the substrate [44, 45]. The stress from the mismatch can be calculated with the following expression, Equation 2.2, for a thin coating,

$$\sigma_{\Delta T} = \Delta T \cdot \Delta\alpha \cdot \frac{E}{1-\upsilon} \tag{2.2}$$

where ΔT is the difference between the temperature after cooling and the strain-free reference temperature, $\Delta\alpha$ is the difference in CTE between the substrate and the coating, and E and υ are the elastic modulus and Poisson's ratio, respectively, for the coating [46].

The maximum stress is experienced at the substrate-coating interface and then dissipates in magnitude with increasing distance from the interface [47]. Figure 2.6 shows the thermal stresses measured by Matejicek et al. by neutron diffraction along the cross section of a plasma-sprayed NiCrAlY 460 coating on a steel substrate [45].

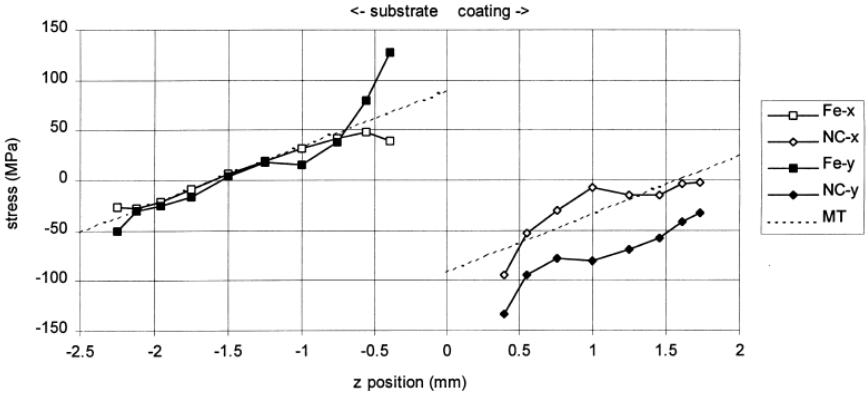

Figure 2.6: Stress data from a NiCrAlY 460 coating on a steel substrate measured by Matejicek et al. at room temperature using neutron diffraction. The stress is reported for both the x and y directions. [Obtained from Matejicek et al. [45]. (Used under fair use, 2012)].

After cooling, the stress profile shows the maximum stress at the interface with the coating in compression and the substrate in tension. The magnitude of these stresses can be significantly high and cause failure if they are greater than the adhesion or cohesion strength [44]. A temperature change of 100^{o}C has reported to induce stresses as high as 100MPa in metallic coatings [48]. The stress profile is controlled by the material properties, the temperature gradient, relaxation mechanisms and the thermal history [44, 47, 49, 50]. The relaxation mechanisms and residual stresses from processing will be discussed in more detail below.

Functionally gradient coatings have been formulated to decrease thermal stress but the CTE mismatch is still present between each layer [19, 51, 52]. These systems are more complicated to understand due to gradients in both mechanical and thermal properties.

2.3.2 Residual Stresses from Plasma Spraying

The plasma spray process induces stresses in the coating that control the thermal response and cyclic lifetime of the system. Residual stresses result from two main thermal events during processing: rapid solidification of the particles and cooling to room temperature after spraying [19, 44, 45, 47, 53]. The particles experience rapid cooling on the order of 10^{6}-10^{8} K/s as they hit the substrate [32]. The heat from the particles is transferred and dissipated into the substrate upon impact causing the particle to cool quickly [50]. The coating is then put into tension because the substrate limits the contraction possible [45]. Each subsequent layer also experiences a tensile force upon impact but at lower magnitudes due to the imposed temperature gradient. The temperature gradient develops from differences in thermal conductivity between the metal substrate and the coating material. The solidification rate of each particle depends on the temperature of the previously deposited layer [19, 47, 53]. Some systems can have measured temperature gradients as great as 600-1500 ^{o}C/mm [39]. Therefore, this quenching stress is greatly determined by this temperature profile and the material properties of both the coating and the substrate. Chemical reactions at the interface can also control the cooling rate. This is more prevalent in

metallic coatings since ceramic coatings on metal substrates are mostly bonded by mechanical forces [47]. Several models have been derived to calculate the stress based on curvature measurements. Stoney developed the following equation, Equation 2.3, to measure the quenching stress of the coating at h_d distance from the substrate-coating interface,

$$\sigma_q(T_s) = \frac{E_s(T_s)h_s^2}{6} \cdot \frac{\delta}{\delta h_d}\left(\frac{1}{R}\right) \tag{2.3}$$

where $E_s(T_s)$ is the elastic modulus of the substrate at the temperature of the substrate and h_s is the thickness of the substrate. R is the radius of curvature and is measured experimentally from a bend test [48]. Most of the models based the calculations off of experimental data due to the complexity of the system. Equation 2.3 shows the influence of the substrate's dimension and material properties on the residual stress.

The second thermal event is the system cooling to room temperature after the spraying process is complete. The cooling process develops thermal stresses from the CTE mismatch that counteract the tensile quenching stresses. The residual stresses are therefore a combination of thermal stresses from the rapid solidification of the particles and the CTE mismatch. The final stress state is dependent on the material system and processing conditions. Processing conditions, especially substrate temperature and deposition rate, can be altered to change the magnitude of the quenching stress. A residual tensile stress state is caused by extreme quenching stresses. A compressive final state is common in systems with a large CTE mismatch [19, 44, 45, 47, 53]. The final stress state plays a large role in the failure mode of the coating system.

2.3.3 Relaxation Mechanisms and Failure Modes

The relaxation mechanisms are dependent on the material properties and stress state. The thermal stresses exceed the adhesion or cohesion strength of most systems and therefore drive the material to relax or fail. Figure 2.7 shows many different plasma spray coating relaxation mechanisms. Systems will often utilize several of these modes to obtain the lowest stress state [42] .

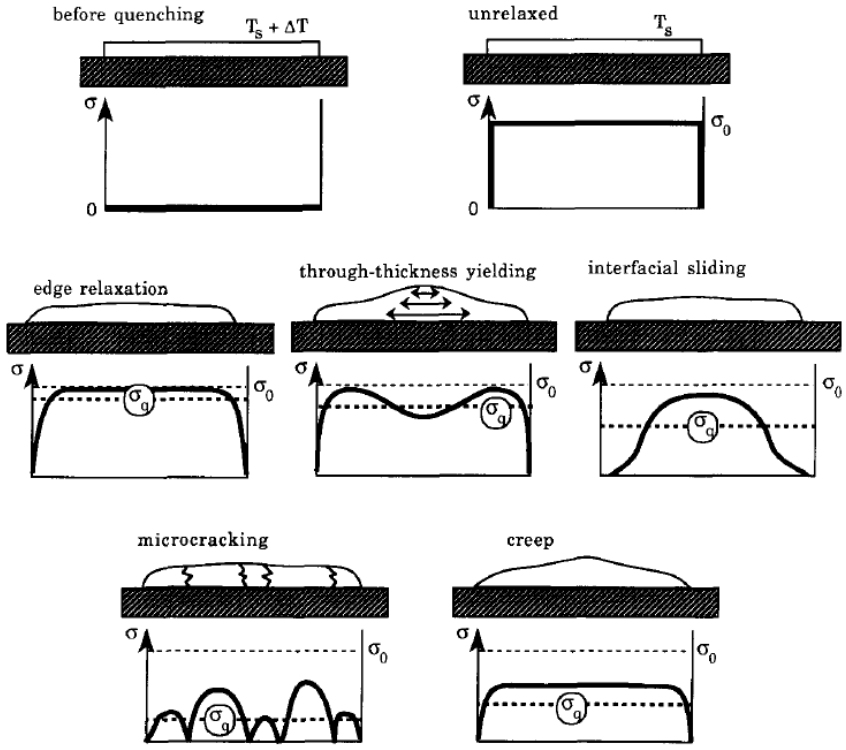

Figure 2.7: Relaxation mechanisms and their effect on the stress states of plasma spray coatings. [Obtained from Kuroda et al. [48]. (Used under fair use, 2012)].

Metallic systems often relax by creep due to the low stresses required for plastic flow at elevated temperatures. An applied stress of 60 MPa generates a creep rate of 1 s^{-1} in nickel at roughly half its melt temperature [48]. Creep will occur at lower temperatures but will require higher stresses to maintain the same rate [45, 52, 53].

Ceramic materials are much stiffer and resist plastic flow at all temperatures. Micro-cracking is often observed for brittle materials during heating and cooling [42, 44, 46]. Kuroda et al. reported that the measured residual stress state of ceramic coatings could not be achieved with micro-cracking alone and attributed the difference in stress to interfacial sliding [48]. Previous reports also show that lamellar sliding is a common relaxation mechanism in plasma spray coatings [29, 41]. Metals can also experience micro-cracking at concentrated stress locations. However, spallation is predominately exhibited in

ceramic coatings and only after either wedge crack propagation or buckling has occurred. Spallation is when part of the material breaks off and is fully removed from the rest of the system. Buckling, during cooling, is caused by radial compressive forces acting at the interface and is dominant in systems with poor adhesion strength. Wedge cracks propagate from the edge of the coating throughout the material to cause delamination. Interlamellar delamination predominantly occurs if the coating's cohesion is weaker than the adhesion strength [48, 53]. The cohesion of ceramic coatings is commonly greater than the adhesion due to the chemical bonding between splats [54, 55]. Therefore, buckling is often observed as the failure mode prior to spallation. Failure modes in a ceramic system are affected more by changes in fracture toughness and the structure of the coating than by changes in the CTE mismatch at the interface [46].

The coating's compliance to differences in thermal expansion is important to resist spallation and other catastrophic failure mechanisms. Pores and vertical cracks have been reported to decrease the stiffness of plasma spray coatings [47, 53]. Vertical cracks are formed perpendicular to the substrate surface by linking interlamellar voids during heating to relax the tensile forces. Cracking parallel to the surface is usually induced by compressive stress [42, 44, 45]. Previous studies have shown that vertical cracks can help stop propagation of parallel cracks and increase the compliance in the system [43, 47]. Therefore, it can be beneficial to allow for tensile cracking during the spray process to increase the lifetime of the coating.

Ceramics at elevated temperatures will undergo cracking because it provides instantaneous relief to tensile stresses. Tang et al. reported that sintering will cause cracking to stop at elevated temperatures and cause the Young's modulus to stabilize [55]. Tensile cracks do not lead to spallation or delamination but can allow corrosive species to enter the system. Pores can act similarly to vertical cracks because they decrease corrosion resistance while being beneficial for diffusion and the compliance of the system. Previous models calculated that increased porosity does not alter the thermal stresses directly [47, 48, 53].

However, they can act as nucleation sites for parallel micro-cracks. The porosity should be optimized to prevent oxidation, corrosion behavior, and cohesion failure but still decrease the stiffness. Stress concentrates at the edges, which are likely to be the location of failure [50].

It should be noted that the substrate can also relieve the stress at the interface by creep or plastic flow [45, 47]. The cohesion strength of the coating will always be less than the yield strength of the bulk substrate so failure will either occur at the interface or within the coating. The thickness of the coating plays an important role for the location of failure and the stress distribution. Delamination is caused from a large stress gradient imposed over the thickness of the coating. Thinner coatings' fracture will be dictated by the adhesion strength of the system and not the lamellar cohesion [42, 54, 55].

Thermal stresses can cause failure in other composite systems as well. Fiber-reinforced materials often experience concentrated stress at the fiber-matrix interface. A stress gradient is observed along the length of the fiber with the maximum stress at the end face. The cavity for the fiber often attracts large densities of dislocations and is a void nucleation site. Delamination of whiskers and fibers is often observed at elevated temperatures from this phenomenon [14, 56].

The residual stresses, thermal stresses and material properties play an integral role in the lifetime of a plasma spray coating. These can be altered and controlled with better understanding of the processing parameters and understanding of the materials behavior at elevated temperatures. The thermal load can also significantly alter the adhesion lifetime but cannot be changed in many applications.

2.3.4 Phase Transformation for Zirconia at Elevated Temperatures

Drastic volume changes can also cause failure in plasma spray coatings. Any system with a crystal structure transformation may cause volume changes that lead to large thermal stresses. Zirconia is a commonly studied material for thermal barrier coatings due to its desirable material properties for

protection of metals in high temperature applications [18]. Pure zirconia experiences a phase change from a monoclinic to a tetragonal crystal structure at elevated temperatures, limiting its use in application. This transformation involves a large volume change, between 3-4%, that can be detrimental to adhesion. A sufficient amount of yttria, and other compounds, can be added to the composition to allow the cubic crystal structure to be thermodynamically stable at all temperatures. The yttria-zirconia phase diagram can be seen in Figure 2.8.

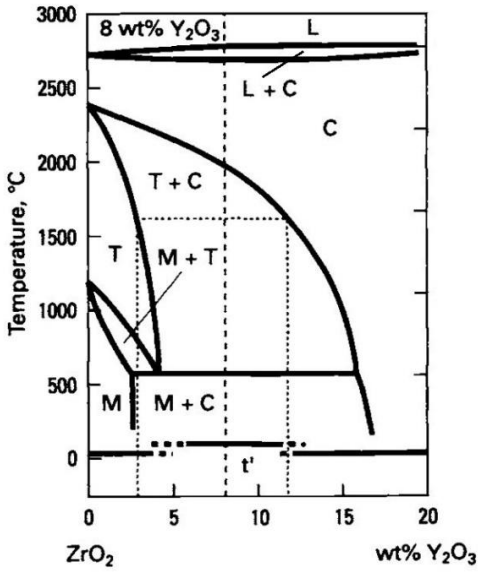

Figure 2.8: The yttria-zirconia phase diagram where C, M, and T are the cubic, monoclinic and tetragonal crystal structures, respectively. The t' is the untransformable tetragonal phase. [Obtained from Taylor et al. [57]. Modified by author. (Used under fair use, 2012)].

The phase diagram shows fully stabilized zirconia is at compositions with over 16wt% yttria because there are no phase transformations prior to melting. The fully stabilized zirconia could be used at higher temperatures without stresses induced from volume change. However, NASA has proven that a composition of 6-8wt% yttria-zirconia produced the best cyclic thermal life for a thermal barrier coating [58]. The volume change is also reduced in this region due to an untransformable tetragonal phase. Under certain processing conditions for compositions within 6-11wt% yttria, the tetragonal phase does not transform to monoclinic but remains in the material as a metastable phase. The compositions with the untransformable tetragonal phase are referred to as partially stabilized zirconia. The tetragonal phase will

not transform by either a thermal or physical driving force [59]. The untransformable phase has the same unit cell as the transformable tetragonal phase but possesses different material properties because of its unique grain structure and different yttria content. The phase is formed by quenching, which produces a very fine grain structure with antiphase boundaries. The phase is believed to be the cause of the increased resistance to thermal fatigue [18]. Figure 2.9 shows the effect of yttria content on the number of cycles to failure for thermal barrier coatings.

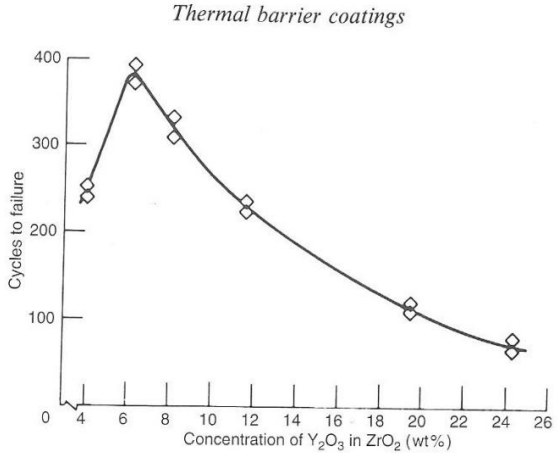

Figure 2.9: Graph of the number of cycles to failure for different compositions of yttria-zirconia thermal barrier coatings. [Obtained from Stern [18]. Modified by author. (Used under fair use, 2012)].

The partially stabilized zirconia compositions are desired for plasma spray coatings in high temperature applications. The thermal stresses of the system can be assumed to be from CTE mismatch and residual stresses for partially stabilized zirconia coatings and not from a volume change.

2.4 Characterization Techniques

2.4.1 Nanoindentation Theory and Practice

Plasma spray coatings are often mechanically tested by nanoindentation due to their size. Nanoindentation techniques measure mechanical properties differently from conventional macro and micro-indentation methods because of the small loads employed. The nano-sized indents require high resolution microscopy for dimensional measurement, which can be time consuming and expensive [60]. Instead, nanoindentors

measure the force and tip displacement during an applied load to produce load vs. displacement curves. The curves are then used to analyze the system for plastic and elastic behavior. The hardness is calculated by Equation 2.4.

$$H = \frac{P}{A_c} \tag{2.4}$$

H is the hardness, P is the maximum load, and A_C is the contact area. The contact area is calculated based on the indenter tip shape and penetration contact depth. The measured total penetration depth, δ_T, includes both the plastic (contact) depth, δ_c, and the elastic depth, δ_e. The equations, Equations 2.5 and 2.6, used to estimate the contact area are shown below.

$$\delta_c = \delta_T - \delta_e = \delta_T - \varepsilon \frac{P}{S_u} \tag{2.5}$$

$$A_c = 24.5\delta_c^{\,2} \tag{2.6}$$

S_u is the slope of the unloading curve at the maximum load and ε is a constant determined by the indenter type, specifically ε = 0.75 for a Berkovich indenter. Other equations and models have been proposed to better describe the indenter geometry but were not used in this analysis.

The specimen experiences elastic and plastic deformation during loading and elastic behavior during unloading. Thus, the elastic modulus must be recovered from the unloading curve. The Young's modulus can be calculated from the reduced modulus using Equation 2.7.

$$E_Y = \frac{1-\nu_S^2}{\left(1/E_R\right)-\left(\frac{\left(1-\nu_i^2\right)}{E_i}\right)} \tag{2.7}$$

E_Y and E_i are the Young's modulus for the specimen and the indenter material, respectively, and E_R is the measured reduced modulus. ν_i and ν_S are the Poisson's Ratio for the indenter and specimen, respectively [61].

The loading curve can be used to analyze the fracture modes during indentation because it includes plastic behavior. Discontinuities are indicative of fracture, including cracking, buckling, or detachment in

coatings [61]. Previous work has also been completed on porous ceramic coatings produced by electron beam-physical vapor deposition and show that increased porosity will elongate the loading curve and change the slope [62]. Rough loading curves can also be indicative of pores that are causing irregular displacement with the applied load or may be due to dislocations that are resisting flow [60, 63]. The loading curve is important to understand how to evaluate the resultant unloading curve and understand the corresponding error in the mechanical properties' calculations.

2.4.2 Raman Spectroscopy

Thermal stresses in coatings have been analyzed by numerous non-destructive techniques including X-ray diffraction, neutron diffraction and Raman spectroscopy [49, 64, 65]. Raman spectroscopy can identify molecular bonds by exciting the material with monochromatic light and measuring the frequency of inelastically scattered photons. Rayleigh scattering, or elastic scattering, occurs if the molecules of the material return to their original energy state after excitation. The scattered light is therefore unaffected by the excitation of the material and unusable for analysis. Stokes Raman scattering and Anti-Stokes Raman scattering occur if the molecule does not return to its original energy state after excitation. The difference between the initial and final energy states will change the molecular vibration and cause the scattered photons to change frequency. The change in frequency is specific for material bonds and can be used for chemical and crystal structure identification. Raman scattering is prevalent in covalently bonded materials. However, Rayleigh scattering dominates in metals and special equipment is often required to produce useable Raman spectra [66].

Raman spectroscopy has also been used to identify residual stresses in coatings. Frequency shifts have been reported when straining materials experimentally. The shifts are attributed to bonds stretching and bending and have been used to calculate elastic strain. Due to the lateral resolution of the technique it has often been used to study the stress gradient across the thickness of thermal barrier coatings [49, 53, 67, 68].

2.4.3 Scratch Testing

Coating adhesion is usually measured with pull off methods or tensile tests. However, these methods require many samples and specific sample geometries. Scratch testing, which allows for fewer samples and variable geometry, has become a widely accepted alternative for adhesion measurements [18, 69-72]. The test can be completed by dragging a load across the surface of the coating with increasing force or by completing multiple scratches at singular loads. The former method introduces more error for determining the critical load but is faster and uses less sample material [70]. The residual stresses from production of the coating, stresses from indenting the material, and the shear stress introduced from moving across the surface all contribute to the critical force for failure [18, 71]. The measured adhesion strength is therefore a measurement of the coating system's ability to resist delamination or cracking from a combination of imposed shear and normal forces. The sample can fail by either cohesive or adhesive failure during scratch testing.

The failure mode can be determined by visible cracks caused by the scratch and based on knowledge of the material systems. Figure 2.10 shows the dominate failure modes induced from scratch testing based on the material properties of the coating and substrate.

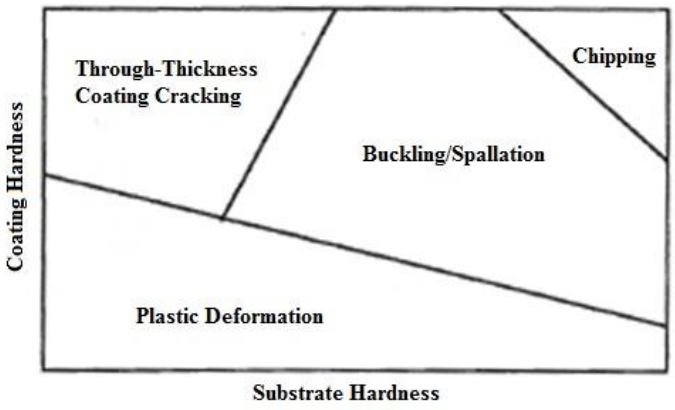

Figure 2.10: The failure modes for a thermal sprayed coating system based on the hardness values of the substrate and coating created by Bull. [Obtained from ASTM Standards [71]. Modified by author. (Used under fair use, 2012)].

The cracks along the surface of the scratch can be used to analyze the type of fracture. Figure 2.11 shows examples of different scratch behaviors induced by different fracture mechanisms.

Type of Failure	Crack Behavior
Through Thickness Cracking or Decohesion	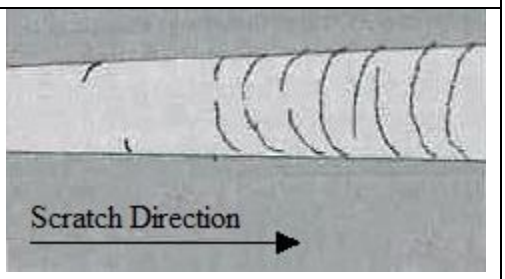
Spallation and Adhesion	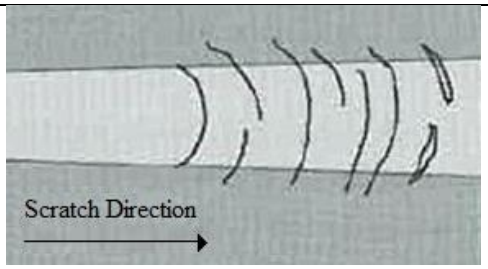

Figure 2.11: The crack behaviors for different types of failure induced from scratch testing according to ASTM C-1624. [Obtained from ASTM Standards [71]. Modified by author. (Used under fair use, 2012)].

Many other cracking behaviors have been observed, and often samples will experience multiple fracture modes simultaneously [71]. The material properties of the coating and the substrate are not the only controlling factors for the failure modes. Residual stresses, which also contribute to the hardness, can induce certain failure modes [69, 73]. The through-thickness cracking and decohesion failure modes will be prevalent in systems in tension and spallation will be dominant under compression. Both the hardness and the residual stress state of the system should be considered when evaluating scratch testing results.

Scratch testing is most commonly reserved for brittle coatings and not often used in the study of ductile coatings. Ductile coatings fail by plastic deformation, as seen in Figure 2.10, which can be difficult to visually inspect. Delamination in ductile coatings is less likely to cause spallation or vertical crack growth [18, 69, 71].

The technique is not the most reliable or accurate because measurements are often determined by visual inspection or from the acoustic signal. Testing parameters such as loading rate or lateral speed and the samples' material properties introduce variability and are important factors in the measurement data [18, 72, 74].

3. Materials and Methods

3.1 Sample Materials and Acquisition

The samples tested were produced by a collaborative effort between the Center for Photonics Technology at Virginia Tech and MesoScribe Technologies, Inc. The fiber optic sensors were created at Virginia Tech and then shipped to MesoScribe Technologies, Inc. for the deposition. The deposits and encapsulated fibers were analyzed at Virginia Tech in the Materials Science and Engineering, Electrical and Computer Engineering, and Geosciences departments.

Fourteen silica optical fibers with an intrinsic Fabry-Perot interferometric (IFPI) sensing head were manufactured at Virginia Tech. The sensors can detect strain at elevated temperatures up to about 700^{o}C depending upon the environmental conditions and can be used for process control data acquisition in power generation facilities such as coal-fired boilers. A detailed description of the fiber fabrication can be found in Appendix A. The IFPI sensors fabricated use internal air gap for reflective surfaces as discussed in Section 2.1.

MesoScribe Technologies, Inc. produced unique coatings called MesoPlasma™ deposits to attach the fiber optic sensors to stainless steel substrates. Two deposit materials were selected for these experiments: (a) yttria stabilized (8wt%) zirconia (YSZ) was selected due to its desirable thermal and corrosion resistance properties and (b) a Ni-based alloy (Ni-(AlMnSi5%)) was also chosen for comparison due to its common use in high temperature applications [33]. Each material was deposited on seven of the fiber optic sensors.

Small brackets were attached along the length of the fiber to hold it in place during processing. A 303 stainless steel substrate was used because it is a relatively common metal for structural components in power generation. The fiber was restrained and protected with a 304 stainless steel tube near the sensor

head. Figure 3.1 is a labeled image of a sample. Each of the deposits is different in thickness and geometry and will be discussed further in Section 3.5. The sensor heads are fully encapsulated within the deposits.

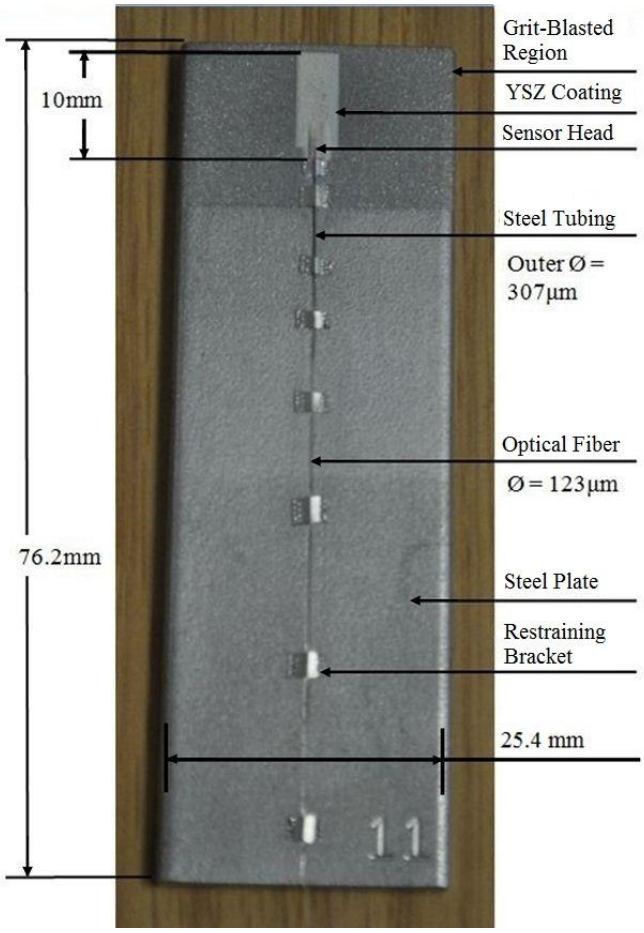

Figure 3.1: Labeled image of a sample with a YSZ deposit to encapsulate the sensor.

3.2 Sensor Spectra Collection

The sensor signals were collected at Virginia Tech's Center for Photonics Technology using a si720 optical sensing analyzer produced by Micron Optics, Inc. The instrument has a swept fiber spectrometer with a 70dB dynamic range, 50nm spectral range, and 2.5pm spectral resolution. The interference pattern was recorded for wavelengths between 1520-1570nm and MATLAB was used to report the signal data

for analysis. The data collection setup can be seen in Figure 3.2. Xiaohua Lei and Cheng Ma, students in the Center of Photonics Technology department, setup the system and helped acquire the spectra.

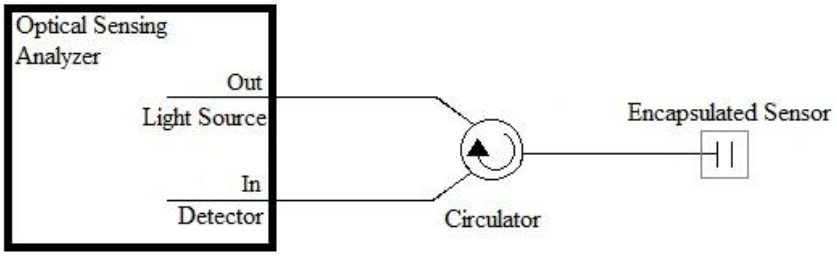

Figure 3.2: Schematic for the sensor signal acquisition setup.

The sensors' signals were collected before and after the plasma spray process. The signals were compared to identify any damage induced on the fiber during processing.

3.2.1 Signal at Elevated Temperatures

The optical spectra of two encapsulated sensors, one of each material system, were collected at elevated temperatures to determine the effect of the thermal stresses on the sensor's function. The samples were heated to 700^{o}C at 100^{o}C increments and with a ramp-rate of 5^{o}C/min. After each heating step, the furnace would dwell for 10 minutes at the set temperature. The heating profile can be seen in Figure 3.3. The samples were then cooled at a maximum rate of -5^{o}C/min. A type K thermocouple was used to report the temperature in the furnace at the time of the data collection. The signal for the Ni-based alloy deposited sample was recorded after the 10 minute dwell period prior to the next heating step. The spectra for the YSZ deposit was collected two or three times during the 10 minute dwell period.

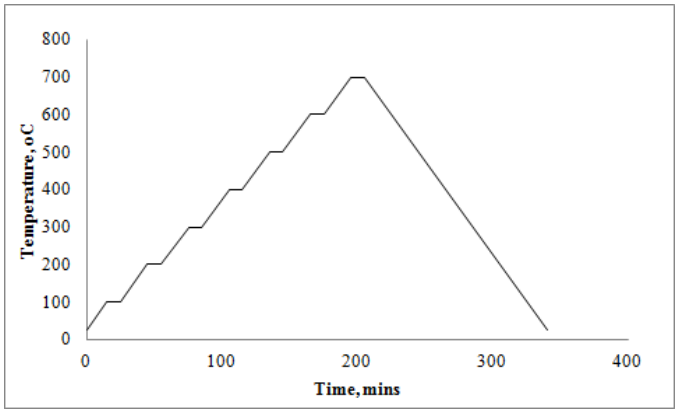

Figure 3.3: Temperature profile of sample during signal acquisition.

The signal from another Ni-based alloy encapsulated sensor was recorded every 10 seconds while under thermal load. The sample was heated to 400^{o}C at 5^{o}C/min and cooled to room temperature with a set maximum cooling rate of -5^{o}C/min. The test was completed to better examine the sensor's behavior at the specified temperature range.

3.3 Thermal Cycling

For the sensor system to be applicable for coal-fired boilers, the deposits need to be able to remain well adhered to both the substrate and the fiber during thermal cyclic loading. A Ni-based alloy sample and a YSZ sample were thermally cycled with a hand-made coil resistance furnace. The coil-resistance furnace was made using Kanthal wire (FeCrAl alloy), which has a resistance of .5210 Ohms/ft and .0402 in diameter (AWG 18). The coil was then cast in Ceramacast™ according to the manufacturer's specifications to set the placement of the coils and prevent a shortage from contact with the metal substrate or itself. A voltage was applied across the wire using a 12 Amp variable autotransformer made by Staco Energy Products Co by attaching alligator clips to both ends of the wire. The voltage was increased every minute to heat up the sample without shorting the fuse. A piece of porous alumina was milled to create a cavity which could fit over the samples and contain the heat. A small hole was drilled through the entire alumina piece to be able to observe the deposit during cyclic loading. A Type K

thermocouple was used with a Eurotherm CN7800 controller to monitor the temperature during heating and cooling. The entire furnace setup can be seen in Figure 3.4.

Each sample was heated to 700^{o}C within 60 minutes and then cooled to room temperature in 30 minutes with the use of convection cooling. The loading was repeated until failure was observed or 20 loads were completed. Previous reports indicate that delaminated regions cool at a slower rate and appear brighter [43, 55]. Therefore, the deposits were observed during cooling to watch for signs of delamination as well as cracking.

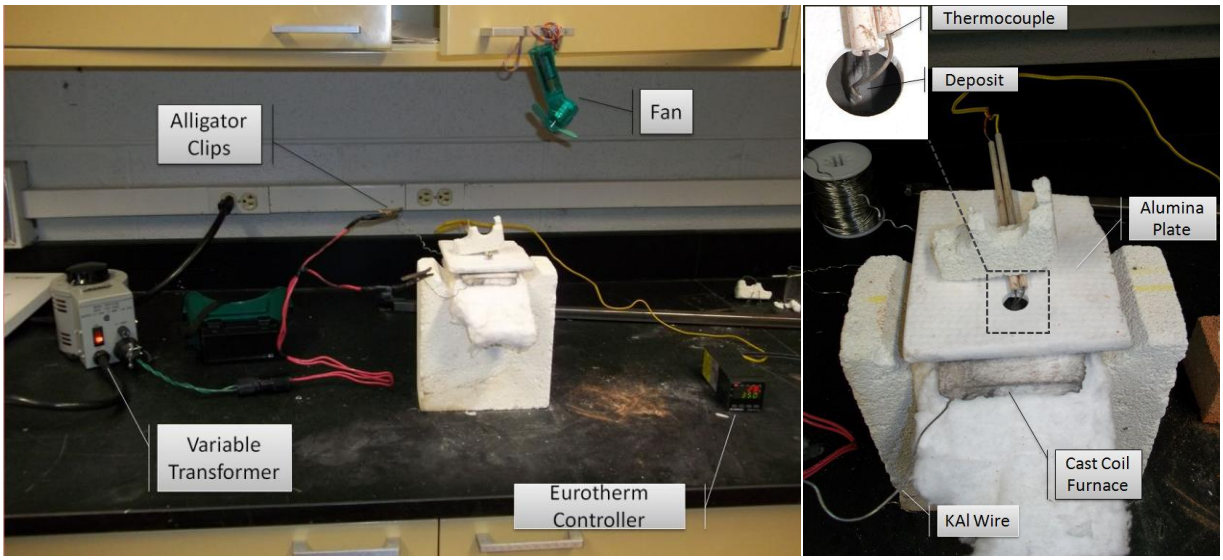

(a)

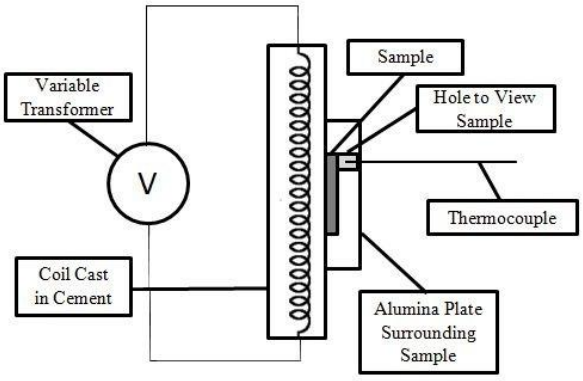

(b)

Figure 3.4: An (a) image and (b) schematic of the coil resistance furnace used for thermal cycling of the samples.

3.4 Characterization

3.4.1Imaging

Scanning Electron Microscopy and Energy Dispersive Photoelectron Spectroscopy

Scanning electron microscopy (SEM) was used to image the cross sections of six encapsulated fibers, three of each material system. The samples were cut with a low speed saw with an alumina abrasive steel blade, mounted in room temperature curing epoxy and then polished with alumina to a 0.3μm finish using standard polishing techniques. The samples were gold-sputtered for 30 seconds. Two of the samples had been heat treated to 700^{o}C to test their signal at elevated temperatures as described in Section 3.2.1.

A LEO (Zeiss) 1550 field emission microscope was used to image the cross sectioned samples. The images were used to measure porosity and investigate the substrate-deposit and the fiber-deposit interfaces. The in-lens secondary electron detector, below the objective lens, was utilized to provide detailed topographic information and is capable of 2-4nm resolution.

Electron Dispersive Photoelectron Spectroscopy (EDS) was used to investigate possible diffusion and identify the chemical species of unique features. Multipoint analysis was conducted at the substrate-deposit interface. The chemical analysis was completed with a Bruker QUANTAX 400 Energy Dispersive X-ray Spectrometer. The EDS system is on a FEI Quanta 600 FEG, an environmental SEM, and images were collected using the backscattered detector.

Porosity Measurements

ImageJ, an image processing software, was used to identify pores and calculate the porosity for both material deposits. Two cross sections that had not undergone heat treatment of each material system were imaged for porosity measurements. Each cross section was evaluated at ten locations to represent the porosity across the entire width and thickness of the deposit. Images were collected at high and low

magnifications with a secondary electron detector, an acceleration voltage of 20kV, and a 9mm working distance. Appendix C describes the porosity calculations completed in ImageJ in more detail. The average porosity was calculated from the images collected at high magnification.

3.4.2 Nanoindentation

The Ni-based alloy and YSZ plasma sprayed deposits were both tested using Micro-Materials LTD – NanoTest in the Engineering Science and Mechanics Department at Virginia Tech. The indents were made with a diamond Berkovich indenter tip and a maximum applied load of 35mN. The maximum load was held for 20 seconds before unloading. During unloading, the sample was held at a low load for a few seconds to calibrate for any change in temperature. The displacement and load were measured during the experiment to produce a load-displacement curve. The maximum load was chosen by experimentation of multiple load ranges on the YSZ deposit sample as described in Appendix D.

A 4x3 (thickness vs. width) point grid, positions 25μm apart in both directions, was superimposed on half of each tested cross section. The grid positions were used to maintain distance between each indent and to determine if the mechanical properties varied across the thickness and width of the deposit. The hardness and elastic modulus were calculated from the measured load-displacement curves as described in Section 2.4.1. The F-test ($\alpha = 0.10$) was used to assess if there was a real difference in hardness or stiffness across the thickness and width of the deposit for both material systems. The reduced modulus was calculated by fitting the slope of the unloading curve from 40-100% of loading values with a power law function.

A 303 steel substrate was also tested by nanoindentation to determine how similar the instrument's results would be to established bulk material values. The maximum load was 100mN for all of the steel indentations and held for 20 seconds before unloading. The substrate was tested at six locations away from any edges.

3.4.3 Raman Spectroscopy

All Raman spectroscopy testing was completed using a JY Horiba LabRam HR800 unit in the Vibrational Spectroscopy Laboratory at Virginia Tech with a 514.32nm Laser Physics 100S-514 argon laser excitation source. All spectra were analyzed using LabSpec-Spectrum software.

Spectra could only be produced for the YSZ deposit because the instrument is not equipped to maximize the signal for metallic samples. Fifteen different locations (five locations across the width at three different distances from the deposit/substrate interface) were tested on the cross sections of an as processed YSZ sample and a heat treated YSZ sample. The cross sections were prepared as described in Section 3.4.1. Each spectrum was collected from 100-600cm^{-1}, with a 2400grooves/mm grating and for either 45 or 60 sec of acquisition time depending on the maximum intensity of the signal. The heat treated cross section was the same sample imaged on the SEM and analyzed using EDS in Section 3.4.1. The temperature profile of the heat treatment is described in Section 3.2.1.

The surface of a YSZ deposit was also tested with Raman spectroscopy at five different locations before and after heat treatment. The spectra were collected from the flat portion of the deposit and not over the fiber due to the technique's sensitivity to rounded surfaces. The same heat treatment as shown in Figure 3.3 was used. The spectrum at each point was collected over the wavenumbers 100-600cm^{-1} with either an acquisition time of 30 or 15 seconds depending on the maximum strength intensity.

3.4.4 Scratch Testing at CSM

Scratch testing was completed to evaluate the adhesion strength and to identify different types of failure for the ductile and brittle coatings. All scratch testing was completed by Drew Griffin at CSM Instruments on a Revetest Macro Scratch Tester with a 200μm-radius Rockwell indenter tip. More detailed testing parameters can be found in Table 3.1. The process was conducted according to the ASTM Standard C1624.

Table 3.1: Testing parameters for scratches made on both material systems.

Initial Load (N)	1
Final Load (N)	200
Loading Rate (N/min)	199
Scanning Load (N)	1
Speed (mm/min)	2.5
Length (mm)	2.6
Acquisition Rate (Hz)	10
AE Sensitivity	9

Only one sample of each deposit material was tested. Two scratches were made on each sample along the thin, flat region of the deposit while monitoring the applied normal load, the penetration depth, the residual depth after the scratch, the friction coefficient, the frictional force, and the acoustic emission. The critical force for adhesion and cohesion failure was determined visually and by changes in the friction coefficient signal. The failure stress (σ_f) for delamination was then calculated using the known geometry of the indenter tip, the width of the scratch at the point of delamination (w) and the critical force (F_c) in Equations 3.1 and 3.2.

$$\sigma_f = \frac{F_c}{A} \tag{3.1}$$

A is the surface area of the indenter in contact with the sample at the critical load. The surface area for the sphere tip can be calculated by Equation 3.2 where R is the radius of the indenter tip.

$$A = 2\pi R\left(R - \sqrt{R^2 - {}^{w}/_{2}}\right) \tag{3.2}$$

The failure stress was calculated for both material systems by the average critical loads and average width of the two scratches.

3.5 Modeling

3.5.1 3D CAD

3D drawings were created on Autodesk® Inventor® and then imported into COMSOL® Multiphysics® 4.2a for analysis. The models will be used to optimize the stress distribution for thermal loading by

investigation of different possible materials and tube lengths. The 3D Inventor® model, seen in Figure 3.5, has the same deposit dimensions determined by SEM. Some of the dimensions can be found in Figure 3.1.

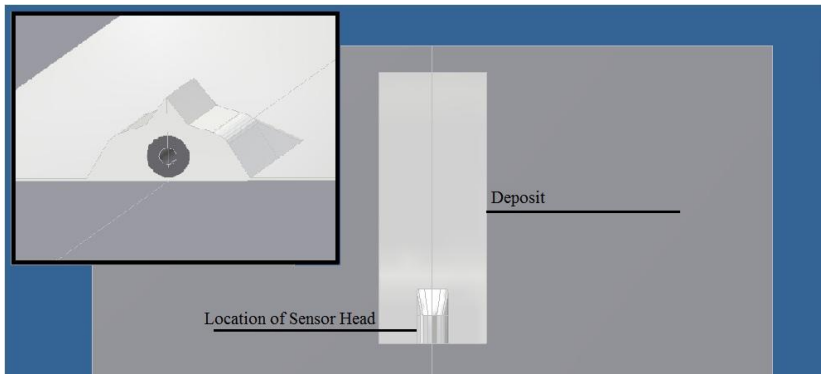

(a)

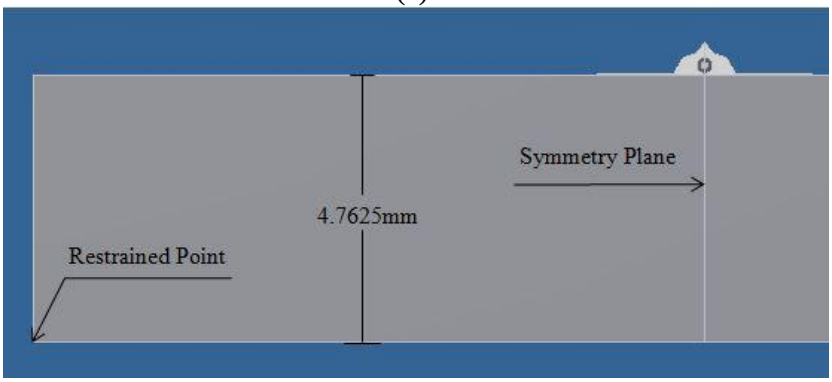

(b)

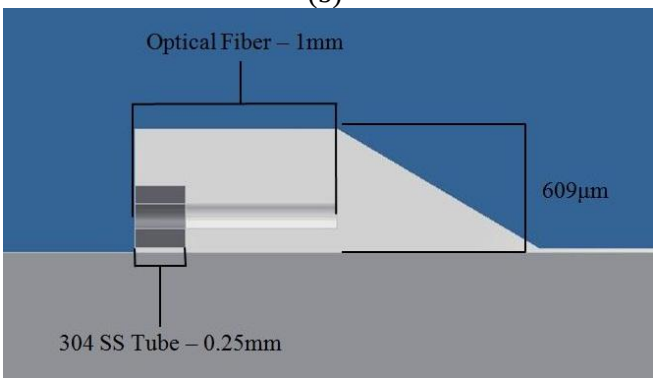

(c)

Figure 3.5: The (a) top, (b) front and (c) right views of the 3D CAD produced in Autodesk® Inventor® to represent the attachment system.

Four different geometries were modeled, each with a different tube length extending into the deposit as seen in Figure 3.6. The heat transfer in solids and solid mechanics modules were utilized in COMSOL® to apply a thermal load and then analyze the von Mises stress due to the CTE differences between the

components. All boundaries were free to move except the point labeled “Restrained Point” in Figure 3.5, which was a fixed point boundary condition. The 3D CAD model was split in half (parallel to the fiber) and a symmetric boundary was applied to reduce computer memory and minimize the amount of time to achieve a solution.

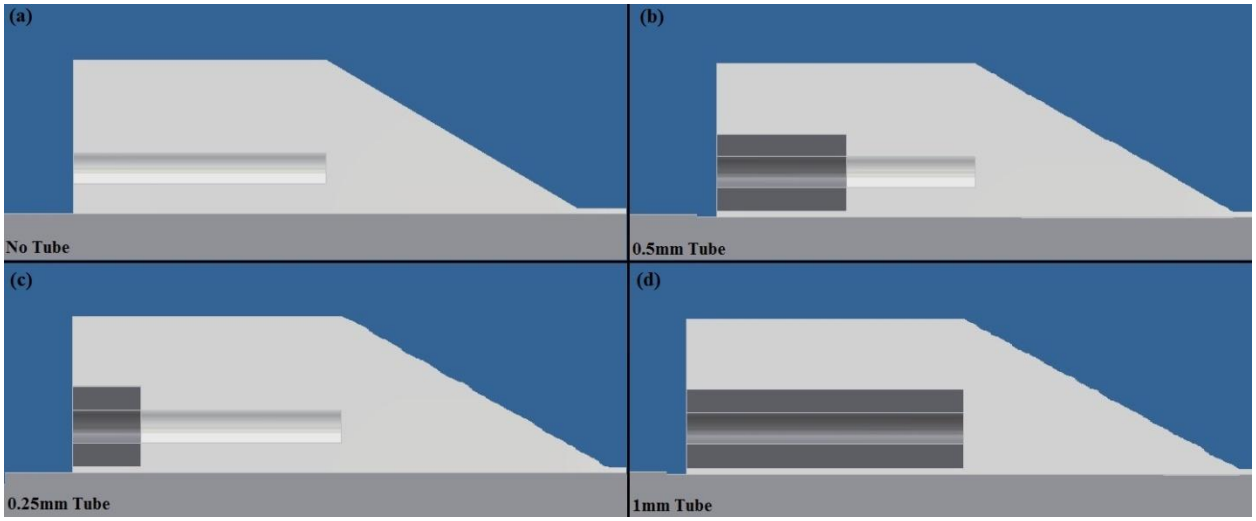

Figure 3.6: The 3D drawings of the four different geometric models: (a) no tubing, (b) 0.5mm tube, (c) 0.25mm tube, and (d) 1.00mm tube.

3.5.2 COMSOL® Thermal Stress Study

The initial temperature for the entire system was set to 25^{o}C. A stationary solver was used to solve for the stresses at 700^{o}C. The temperature was set by applying convective cooling to all exterior faces of the geometry except the end face of the fiber and the tubing, visible in Figure 3.5. The heat transfer coefficient for air was set to 5 W/(m^{2}·K). The stationary solution was used for the initial stress state and other initial boundary conditions for a time-dependent study, which ramped down the temperature from 700^{o}C to 25^{o}C using convective cooling at -5^{o}C/min. The system was solved either with a time step of 1 or 10 seconds for a total of either 13,000 or 23,100 seconds, respectively. Although the air was cooled to room temperature in 8,100 seconds according to the input temperature function, the entire part required a longer time to cool to 25^{o}C.

The stresses along the substrate-deposit interface and around the fiber have the most significant affect on the adhesion and lifetime of the sensor. Edge probes were employed to report the maximum and average von Mises stresses and temperature along these edges during the time-dependent studies.

3.5.3 Material Property Inputs

The material properties for each component were determined from data reported in literature. The CTE and thermal conductivity were defined by temperature dependent functions that were developed by fitting researched data in Wolfram Mathematica® 8. Appendix E shows the computer code used to develop material property functions. All material properties that are independent of temperature can be found in Table 3.2. The CTE and thermal conductivity data for the YSZ deposit was based on the temperature dependent data of a YSZ plasma spray coating of the same composition and similar density [75]. Unfortunately, this information was not available for the Ni-based alloy because this alloy's thermal properties as a function of temperature have not been previously documented. The material properties for the Ni-based alloy were provided by the manufacturer. The material properties that are functions of temperature can be found in Table 3.3.

The heat transfer in solids module requires the thermal conductivity to calculate the temperature of the system resulting from convective cooling. Therefore, the temperature dependent material properties were calculated by a user input predicted temperature that was a function of time. The input temperature function, Equation 3.3, was determined from a model run with constant thermal properties to determine how fast the components cool.

Table 3.2: The material property input data for all components.

Material	Heat Capacity, J/(kg·K)	Density, kg/m^3	Young's Modulus, GPa	Poisson's Ratio
303 SS (Substrate)[1]	500	7810	190	0.33
304 SS (Tube)[1]	500	8000	200	0.29
Silica (Fiber)[2]	703	2203	73.1	0.17
Ni-based alloy(deposit)[1]	523	7850	41.0	0.21
YSZ (deposit)[3]	480	5400	222	0.30

Table 3.3: Temperature dependent functions for CTE and thermal conductivity of the components.

Material	CTE, 1/K	Thermal Conductivity, W/(m·K)
303 SS[1]	$1.34x10^{-14}\cdot T^3+1.04x10^{-11}\cdot T^2+17.6x10^{-6}$	$3.11x10^{-6}\cdot T^2+9.69x10^{-3}\cdot T+12.2$
304 SS[1]	$1.93x10^{-12}\cdot T^2+17.1x10^{-6}$	$3.11x10^{-6}\cdot T^2+9.69x10^{-3}\cdot T+12.2$
Silica[2]	$2.21x10^{-16}\cdot T^3-4.43x10^{-13}\cdot T^2-1.41x10^{-4}/T+9.11x10^{-7}$	1.38
Ni-based alloy[1]	$12x10^{-6}$	29.7
YSZ[3]	$1.40x10^{-10}\cdot T+10.8x10^{-6}$	$-3.22x10^{-13}\cdot T^4+1.97x10^{-9}\cdot T^3-2.53x10^{-6}\cdot T^2+1.71$

[1]Data from Metal Material Data Sheets [76].
[2]Data from Handbook of Glass Properties [77].
[3]Data from study performed by Pawlowski et al. on porous YSZ plasma spray coatings [75].

$$T(t)=\begin{cases}\frac{t+5.95x10^{10}}{t^2+6.25x10^{7}}, 0<t<11715\\ 298,\ t\geq 11715\end{cases}$$ "t" is time in seconds (3.3)

3.5.4 Porosity Effects

The heat transfer in solids module does not account for porosity in the materials. Also, porosity is not an input function for the material properties. To evaluate the effects of porosity, the Young's modulus of the deposit was varied. Researchers have determined that the Young's modulus is a function of the porosity in the material. J.K. Mackenzie derived the following expression which is widely accepted to calculate the Young's modulus for porous materials [78].

$$E=E_o(1-1.9P+0.9P^2) \quad (3.4)$$

The equation was applied to determine the effective Young's modulus for the Ni-based alloy and YSZ deposits with 10, 20, 30, and 40% porosity. These values were then material inputs for the deposits in the 0.25 tube geometric model. All other material properties were the same as seen in Tables 3.2 and 3.3.

3.5.5 CTE Effect of Deposit

The CTE mismatch is often attributed for the source of adhesion failure and thermal stresses. The CTE of the deposit was altered to determine its role in the thermal stress distribution and find an optimum material for the attachment of silica fibers to steel substrates. The study was completed by altering the CTE of the Ni-based alloy material model with the 0.25mm 304SS tubing. All of the other material properties were consistent with the reported values in Tables 3.2 and 3.3. The model was solved for the deposit with CTE values of 0.6, 7, 15, and 20 $\mu m/(m \cdot K)$.

3.5.6 Comparison of Different Material Tubes

The protective tubing may increase the thermal stresses of the system due to the increased composite mismatch in CTE. Therefore, nine materials with a wide range of CTEs were modeled for comparison. The materials and their respective CTE (at 700^{o}C) can be found in Table 3.4. All of the material properties can be found in Appendix F.

Table 3.4: CTE values for different modeled material protective tubing.

Material	**CTE, $\mu m/(m \cdot {}^{o}C)$**
304 SS	18.9
Quartz	0.55
Sialon	3.0
Aluminum Nitride	4.5
Alumina	8.1
Hastelloy B-2 (nickel superalloy)	11.8
Inconel 701	16.1
Copper	20.3
Invar 36	24.6

The material tubes were studied in both deposit material systems using the 0.25mm tubing geometric model.

3.5.7 Meshing for Modeling

All geometric models were meshed for modeling using tetragonal elements at the predefined size of "Extra Fine," whose dimensions are defined in Table 3.5. Two distributions were then added to allow for

finer elements along the interfaces of the different components. Table 3.6 reports the number of elements, the degrees of freedom and other meshing statistics for the different models.

Table 3.5: The predefined parameters of an "Extra Fine" element size in COMSOL®.

Maximum Element Size	2.67×10^{-3} m
Minimum Element Size	1.13×10^{-4} m
Maximum Growth Rate	1.35
Resolution of Curvature	0.3
Resolution of Narrow Regions	0.85

Table 3.6: The meshing statistics for all geometric and material models.

Deposit Material	Geometric Model	Distribution 1		Distribution 2		Total Number of Elements	Degrees of Freedom
		Number of Elements	Edges[1]	Number of Elements	Edges[1]		
Ni-based Alloy	No Tube	600	9, 14, 42, 46	175	11, 13, 15, 16, 53, 56	372,146	1,699,608
	0.25 Tube				11, 13, 15, 16, 53, 56, 60, 61	420,286	2,448,584
	0.5 Tube					419,668	2,445,080
	1.0 Tube				11, 13, 15, 16, 53, 56	423,144	2,467,084
YSZ	No Tube	600	9, 14, 42, 46	250	11, 13, 15, 16, 53, 56	427,110	1,949,116
	0.25 Tube				11, 13, 15, 16, 53, 56, 60, 61	514,522	2,991,036
	0.5 Tube					513,593	2,985,076
	1.0 Tube				11, 13, 15, 16, 53, 56	423,144	2,467,084

[1] The edges are labeled in Figure 3.7.

Figure 3.7 shows the distribution of the elements across the part and how the elements were concentrated around components' interfaces for the 0.25 tube geometric model. Tetragonal elements with equivalent length edges are considered high quality and represented by dark red in Figure 3.7. The regions around the fiber and interface are dark due to a high concentration of small tetragonal elements, as indicated by the color bar in the figure.

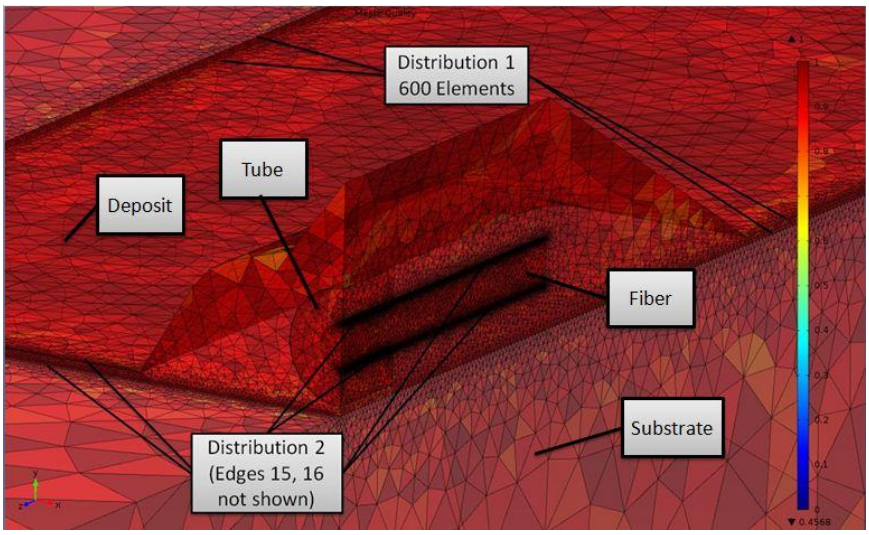

Figure 3.7: The tetragonal element shaped mesh for the 0.25 tube geometric model, seen in Figure 3.6 (c), created in COMSOL® with the edges that are used in the distributions described in Table 3.6.

4. Results

4.1 Sensor Signals

4.1.1 Comparison of Sensors Before and After Attachment

One sensor encapsulated by the Ni-based alloy deposit did not report a signal prior to the encapsulation and will not be discussed. After processing, one of the six intact sensors encapsulated by the Ni-based alloy reported no signal. Five of the seven YSZ encapsulated samples reported irregular or no signal after attachment. Signals were compared by their amplitudes and OPDs.

Figure 4.1 shows examples of collected spectra of undamaged sensors. The spectra from before and after the attachment process have the same frequency but the amplitude has changed.

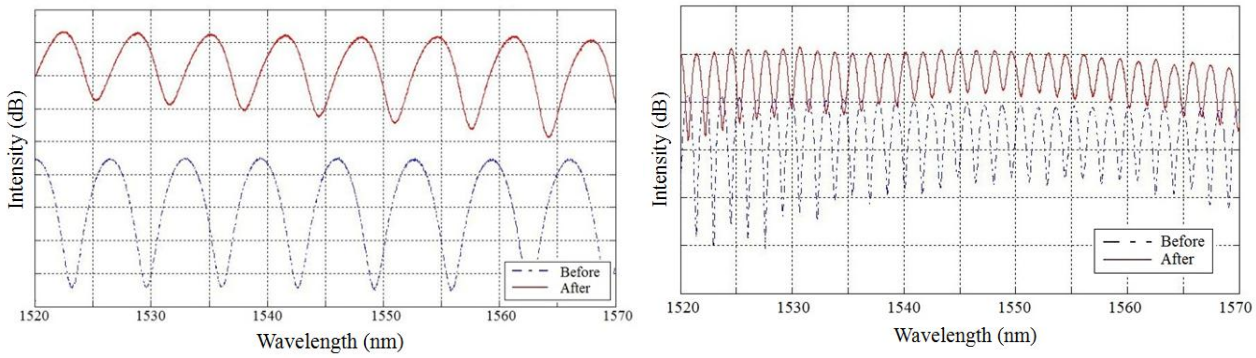

Figure 4.1: The optical spectra from before and after encapsulating sensors with (a) a Ni-based alloy deposit and (b) a YSZ deposit.

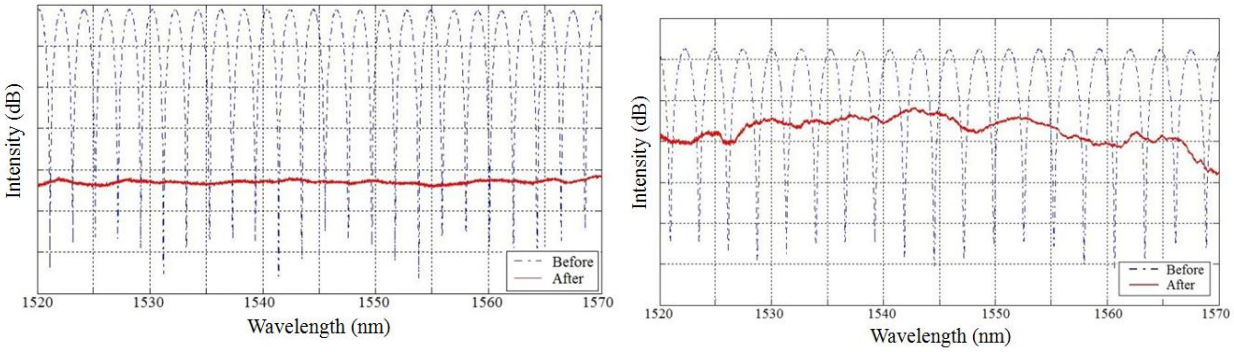

Figure 4.2: Examples of the optical spectra collected from sensors damaged during the encapsulation process for (a) a Ni-based alloy deposit and (b) a YSZ deposit.

Examples of the optical spectra from sensors damaged during processing can be found in Figure 4.2. Interference was not observed in these samples. All of the sensors tested can be found in Appendix B. The OPD did not significantly change for any of the sensors after encapsulation.

4.1.2 Sensor Signal at Elevated Temperatures

The Ni-based alloy deposit sample tested at elevated temperatures showed signal distortion between 200°C and 300°C. The sample continued to have additional interference at elevated temperatures and never recovered its original spectrum frequency. Figure 4.3 reports the collected spectra at various temperatures as the sensor was heated to 700°C.

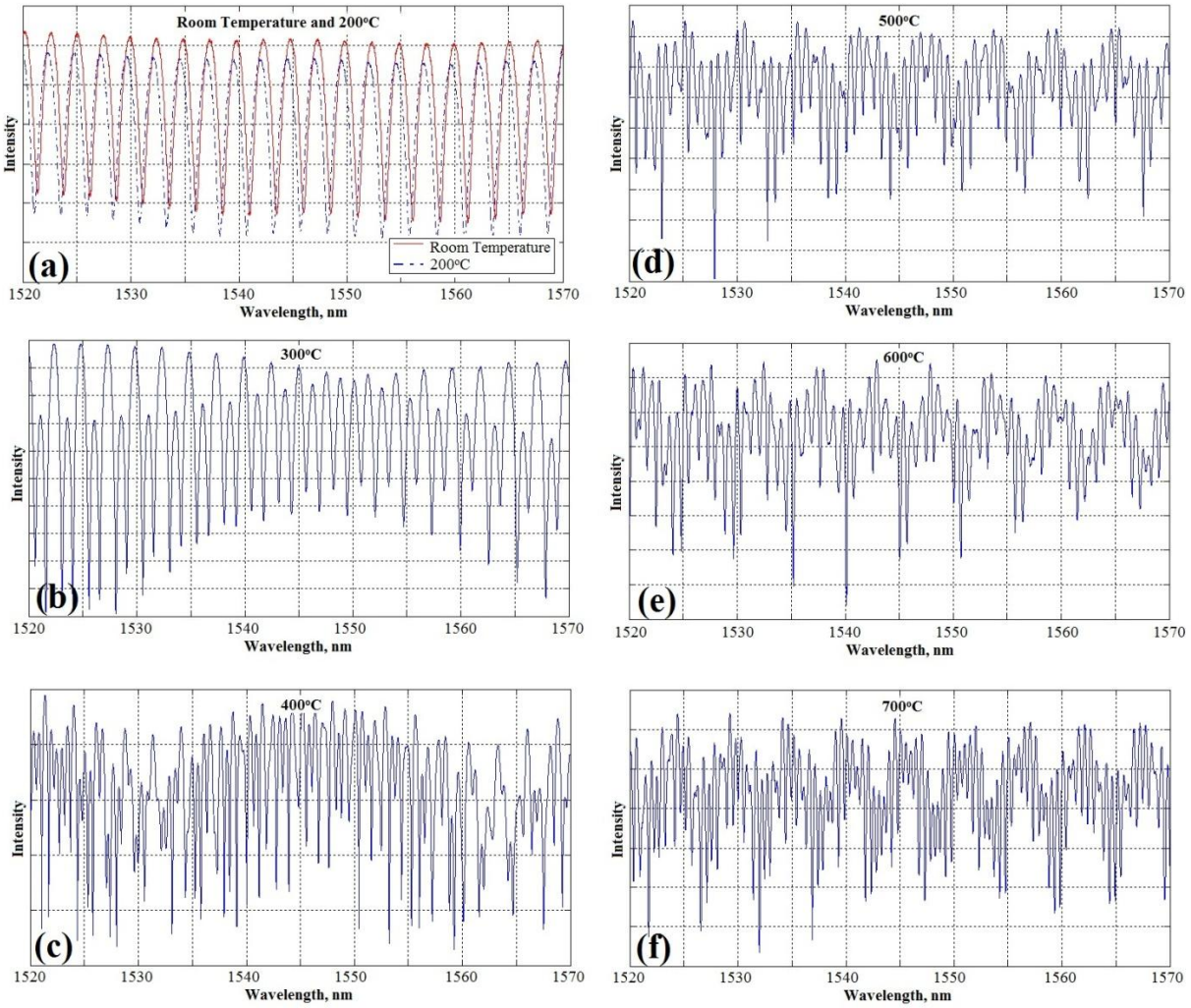

Figure 4.3: Spectra of Ni-based alloy encapsulated fiber at elevated temperatures: (a) at room temperature and 200°C, (b) at 300°C, (c) at 400°C, (d) at 500°C, (e) at 600°C, and (f) at 700°C.

Figure 4.4 shows two spectra collected 10 seconds apart while heating a Ni-based alloy encapsulated fiber to 400°C.

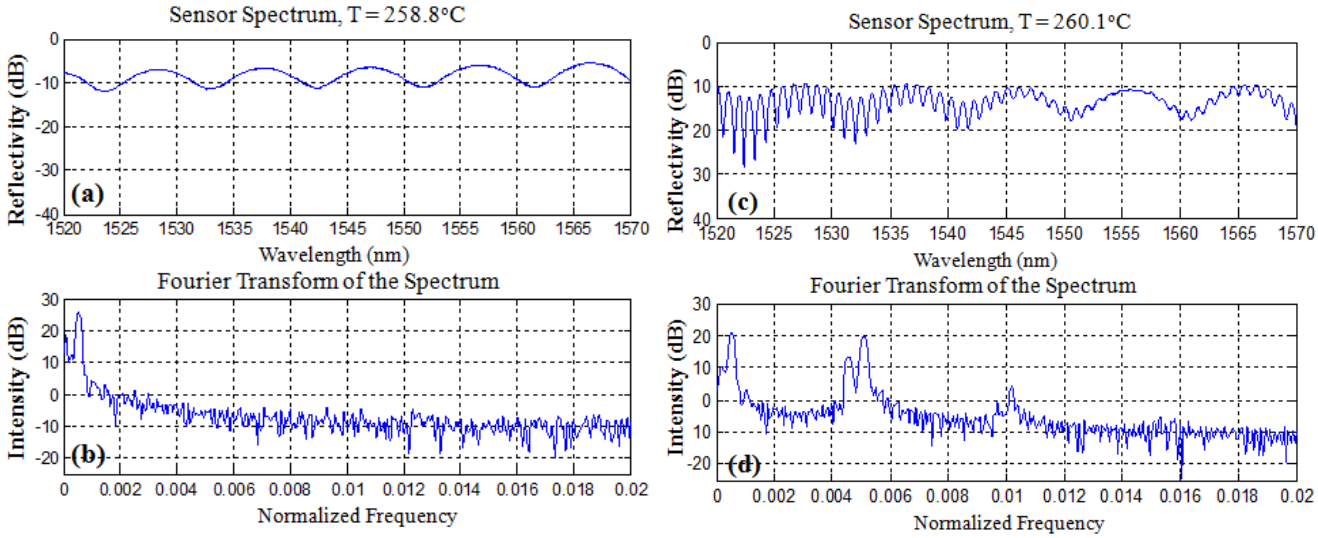

Figure 4.4: The spectra collected at (a) 258.8°C and (c) 260.1°C and their Fourier transforms are shown in (b) and (d), respectively.

A drastic change in the spectra behavior is observed around 260°C by comparing two sequential spectra. The Fourier Transform in Figure 4.4 (b) shows two additional peaks at different normalized frequencies. The additional peaks suggest an additional reflective surface that is causing constructive interference. Harmonic peaks are also observed at higher normalized frequencies from the distortion of the signal.

The spectra collected from the YSZ encapsulated fiber at elevated temperatures can be seen in Figure 4.5. Multiple spectra were collected at different times during the furnace's 10 minute dwell period at the specified temperature. These spectra are labeled as different data in Figure 4.5.

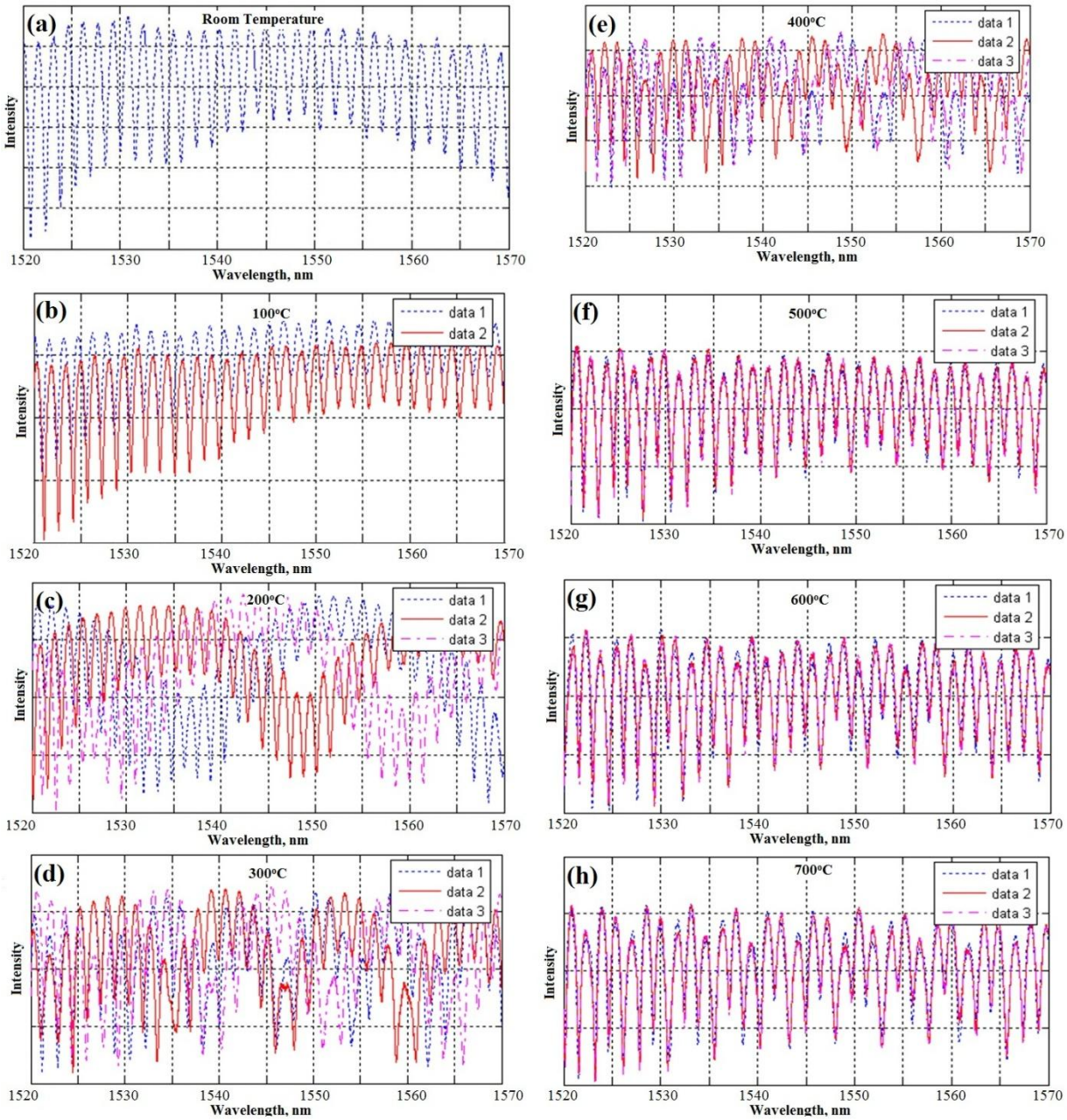

Figure 4.5: A YSZ encapsulated sensor's spectra at various temperatures: at (a) room temperature, (b) 100°C, (c) 200°C, (d) 300°C, (e) 400°C, (f) 500°C, (g) 600°C,and (h) 700°C. The different data in the figures represent spectra collected sequentially at the same temperature.

The spectra reported for the YSZ encapsulated sensor show a large behavior change between 100°C and 200°C. A larger superimposed frequency pattern appears at 200°C, 300°C and 400°C. The large frequency pattern experiences a peak shift over the 10 minute dwell period at each temperature. At temperatures

above 500°C, no clear consistent amplitude is observed and the large frequency pattern is no longer visible.

4.2 SEM Imaging

The structure shape and geometry was first captured at low magnification with a low acceleration voltage of 5kV. Figure 4.6 (a) is a labeled image of a Ni-based alloy encapsulated sample with the fiber intact. Figure 4.6 (b) shows a YSZ deposit that has a large cavity where the fiber was before it was pulled out during sample preparation.

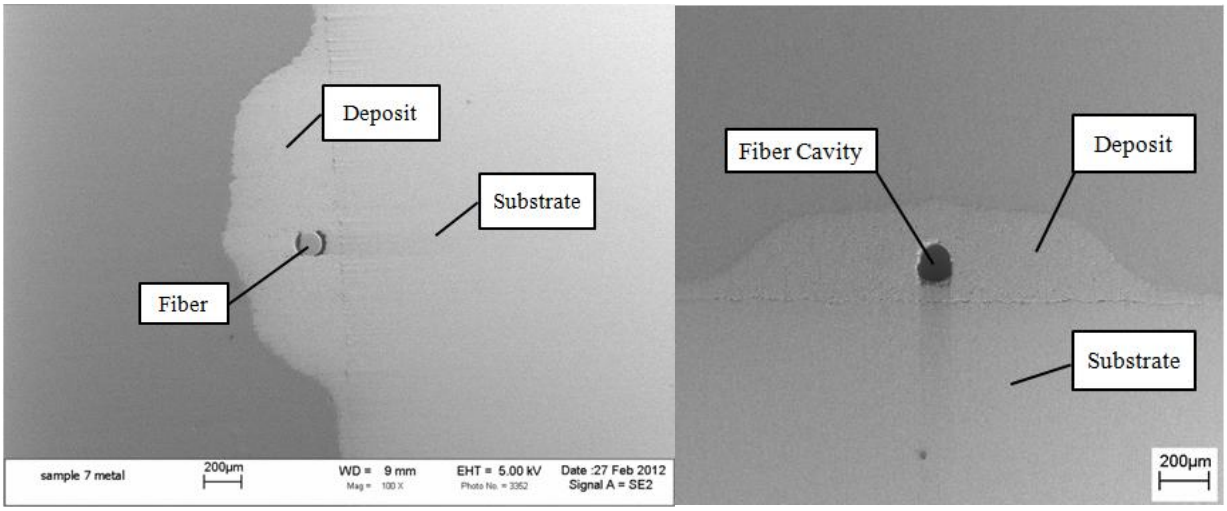

Figure 4.6: Cross section images of a (a) Ni-based alloy deposit and a (b) YSZ deposit.

The cross sections in Figure 4.6 had been cut and polished far enough into the sample that the protective steel tubing was not visible. Figure 4.7 shows the cross section of a system with the steel tubing around the fiber.

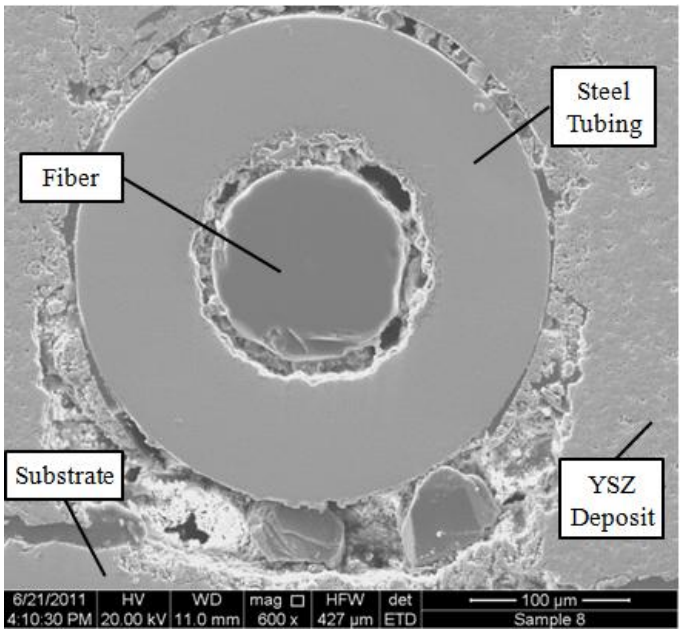

Figure 4.7: SEM image of YSZ encapsulated fiber with 304SS tubing

Large voids were found around the exterior of the tubing and between the tubing and the fiber. The outer diameter of the tubing was measured as 306.9µm and has a thickness of 75.5µm. The damaged fiber diameter was measured as 122.8µm. The shape and measurements were used for creating the model geometry.

The deposit-fiber interface was also investigated using SEM at regions of the fiber not enclosed with the tubing. Images collected at higher magnification around the fiber can be seen in Figure 4.8 for both material systems.

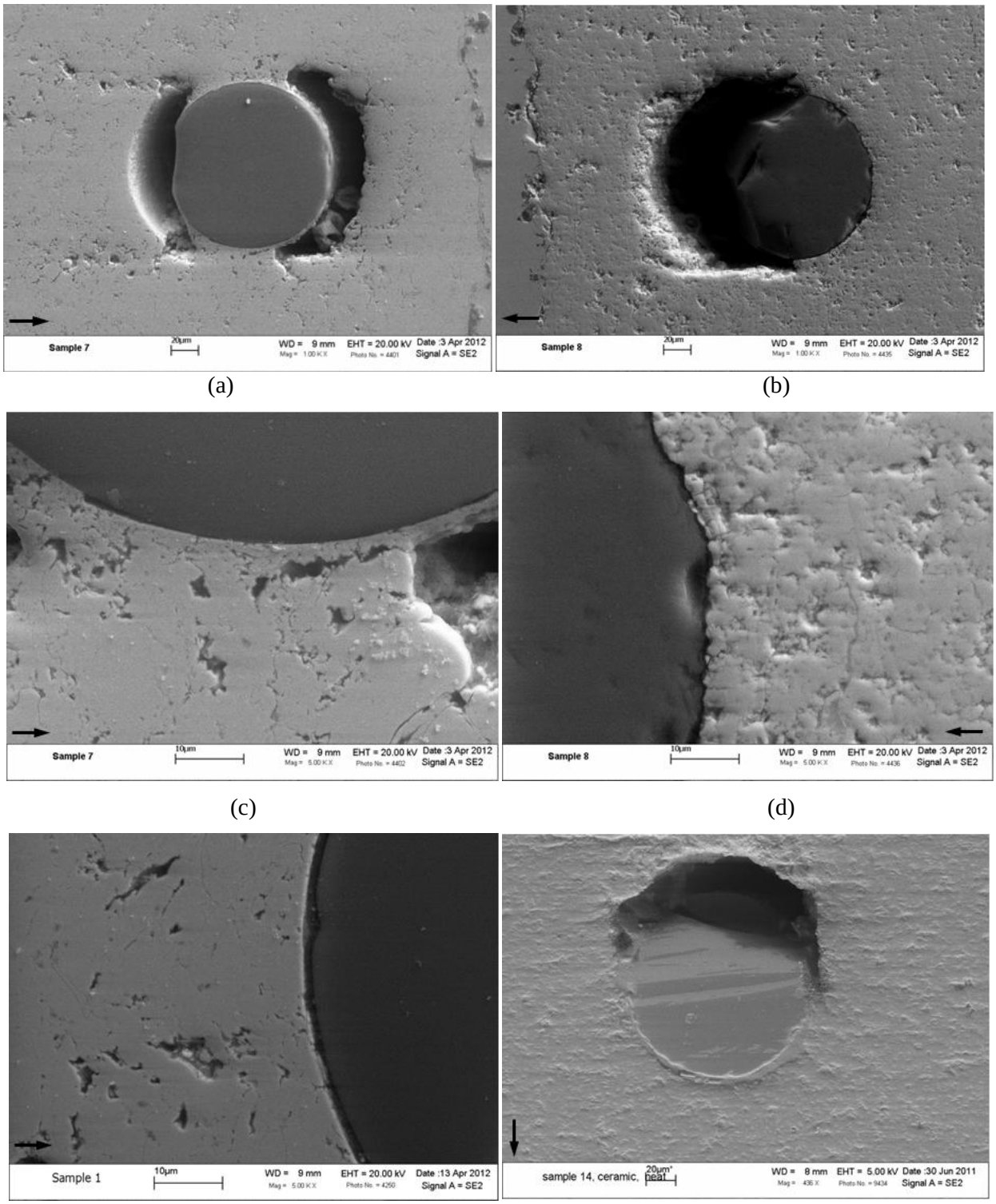

Figure 4.8: SEM cross section images of Ni-based alloy (a, c, e) and YSZ (b, d, f) deposits around the fiber at low (a, b) and high (c, d) magnifications. Images (e) and (f) are samples which have been heat treated to 700^{o}C. The (f) image was collected using a lower accelerating voltage than the other images. The arrows seen in the figures show the direction of the plasma spray.

All of the samples show a large void below the fiber (according to the plasma spray direction) and a few samples show voids above the fiber, as seen in Figure 4.8 (a). The YSZ encapsulated fiber edge, seen in Figure 4.8 (d), is much rougher than the edges of the Ni-based alloy encapsulated fibers. The heat treated systems, Figure 4.8 (e) shows a visible separation between the fiber and the deposit. Figure 4.8 (f) shows a white substance on the fiber end face and within the pores and voids of the sample. The substance is assumed to be contamination from sample preparation where polishing material and debris have filled the voids. The contaminants have filled in the gap between the fiber and the deposit that was formed during the heat treatment.

The substrate-deposit interface was also investigated to ensure good adhesion after processing and images of both material systems can be seen in Figure 4.9.

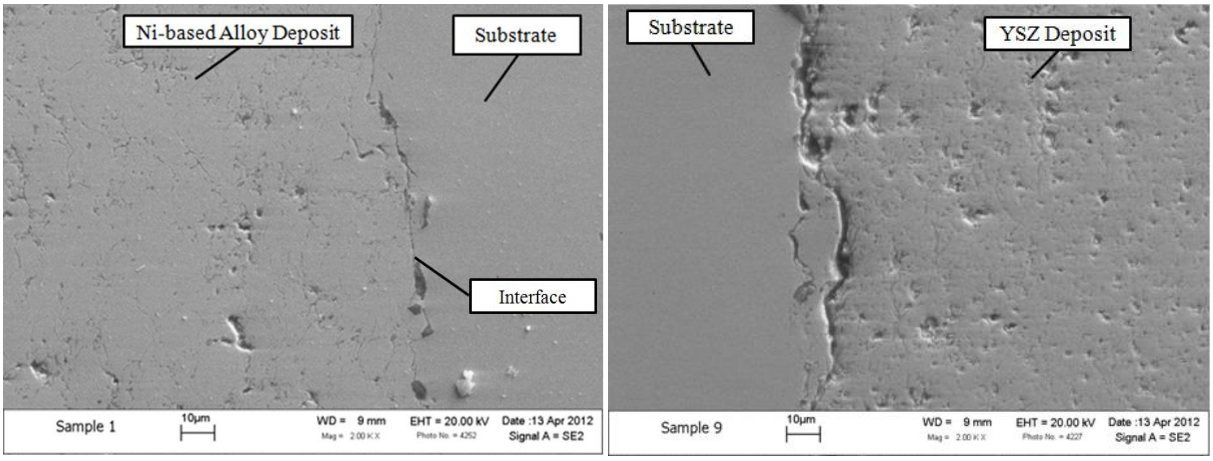

Figure 4.9: The substrate-deposit interface for a (a) Ni-based alloy deposit and a (b) YSZ deposit.

The YSZ system interface is clearly visible due to cracking and pores that have congregated along the edge. The substrate-deposit edge for the Ni-based alloy deposit system has pores but does not show much separation.

4.3 EDS Chemical Analysis

Multipoint analysis was completed at the substrate-deposit interface to evaluate the chemical species present on different features. The elements were selected from knowledge of the material system and the EDS produced spectra. The elements were reported using a normalized mass percent. Figures 4.10 and 4.11 are labeled images that show the locations of the acquired spectra reported in Tables 4.1 and 4.2, respectively.

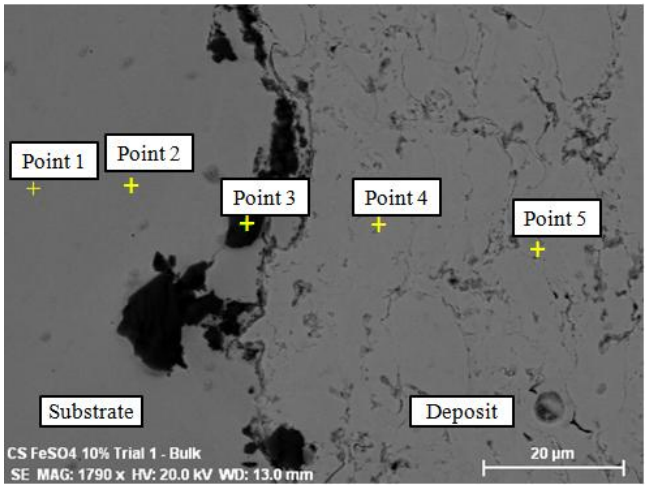

Figure 4.10: Point locations for EDS acquired spectra of the Ni-based alloy system on a backscattered electron image.

Table 4.1: The elements measured at points across the Ni-based alloy deposit-substrate edge.

Point	Element in Mass Percent (%)					
	Aluminum	Silicon	Chromium	Manganese	Iron	Nickel
1	0.05	0.26	19.32	-	72.30	8.08
2	0.05	0.26	19.35	-	72.30	8.04
3	93.72	1.33	1.03	-	2.06	1.86
4	1.75	0.59	0.29	1.79	0.80	94.77
5	1.67	0.67	0.23	1.97	0.49	94.96

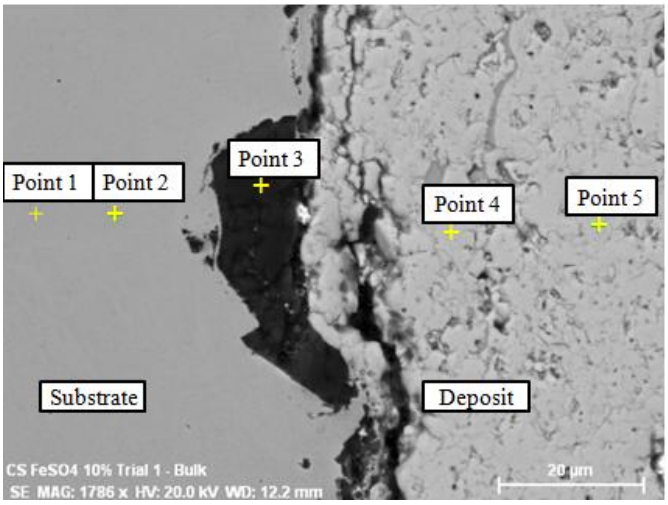

Figure 4.11: Point locations for EDS acquired spectra of a YSZ system on a backscattered electron image.

Table 4.2: Mass percent of each chosen element measured from EDS at different points across a YSZ system's substrate-deposit interface.

Point	Element in Mass Percent (%)						
	Aluminum	Titanium	Chromium	Iron	Nickel	Yttrium	Zirconium
1	0.25	-	19.18	72.35	8.22	-	-
2	0.29	-	19.11	72.44	8.17	-	-
3	93.45	2.39	1.03	2.33	0.80	-	-
4	0.77	-	-	-	-	11.94	87.30
5	0.65	-	-	-	-	11.82	83.54

4.4 Porosity Measurements

Representative micrographs of both material systems can be found in Figure 4.12 at a high and low magnification, indicating the degree of imbedded and interconnected porosity throughout the two deposit materials. The Ni-based alloy deposits averaged a porosity of 8.84%±1.37% and the YSZ deposits averaged a 15.89%±1.37%. The porosity measurements were completed with the high magnification images due to the size of the pores in the samples.

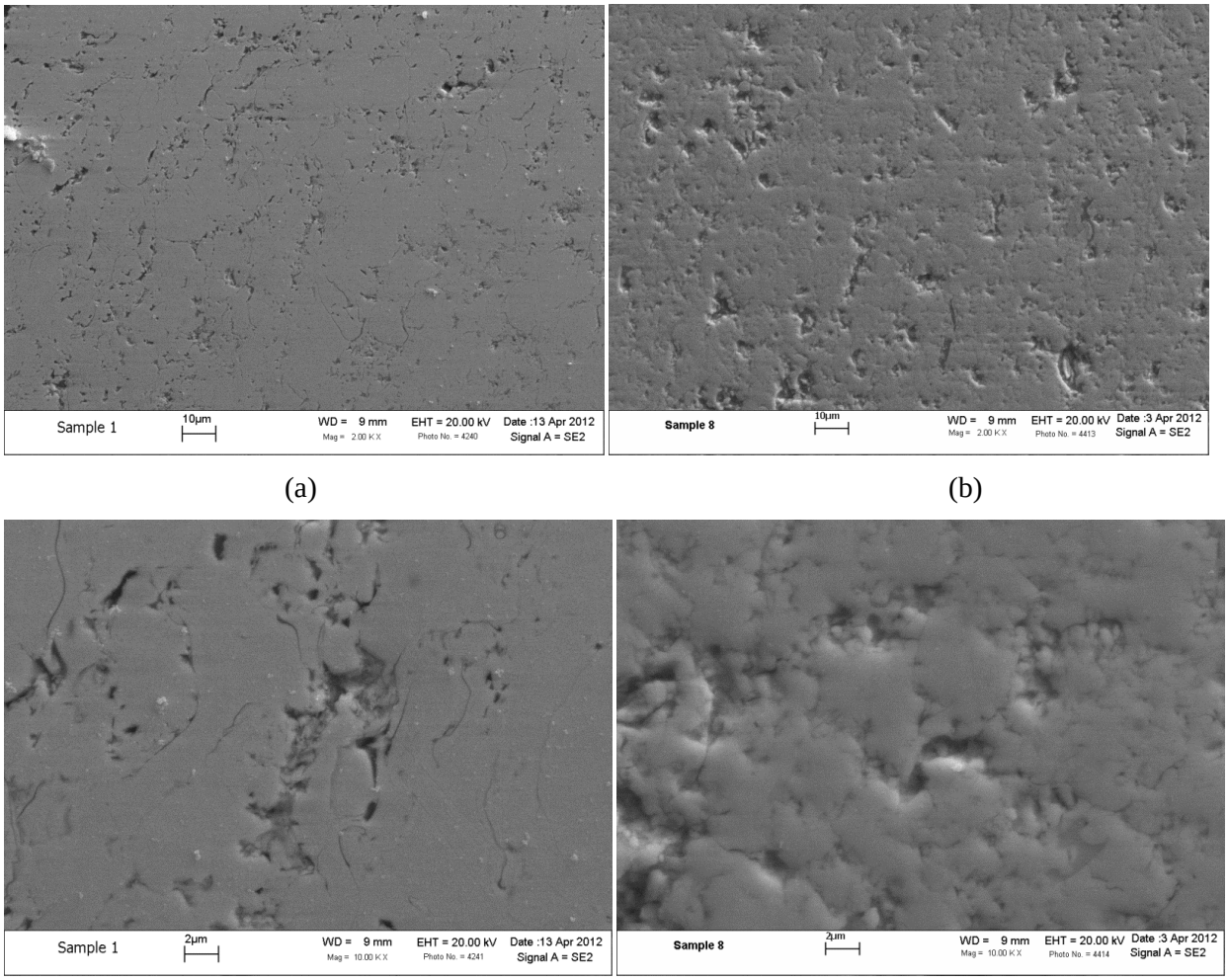

Figure 4.12: Representative SEM images of the (a, c) Ni-based alloy deposits' and (b,d) YSZ deposits' microstructures. The SEM images are collected at (a,b) low and (c,d) high magnifications.

4.5 Nanoindentation of Samples

Two example load-displacement curves for the Ni-based alloy and YSZ deposits are shown in Figure 4.13. The average hardness and Young's modulus values can be found in Table 4.3. The established values for the bulk materials are also listed for comparison. The F-test ($\alpha = 0.1$) reported that there was no change in the mechanical properties across the thickness of the deposit.

Table 4.3: Average hardness and Young's Modulus measured and published bulk values for the Ni-based alloy, YSZ, and the 303 SS substrate including 95% confidence intervals.

Material	Hardness, GPa		Young's Modulus, GPa		Maximum Depth (nm)
	Measured	Published	Measured	Published	
Ni-based alloy[1]	3.60±0.58	0.130-0.300	177±14	41	690±60
YSZ[2]	12.5±3.44 (14.4±2.93)*	13.5	160±30 (180±23)*	222	470±80 (410±30)*
303 SS[1]	2.94±0.23	1.63	178±10	190	1240±40

*Data with two outliers removed
[1]Published data from [76].
[2] Published data from [75, 79].

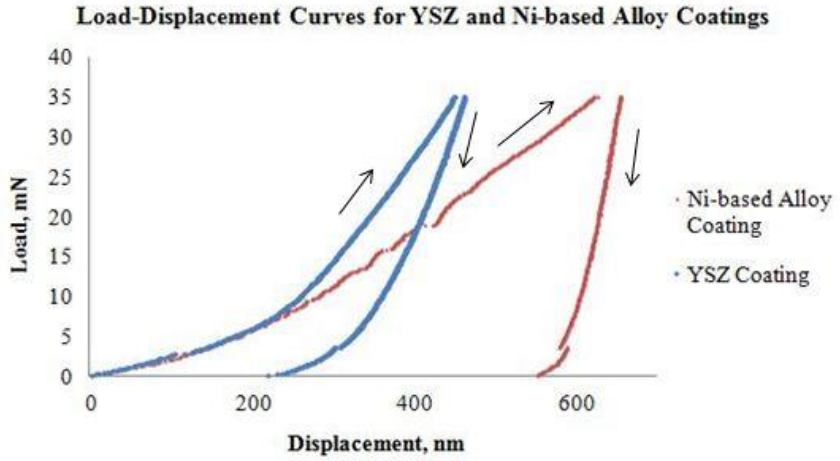

Figure 4.13: Load-Displacement curves for loading and unloading of both material systems.

Figure 4.13 shows an example of a Ni-based alloy deposit indentation process with a rough loading curve and a YSZ deposit loading curve with a discontinuity. Both systems reported several curves with discontinuities and irregular changes in slopes.

4.6 Raman Spectra of YSZ Deposit

The Raman spectra were fitted using the Lorentzian function with five peaks selected in the 200-500cm^{-1} range as seen in Figure 4.14. The peaks observed have been previously reported for the monoclinic and tetragonal phases [49, 67, 80]. All fitted peak positions were recorded for each spectrum. The data retrieved for both cross-sectioned samples showed no consistent peak shift across the thickness or width of the individual deposits. However, a noticeable peak shift was observed between as-processed samples and samples that were heat-treated as seen in Figure 4.15. Figure 4.15 reports the peak location of the starred peak in Figure 4.14 for the different samples. This peak was selected because it was well defined

and showed minimum overlap with other peaks, which allowed a more accurate fit. The error bars show the 95% confidence interval for the data collected.

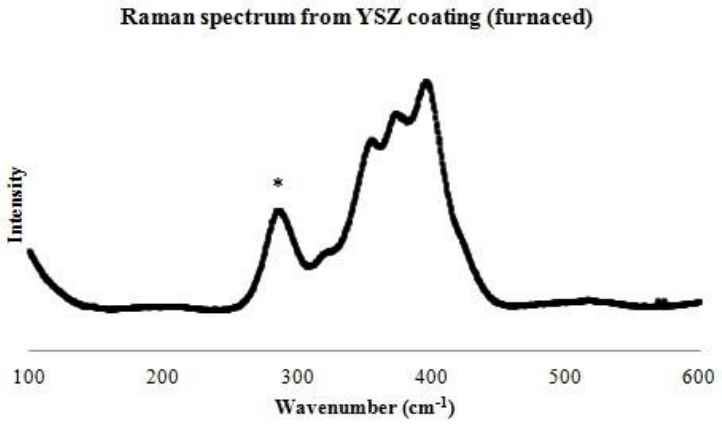

Figure 4.14: Typical Raman spectrum produced for a YSZ deposit.

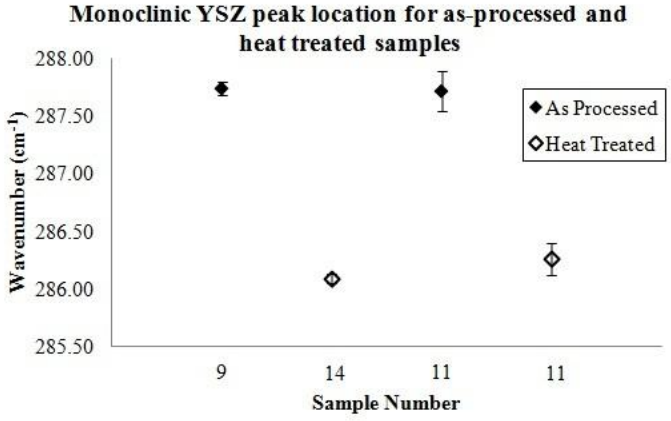

Figure 4.15: Comparison of peak locations for as-processed and heat treated YSZ samples.

The peak shift was consistent for the cross-sectioned and surface tested samples. The direction of the peak shift may be indicative of an applied force in the tensile direction. The larger variance in sample 11 is due to the surface being rougher than the polished cross-sections.

4.7 Thermal cycling to failure

The Ni-based alloy deposit did not show any signs of spallation during or after thermal cycling, as seen in Figure 4.16. The deposit did show a difference in color during cooling between the encapsulated fiber region and the thinner region away from the sensor head, which could indicate that the later is cooling

faster. However, it is unclear if this is because the thicker part of the deposit was delaminated or if it was cooling slower due to the different amount of material.

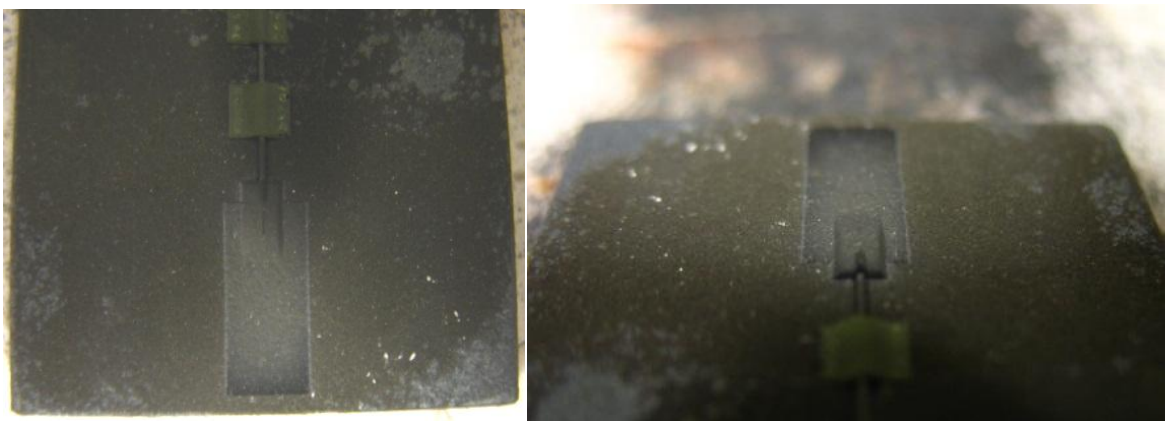

Figure 4.16: The Ni-based alloy sample after thermally cycling 20 times.

The YSZ deposit failed after 6 cyclic loads. The images of the broken specimen can be found in Figure 4.17. Failure occurred during cooling below 200^{o}C. The images show that the delamination, spallation and cracking are located at the raised region around the fiber. The deposit did not show any signs of failure prior to fracture.

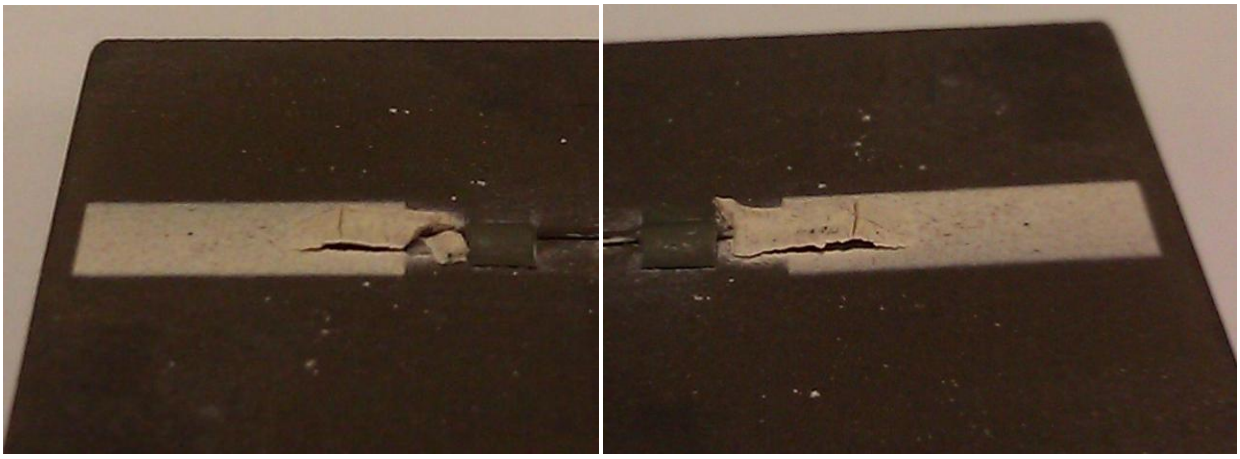

Figure 4.17: Images of delaminated YSZ deposits from thermal cycling.

4.8 Scratch Testing

The failure mode was difficult to identify visually by the scratch on the Ni-based alloy due to the ductile nature of the deposit and the substrate. Figure 4.18 shows an image, from above, of a scratch on the Ni-

based alloy deposit. The signals measured by the instrument during scratching are seen below the image and are aligned with the scratch for easier location of the failure point.

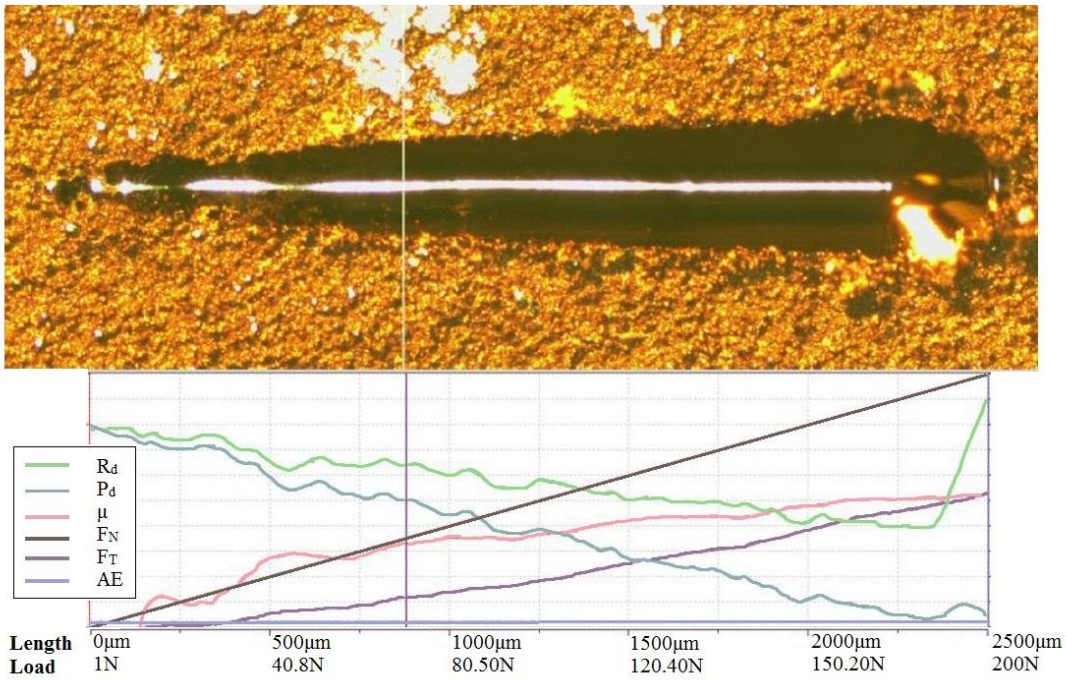

Figure 4.18: Scratch and sensor signals for Ni-based alloy deposit.

The acoustic emissions and depth curves did not show delamination behavior. The irregular shape of the coefficient of friction curve, labeled "μ" in Figure 4.18, as the load is first being applied is indicative of sticking and slipping across the material. The indenter tip then begins to experience a linear response with the applied load. The change in material response suggests that delamination has occurred. The failure position was chosen at the inflection point of the μ curve.

Adhesion and cohesion failure were observed in the YSZ deposited sample. Figure 4.19 is an image of a scratch with the labeled locations of failure.

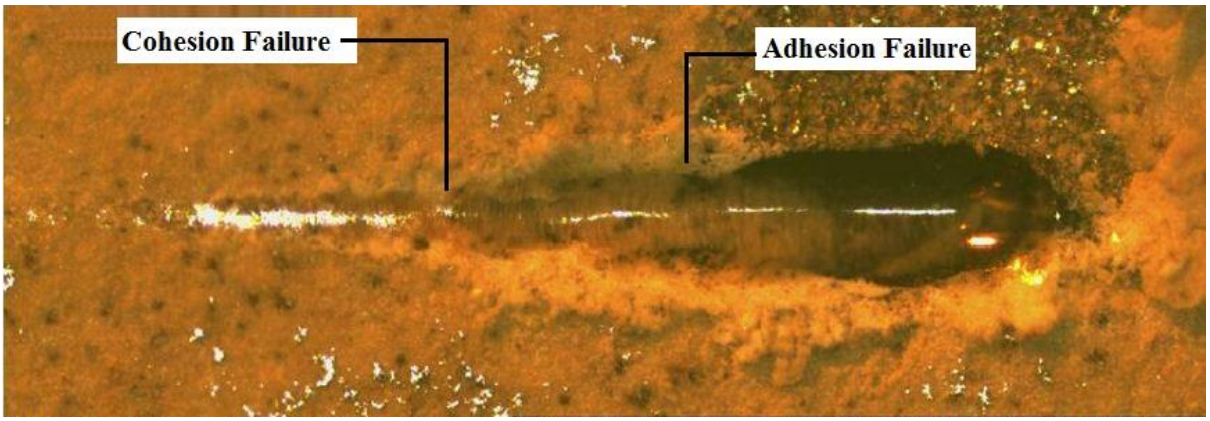

Figure 4.19: Image of scratch on YSZ deposited sample with the positions where failure occurred.

The brittle nature of the YSZ deposit allowed the user to identify the fracture locations visually. Cohesive failure was first observed in the deposit around the scratch edges where the YSZ deposit began fracturing internally. Adhesive failure was identified by complete delamination and removal of the deposit from the substrate. Table 4.4 reports the critical force and stress for delamination for both material systems. The stress for delamination was calculated as described in Section 3.4.4.

Table 4.4: The measured critical forces and calculated stress for adhesion failure of the deposits.

Deposit Material	Critical Force, N			Stress, GPa
	Scratch 1	Scratch 2	Average	Average
Ni-based Alloy	86.0	71.0	78.5	1.20
YSZ	124	70.4	97.2	3.61

4.9 Modeling

4.9.1 Ni-based alloy deposit system

The temperature probes in the model show that the deposits experience only a maximum difference of 2^{o}C at any point during the study. Therefore, in the following sections the deposits are considered to cool homogeneously.

Different Tube Lengths

The maximum stress for the Ni-based alloy deposit system was identified at the interface between the fiber and the protective steel tubing. This was the location for maximum stress for all geometric models that had a tube. Figure 4.20 shows the change in maximum stress at all interfaces while cooling.

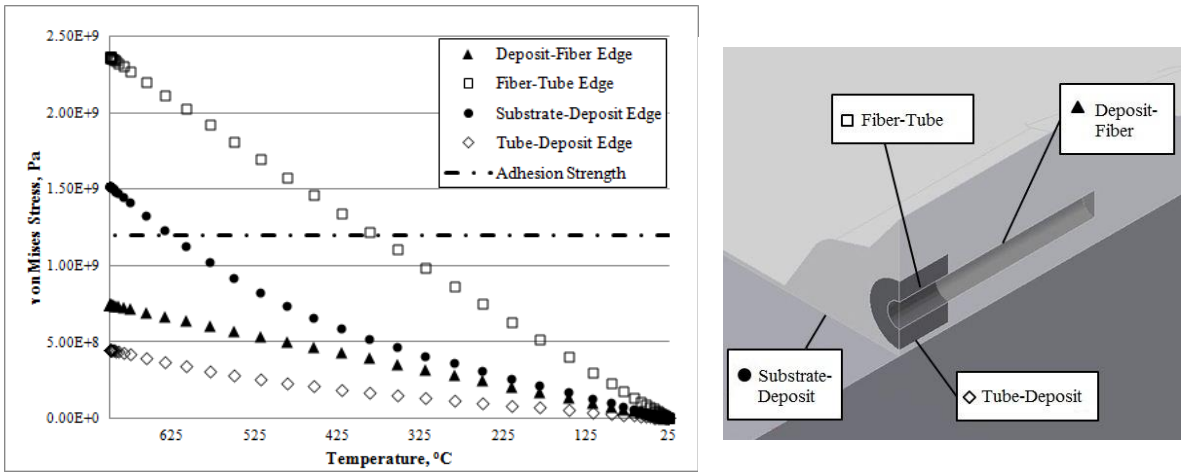

Figure 4.20: (a) The calculated maximum von Mises stress according to the temperature for different edges in a Ni-based alloy model with the 0.25mm 304 SS steel tubing. (b) The labeled model for the locations of the probes.

The stress at the substrate-deposit interface exceeds the adhesion strength at temperatures above 627°C.

The maximum stress for each geometric model at the edges of interest can be seen in Figure 4.21.

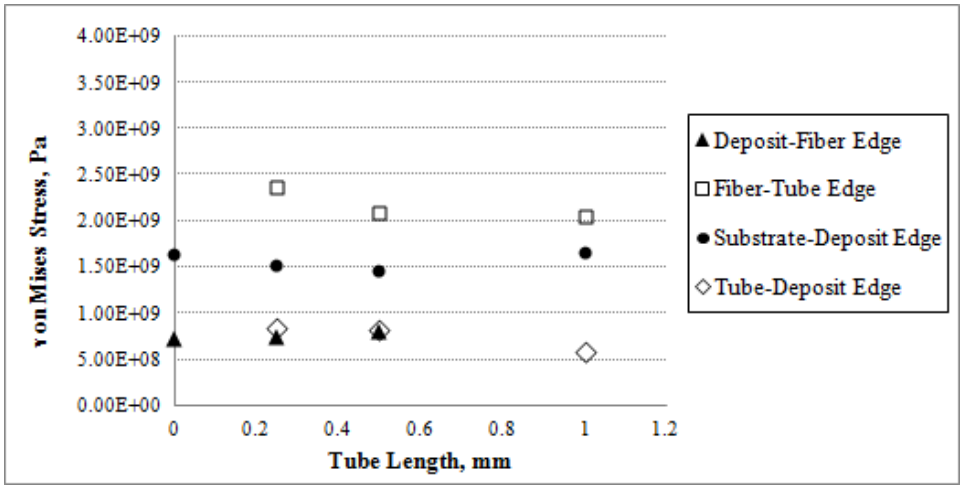

Figure 4.21: The von Mises stress distribution for different tube lengths in the Ni-based alloy system.

The maximum stresses at the fiber-tube edge and tube-deposit edge decrease by increasing the length of the tube. The stress at the substrate-deposit interface can be minimized by using a 0.5 mm tube. A small increase in maximum stress at the deposit-fiber edge with tube length is also reported.

Different material tubes

The tubing material significantly altered the stress distribution in the system. Figure 4.22 shows the maximum von Mises stresses reported by the edge probes for the different material tubes according to their CTE.

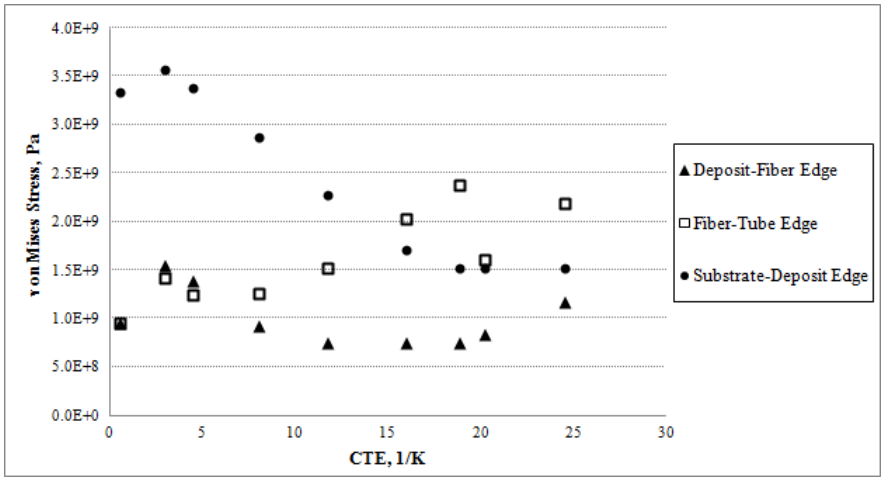

Figure 4.22: The maximum von Mises stress at the various edges in the Ni-based alloy deposit system for various protective tubes with unique CTE values.

A significant decrease in stress at the substrate-deposit interface is observed for tubes with higher CTE. However, the materials with higher CTE values experience an increase of stress at the fiber-tube edge. The stress at the deposit-fiber edge is lowest for the alumina and Hastelloy B-2 alloy, which have moderate CTE values. There was no discernible correlation between the stress experienced at the tube-deposit interface and the CTE. The maximum stress values ranged from 0.82GPa and 1.7GPa for the tube-deposit edge.

4.9.2 YSZ system

The YSZ system has a much larger stress variance across the model than the Ni-based alloy. The scale of the graphs should be considered when comparing to the Ni-based alloy system.

Different length tube system

The YSZ deposit model exhibited a much higher von Mises stress at the substrate-deposit interface and a different stress distribution than the Ni-based alloy system. The edge probe results for the YSZ deposit system and the 0.25 tube geometric model can be seen in Figure 4.23.

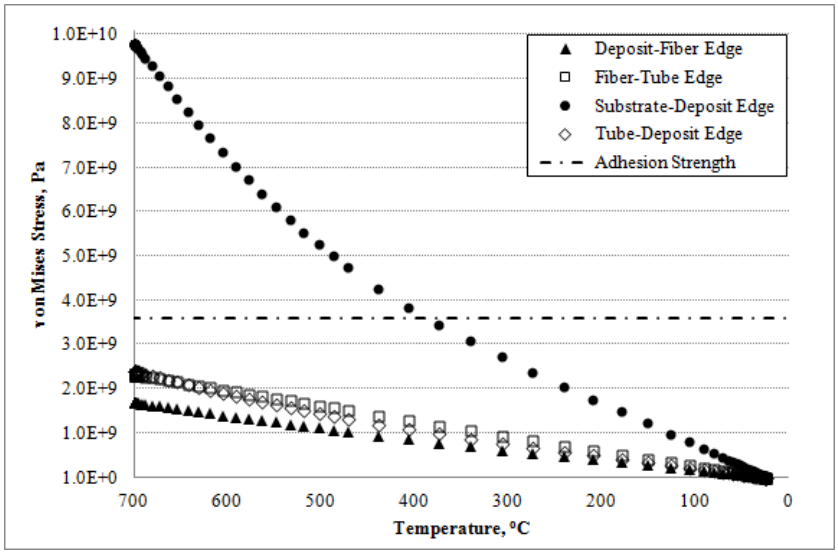

Figure 4.23: The maximum von Mises stress along various edges in the 0.25 tube geometric model for the YSZ deposit material.

The thermal stress at the interface exceeded the adhesion strength at temperatures above 391^{o}C. All of the edges reported a sharp decrease in thermal stress values at low temperatures. Thermal stress values drop four orders of magnitude when cooling from 40^{o}C to 25^{o}C, which the model calculates to take 12,000 seconds.

The different geometric models are compared by their maximum von Mises stress at the different edges for the YSZ deposit system in Figure 4.24. The maximum von Mises stress for each probe is not significantly affected by the tube length.

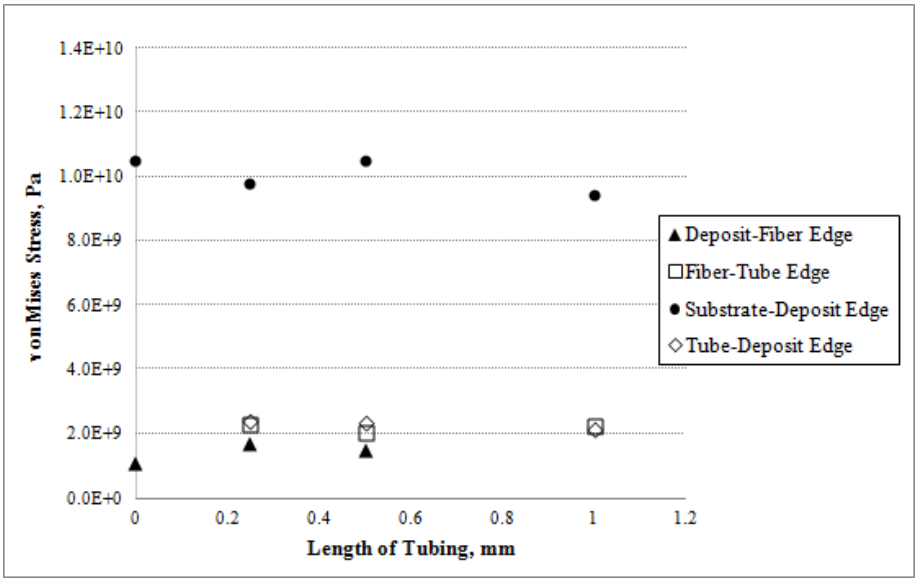

Figure 4.24: The edge probe results for the maximum von Mises stress of the YSZ model for the different geometric models.

Different Protective Tubing Materials for the YSZ Deposit

The protective tubing altered the values of the stresses along the fiber and at the substrate-deposit interface, as seen in Figure 4.25.

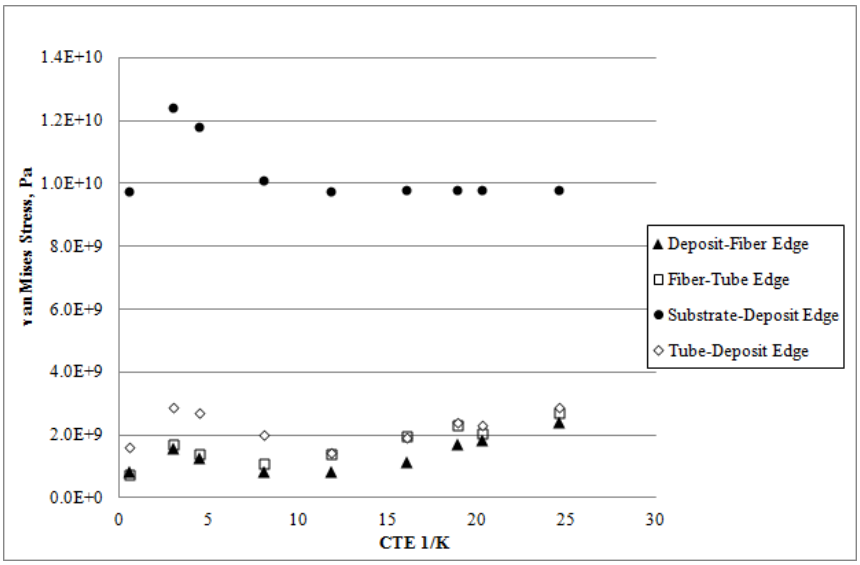

Figure 4.25: Maximum von Mises stress along different edges for the YSZ deposit model with different protective tubing materials. The 0.25 tubing geometrical model was used.

The thermal stresses along the substrate-deposit interface were reduced when using a tube with a higher CTE. The fused silica tube, the same material as the fiber, had a low CTE value but also reduced the

stress at the interface. Thermal stresses along the fiber edges and at the tube-deposit interface were affected similarly by the change in the material tubing. The lowest maximum stresses along the fiber edges were seen for the fused silica, alumina and Hastelloy B-2 alloy tubes.

4.9.3 Porous Deposits

The increase in porosity decreased the stresses along the substrate-deposit interface for both material systems, as seen in Figure 4.26 (a). The same trend was seen along the deposit-fiber and tube-deposit edges. However, stress along the fiber-tube edge increases with porosity for both material systems, as seen in Figure 4.26 (b).

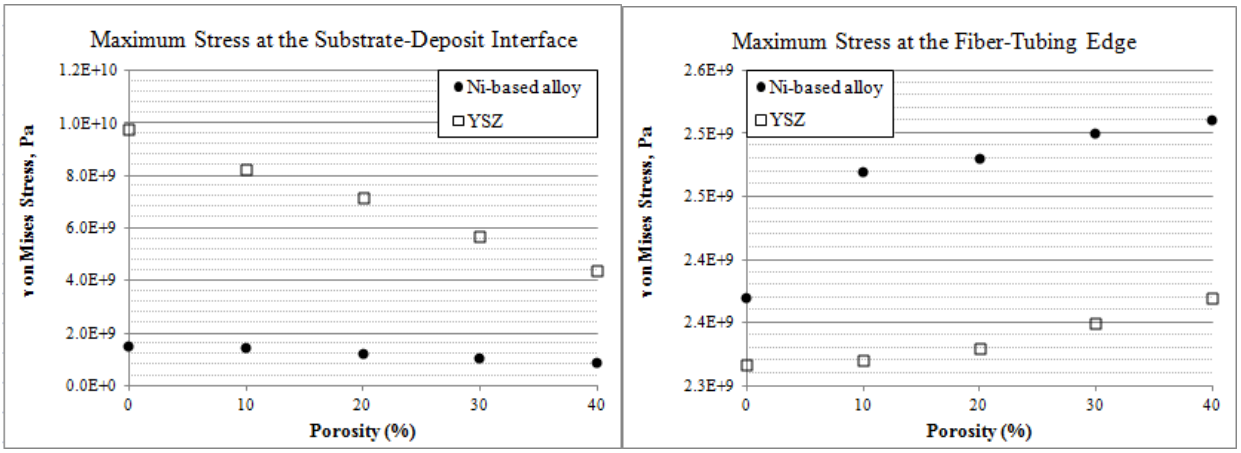

(a) (b)

Figure 4.26: The maximum von Mises stress along the (a) substrate-deposit interface and the (b) fiber-tubing interface for both material deposits at various porosities.

4.9.4 Varying CTE of the Deposit

The stress distribution of the Ni-based alloy system varied for different values of CTE. The maximum von Mises stress for the various edge probes can be seen in Figure 4.27. The CTE value at 12 μm/(m·K) is the true CTE value of the material.

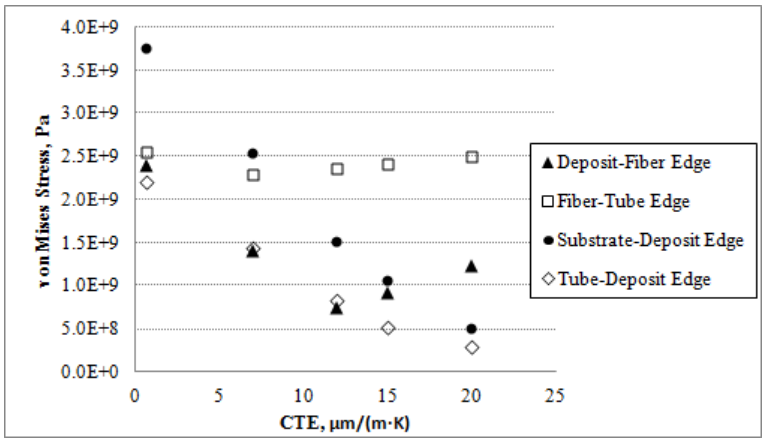

Figure 4.27: The stress distribution changes from altering the CTE of the Ni-based alloy deposit.

5. Discussion

5.1 Sensor Signal

5.1.1 Processing Induced Failure

Six of the sensors were broken during plasma spraying, as seen in the spectra collected after processing in Figures 4.2 and in Appendix B. The sensors may be broken between the first reflective surface and the second reflective surface because a signal is detected without interference. Light is not reflected from the end face of the fiber to allow for a usable signal for strain measurement. The current processing conditions for the YSZ deposit appear too aggressive to attach the silica fibers.

The fibers encapsulated by YSZ appear dented and damaged by the thermal spraying, as seen in Figure 4.8. But the Ni-based alloy fibers appear to have smooth, circular edges. The signal would not be distorted from damage to the fiber's exterior, as seen in these images. But, the fiber core could have been affected at locations of impurities and imperfections at other regions of the fiber, which would alter the signal. The aggressive nature of the YSZ deposit may explain why more sensors failed after encapsulation by YSZ than the Ni-based alloy. The increased success rate of Ni-based alloy encapsulated sensors may be due to the material properties or the plasma spray conditions. The spray parameters may need to be altered for both deposits to protect the fibers.

The tubes helped restrain the fibers during spraying. But it is unclear if they protected the fiber from the applied processing stresses because no sensors were attached without tubing for comparison. Figure 4.7 shows cracking and fracture around the exterior of the fiber and the tube's interior. However, the tube's exterior appears undamaged. The fiber's fracture and tube's interior deterioration do not appear to be from plasma spraying. The location and implementation of the tubing may need to be optimized to protect the integrity of the sensor head. Previous reports show that the processing can induce failure of the fibers

due to silica's low compressive strength and brittle nature. A stiff tube may be required along the entire encapsulated region of the fiber.

Before encapsulation, the air gap and end face of the fiber act as the reflective boundaries in the IFPI sensor. After encapsulation, the signal intensity is altered due to the reflective properties of the deposit material that encloses the end of the fiber. But, the OPD should not change unless the fiber is stressed or bent. The OPDs calculated before and after processing for the unbroken sensors reported little to no change. A larger OPD after processing would have indicated a radial compressive stress had been imposed. The changes in the signal's amplitude indicate that the fibers are well encapsulated, and the lack of an OPD change suggests that the fibers are unstrained.

5.1.2 Signal Degradation at Elevated Temperatures

At elevated temperatures, the signal may be distorted by an additional reflection surface. The Fourier transform in Figure 4.4 shows additional high intensity peaks that appear after a 2^{o}C change in temperature. The sudden change in signal is likely due to delamination of the deposit at the fiber's end face. Delamination would occur because the metal and ceramic deposits are expanding at greater rates than the silica fiber during heating. An additional cavity is then created by the air gap between the fiber's end face and the deposit surface. The signal would be a combination of three different interference patterns. Figure 5.1 is a schematic of the delaminated deposit-fiber interface and shows the three OPDs that are generated.

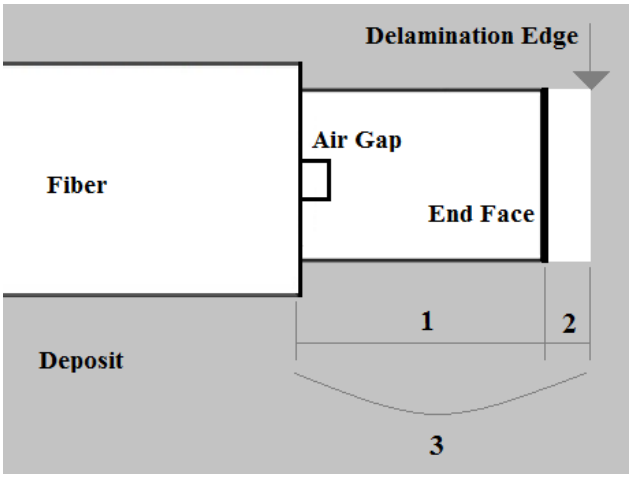

Figure 5.1: Schematic of an encapsulated fiber after delamination.

The original OPD can no longer be calculated from the signal to measure strain because of the additional interference. The end face of the fiber may need to be coated or tapered to avoid any additional reflective surfaces caused from delamination in order to control the signal behavior.

The signal change occurred in the YSZ system before 200^{o}C and in the Ni-based alloy system around 260^{o}C. Delamination should occur in the Ni-based alloy system first if only the CTE mismatch is considered. However, the YSZ deposit is less compliant to changes in the system and more likely to delaminate than the Ni-based alloy.

5.2 Mechanical Properties

5.2.1 Porosity

The deposits exhibited a similar pore fraction. The YSZ system reported higher porosity but this may be due to errors in the measurement.

The images for porosity measurements were collected using a high accelerating voltage. A high accelerating voltage produces enhanced edge effects and reduces the probe size to allow for better lateral resolution. However, the secondary electrons produced are from deeper in the sample and surface

topography information can be lost. It would be assumed that the images for porosity measurements should be collected with a low acceleration voltage. But, the lamellar microstructure was not as visible with a low acceleration voltage because the samples suffered from contamination. The pores and interlamellar voids were filled and leveled with contaminates. The high acceleration voltage enhanced the backscatter contrast to allow for the porosity to become more visible. Regions that show high concentration of aluminum and calcium have been observed throughout the YSZ and Ni-based structure, as reported in the EDS data in Tables 4.1 and 4.2. These regions are considered to be voids that have been filled during sample preparation.

The deposit's compliance is dependent on the porosity. Previous studies show that an increase in porosity can allow systems to operate with a larger mismatch in CTE and can lengthen the adhesion lifetime of the deposit [40, 81]. However, pores can provide pathways for corrosive species that cause premature failure [18].

Although the two materials both showed similar porosity, their microstructures appear very different. The Ni-based alloy deposits have more interlamellar voids and grain-like structures, as seen in Figure 5.2.

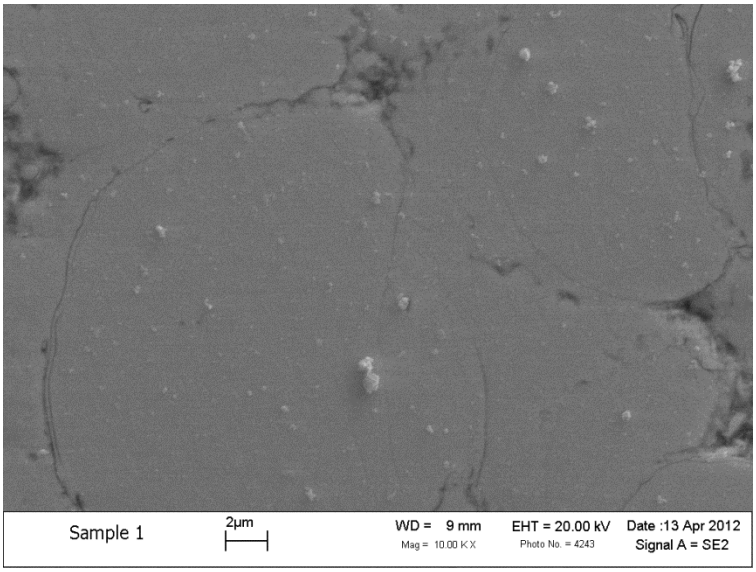

Figure 5.2: The grain-like structure in a Ni-based alloy deposit.

The grain-like structures are most likely particles that were only partially melted in the plasma spray process [17, 18]. The lamellar structure and the partially melted particles may indicate that the plasma spray processing parameters are not fully optimized for a fully cohesive deposit. Interlamellar cracks can cause delamination under compressive loading [43, 55, 82]. However, compressive forces required to induce cracking are restrained to the region around the substrate-deposit interface [45, 46, 48]. Figure 4.10 shows a crack along the deposit-substrate interface. However, Figure 4.9 (a) does not show any cracking. Long durations at elevated temperatures will allow creep to be more prevalent and reduce cracking [53]. It is predicted that the Ni-based alloy will have a longer life than the YSZ deposits due to their microstructures and dominant relaxation mechanisms.

The YSZ deposit does not show the same lamellar structure or any evidence of partially melted particles. Micro-cracks are visible throughout the deposit connecting pores in random directions, and separation is observed at the substrate-deposit interface. Micro-cracking is dominant in ceramic coatings due to their stiffness and inability to comply with compressive lateral forces [47, 70, 82]. The lack of lamellar structure in the YSZ deposits can be detrimental to their lifetime because vertically aligned micro-cracks are not generated. Vertical cracks can be formed by curved lamellar features unable to slide past one

another or by connecting interlamellar voids [43, 44, 55]. The deposit cannot employ interfacial sliding or effectively create compliant vertical cracks without the lamellar structure.

5.2.2 Hardness, Young's Modulus

The F-test reported that the hardness and stiffness are not functions of the position in the deposit. If any gradient is present across the width or thickness of the deposit, it is lost in the variation caused by the irregularities of the microstructure. The nanoindentation technique is very sensitive to surface features. The 303 SS substrate's measured mechanical properties are comparable to the established bulk values because the substrate is dense and free of any surface irregularities.

The large Young's Modulus value for the Ni-based alloy deposit probably indicates that the maximum load was chosen incorrectly. Studies have shown Ni-5wt%Al plasma spray coatings have much higher stiffness than the composition in this study [19]. Any increase in aluminum at specific regions may cause a change in mechanical properties. The EDS results show that within the deposit the aluminum content is less than 1wt%, which is similar to the feed powder composition. Also, the indents were at removed locations from the substrate-deposit interface where the regions of high aluminum content are concentrated. The measured mechanical properties are assumed to be wrong due to the error of the experimental conditions. The variance in maximum depth, or penetration depth, is likely caused by the surface topography. The penetration depth can introduce large error to the measured hardness as seen in Equations 2.5 and 2.6.

The measured mechanical properties for the Ni-based alloy are considered inaccurate and will not be used for analysis. But, the variance and load-displacement curves can be used to evaluate the behavior of the deposit. The rough loading curves seen in the Ni-based alloy are most likely due to dislocations impeding plastic flow or nano-sized pores as discussed in Section 2.4.1.

The YSZ deposits have two indents that were clearly affected by large surface features. Other indents may be effected but they are hard to identify due to the large data variance and because the indents could not be visually inspected. The loading curves are elongated and have discontinuities that show the porosity of the sample. The mechanical properties measured are smaller than the published bulk values. Previous studies attribute low measured mechanical properties to nano-sized pores and cracks. SEM images of the deposits do report nano-sized pores and cracks which should reduce the stiffness of the material. However, the deposits do not experience vertical cracking, which has been reported to efficiently reduce the stiffness of the system as discussed in Sections 2.3.3 and 5.2.1.

Nanoindentation's ability to measure the Young's modulus of plasma spray coatings is complicated by its sensitivity to residual stresses, surface features, and experimental conditions. It often reports much higher values than seen by in-situ curvature or bend tests [83]. Previous reports show that the Young's modulus for metallic plasma spray coatings can be a third of the bulk value and for ceramic coatings as low as a sixth of the bulk value [48]. The absolute value measured by these techniques may not be an accurate representation of the material. The YSZ deposit does report higher stiffness values when compared to other nanoindentation studies of YSZ plasma spray coatings [83]. The increased stiffness of the YSZ deposits is not beneficial for the attachment of fiber optic sensors and can contribute to the short cyclic thermal lifetime.

5.2.3 Adhesion and Thermal Cycling

The scratch test shows the different dominant failure modes for the two types of material deposits. The ceramic deposit reports a larger adhesion strength but failure is catastrophic and buckling and delamination is visible. The Ni-based alloy deposit shows a smaller adhesion strength but the failure was local and difficult to visually inspect. The failure modes of these two types of material are important to understand the attachment lifetime of the sensor. If the metal deposit fails at a single point during thermal

loading, it is probable that the fiber will remain attached to the substrate. However, the attachment of the fiber is threatened if the deposit fails by buckling or cracking.

The Ni-based alloy system showed no sign of failure after twenty loads and is believed to maintain attachment of the sensor for extensive use at elevated temperatures. The dominant relaxation mechanisms in the system allow for the sensor to remain attached under large thermal stresses. The deposit may be experiencing delamination that could hinder the strain transfer. Future work needs to be completed to determine the effect of host-fiber separation on the strain transfer fidelity.

The failure of the YSZ deposit during thermal cycling provides more evidence of the material's inability to comply with the CTE mismatch. The sensor cannot be used after failure and, therefore, the system cannot be used in the intended application reliably for extended operation. The YSZ deposit showed cohesion and adhesion failure after thermally cycling. The adhesion failure was located near the fiber at the front of the deposit and caused spalling parallel to the length of the fiber. Cohesion failure was observed along the side of the thick portion of the deposit. The failure agrees with previous results that thicker coatings fail first [54]. The failure mode of the deposit indicates the stress of the failure. Brittle coatings on ductile substrates will experience buckling if in compression and cracking or decohesion if in tension. The deposit ultimately failed from compressive forces causing buckling and spallation because decohesion did not occur prior to spalling.

5.3 Thermal Stress

5.3.1 Raman results for deposit

Previous *in-situ* stress Raman studies of tetragonal YSZ coatings show a peak shift to lower wavenumbers during the application of a tensile force. The YSZ peak commonly analyzed for stress, located approximately at 640cm^{-1}, is not well defined in the collected spectra and cannot be used in this assessment [49, 67, 80]. The monoclinic peaks are more dominant and easily fitted for analysis but have

not been previously documented with this technique. The deposit is interpreted to have experienced a tensile force if the monoclinic peak recorded at ≈287cm^{-1} follows the same trend as the tetragonal peaks. Because the initial stress state is not known, the deposit could be relaxing to a less compressive state or to a tensile state.

Teixeira et al. reported that subsequent heat treatments add a compressive force for YSZ coatings due stresses induced during cooling [53]. Because the deposits exhibited a stress shift in the tensile direction, the compressive forces must have been relaxed at room temperature or were subordinate to relaxation and tensile forces at elevated temperatures. The samples did not exhibit delamination or cracking at room temperature after a single thermal load, which would have alleviated any compressive forces induced during cooling.

The compressive forces during cooling were not large enough to counteract the relaxation mechanisms at elevated temperatures, which were more efficient due to the geometric shape and the inclusion of the encapsulated fiber [56, 84]. Point defect and dislocation movement to both the fiber cavity and out of the surface of the deposit may allow for a more extensive relaxation at elevated temperatures than was observed in the pure, flat and semi-infinite coatings. If the relaxation is more dominant than the compressive force caused during cooling, the samples will report a stress shift in the tensile direction.

The deposit eventually failed from compressive forces indicating that the stress state must have changed with subsequent thermal loads. This is caused by relaxation mechanisms becoming inefficient at elevated temperatures over time. After a single load the material is capable of utilizing extensive cracking to relieve the system, which counteracts the compressive stresses during cooling. YSZ coatings experience sintering that will effectively decrease crack growth and nucleation after continuous thermal cycling [55]. If the material is unable to relax efficiently, the compressive forces during cooling can then build with

each thermal cycle to eventually cause failure [53]. The number of cycles to effectively stop relaxation mechanisms at elevated temperatures depends on the stiffness of the material.

The monoclinic peaks observed in the spectra indicate that the YSZ deposits were not treated to produce the untransformable tetragonal phase. The untransformable tetragonal phase is only formed under certain processing conditions. The monoclinic to tetragonal phase transition will induce a volume change that will introduce a larger thermal stress than anticipated. The extent of damage induced from the volume change is unclear and could contribute to both the fiber and deposit failure. Previous reports attribute the increase in thermal cyclic lifetime of partially stabilized zirconia to the untransformable tetragonal phase. A shorter thermal cyclic life can be expected for samples without this phase. The processing conditions should be altered to produce the untransformable tetragonal phase for long term fiber attachment.

5.3.2 Modeling

Stress Distribution for Ni-based alloy and YSZ system

The Ni-based alloy and YSZ deposit models produced unique stress distributions due to their different mechanical and thermal properties. The Ni-based alloy is much more compliant and experiences a slightly smaller CTE mismatch with the steel substrate than YSZ. Therefore, the substrate-deposit interface experiences lower maximum thermal stress in the Ni-based alloy model. The highest stress in the system was experienced at the fiber-tube interface, which has the largest CTE mismatch. The deposit-fiber interface has the second largest CTE mismatch. However, the substrate-deposit interface experiences a greater stress than the deposit-fiber interface. This is attributed to the substrate being stiffer than the fiber. Therefore, both the CTE mismatch and the stiffness of the components are significant factors to the thermal stress. Figure 5.3 shows the stress distribution for the Ni-based alloy model at 700^{o}C for two different geometric models.

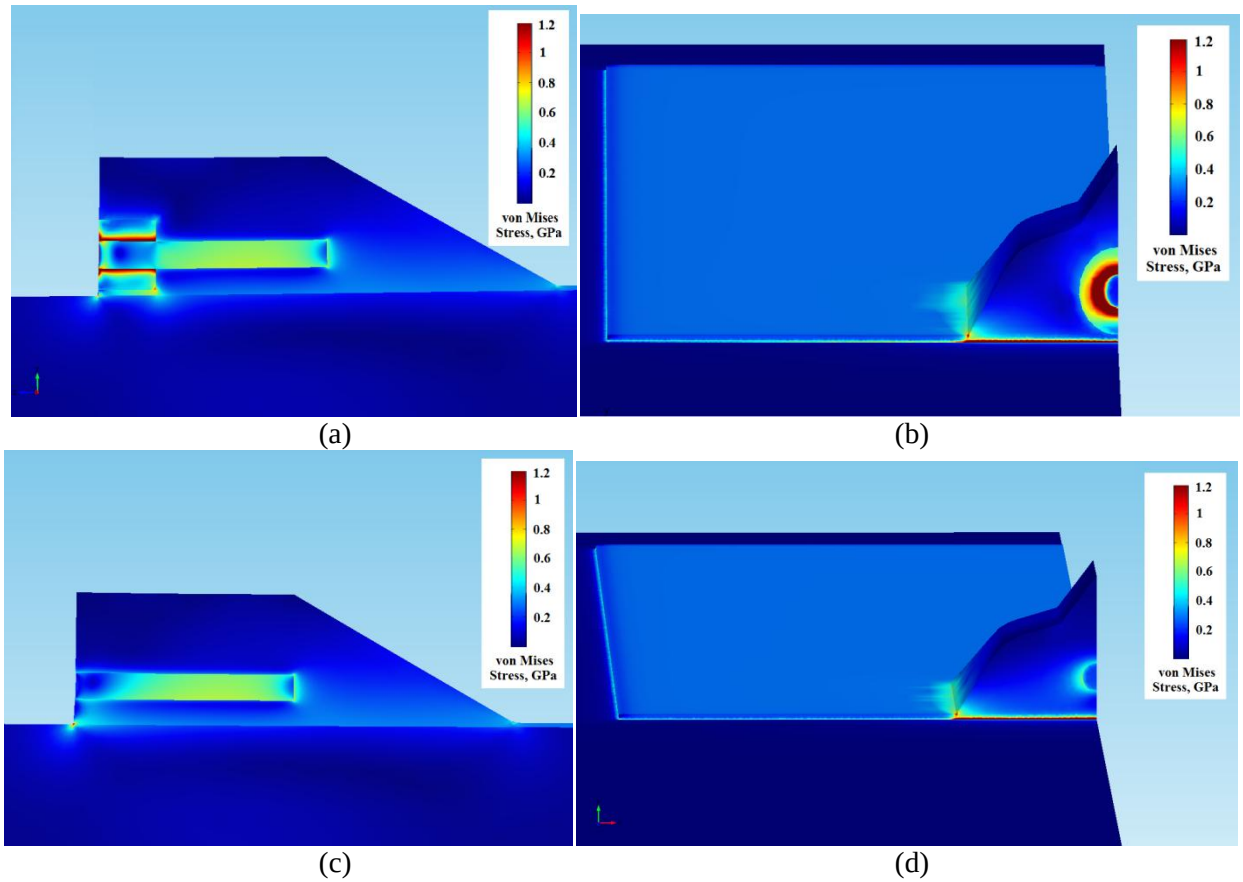

Figure 5.3: The von Mises stress distribution from a cross sectional view for the Ni-based alloy with the (a) 0.25 304SS tube geometric model and the (c) no tube geometric model and the front view for both models in (b) and (d), respectively.

Complete detachment along the substrate-deposit interface in the Ni-based alloy system is unlikely because the thermal stresses are greater than the adhesion strength only at temperatures above 630^{o}C. Surface diffusion and creep would be the prevalent relaxation mechanism at these temperatures. However, the fiber could fracture due to the large radial stresses induced by the steel tube.

The YSZ deposit system reports much higher thermal stresses at the substrate-deposit interface. The ceramic cannot comply with the expansion rate of the substrate at elevated temperatures. The deposit is more likely to fail catastrophically after only a few thermal cycles because the thermal stresses exceed the adhesion strength at temperatures as low as 390^{o}C. The material or deposit would need to be altered for more compliance. Figure 5.4 shows the stress distribution along the fiber for the YSZ model. The stresses

along the fiber are great enough to cause fracture at elevated temperatures. Both material systems show a stress concentration at the encapsulated end face of the fiber.

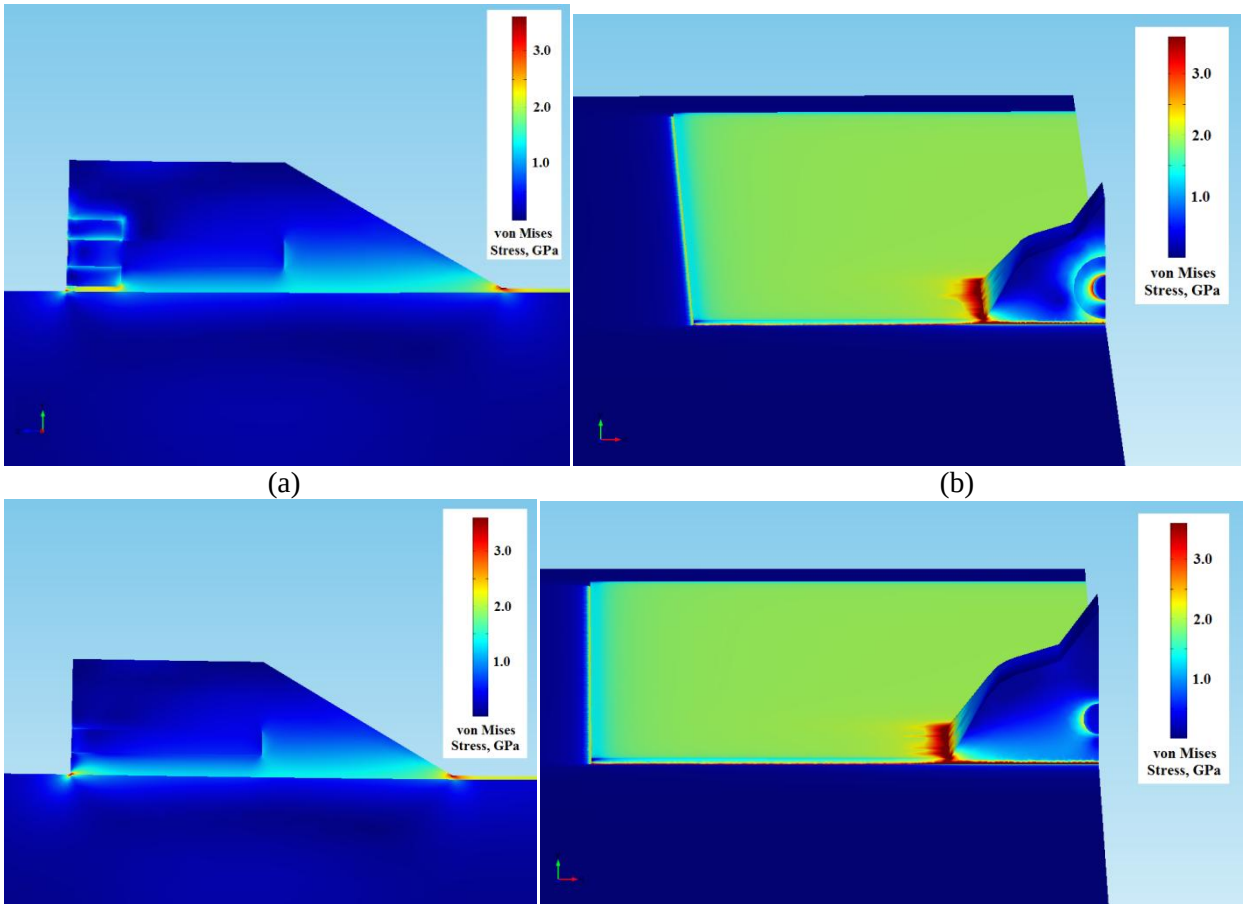

Figure 5.4: The von Mises stress distribution from a cross sectional view for the YSZ deposit and the (a) 0.25 304 SS tubing and (b) no tube geometric models and a front view for both models in (b) and (d), respectively.

The calculated stress, in both material models, does not greatly decrease until temperatures below 40^{o}C, when the cooling rate is much slower. The magnitude of the remaining stress after the thermal load is unclear because no boundary condition is provided for the cooling time. Residual stresses from the thermal cycling will build upon one another to eventually cause failure. The residual stresses from processing were not included in this model but will also contribute to the stress distribution.

Tubing

In each material model, the protective tube introduces a stress concentration along the fiber, as seen in Figure 5.3 and 5.4. The introduced stress is located at the deposit end face which is a common initiation location for failure. The tube length does not greatly change the magnitude of the maximum von Mises stresses at the various edges in the models, as seen in Figures 4.21 and 4.24. However, the length of the tube does change how much of the fiber is exposed to the applied stress. For the longer tubes, the stress will be more likely to be located at regions of imperfections in the fiber that are more prone to fracture. Future testing of the signal during extended thermal cycling can indicate if the fiber does fracture. The length of the tube might need to be minimized if the fiber fails during operation. A tube should not be used if it does not aid in the protection of the fiber during processing because of the increased stress state of the fiber.

The stress distributions, seen in Figures 5.3 and 5.4, indicate that delamination is possible along the tube-deposit interface, which could hinder the strain transfer. Therefore, the tubing may have to be positioned away from the sensor head cavity to ensure that the fiber will be able to measure strain accurately. The calculated stresses along the tube's interior may explain the fracture seen in the SEM images. The plasma spray process may have induced large thermal stresses that weakened the tube and made it more susceptible to pull out during sample preparation. Failure of the tube's interior could hurt the fiber and also weaken the strain transfer fidelity.

The tubing material has a great effect on the thermal stress values for the Ni-based alloy system. Materials with larger CTE values will help extend the thermal cyclic lifetime of the substrate-deposit interface. However, these materials will increase the forces along the fiber-tube edge. These stresses surpass the compressive strength of the fiber at room temperature, and previous studies report that the strength of fused silica decreases at elevated temperatures. Therefore, tubes with moderate or low CTE values should be used to maintain the integrity of the fiber.

The optimum tubing material was the same for both material systems. This is because the deposits have similar CTE values, and the stress distribution was optimized by choosing a tube with a moderate CTE value. A larger change in the stress magnitude was calculated for the YSZ system because of the stiffness of the material. A tube made of alumina or Hastelloy B-2 would decrease the stress along the fiber and maintain a lower stress at the substrate-deposit interface. Silica tubing would also allow for low values of thermal stress because it has a low stiffness. However, the compressive strength of silica will limit its ability as a tubing material to protect the fiber during the plasma spray process.

Porosity

The change in stiffness of the YSZ deposit greatly altered the maximum stress at the substrate-deposit interface. The great increase in compliance allowed for a larger change in stress than seen in the Ni-based alloy with the same increase in porosity. Increased porosity will add more compliance to the sample and indirectly decrease the thermal stresses developed during cyclic loading. Porosity may also allow for stiffer materials to be used for encapsulating optical fibers. However, porosity can decrease the fiber's protection from corrosive species. Materials with lower Young's modulus should be preferred for fiber encapsulation.

The fiber-tube edge was the only interface that experienced an increase in stress with increasing porosity. The increase in stress at this edge is unexpected for both systems because neither component is directly altered by an increase in compliance of the deposit. The increase of strain at this interface could be an effect from the individual components' change in stress state. The increase is not believed to be great enough to alter the behavior of the deposit but may affect the fiber.

Effect of CTE Change in Ni-based Alloy Deposit

The Ni-based alloy deposit with a hypothetical low CTE value had the largest calculated von Mises stresses. During heating, the substrate's expansion will induce a large tensile stress on the deposit at the

substrate-deposit interface because the deposit is resisting displacement. This stress is translated throughout the entire deposit. Although the CTE mismatch is small between the deposit and fiber, a large stress is calculated at the interface because of the overall stress in the system. The tensile stress at the interface decreases with the deposit's CTE increase, as seen in Figure 4.27. The tube-deposit interface will experience a similar decrease in stress as the substrate-deposit interface because the tubing has similar material properties to the substrate.

The model shows that the stress at the deposit-fiber interface can be optimized by using a deposit with a moderate CTE value, such as the two deposit materials modeled. The stress increases as the CTE mismatch increases. The stress along the fiber cannot be minimized with a deposit that has a lower CTE because the stress induced from a large substrate-deposit mismatch dominates the stress profile of the entire system. The stress at the fiber-tube edge can be considered constant because neither component is directly altered by the change in the deposit's thermal properties.

A deposit with the CTE value between 12 and 15 μm/(m·K) is the best for the system because it lowers the stress along the fiber to below the compressive strength of silica and allows a low stress at the substrate-deposit interface. The optimum CTE may be dependent on the stiffness of the deposit material.

6. Conclusions

The IFPI sensors in this study must be altered in their design to be attached with these deposits. Debonding is likely to occur between the deposit and the fiber's end face for all material systems due to thermal stresses induced from mismatches in CTE. Therefore, the fibers must be modified for this attachment method since the optimum system will still cause signal distortion. The second reflective surface cannot be the end face of the fiber. The cavity should be moved to the middle of the fiber or the end of the fiber should be modified to kill all signal reflected from beyond the end of the fiber. This would allow for the deposit to debond from the end face without causing signal distortion and allow for the deposits to be used for attachment. The debonding at this interface does not interfere with strain transfer fidelity or the attachment of the fiber to a host structure.

The processing conditions of the Ni-alloy deposit are promising for application but may require some changes for a better failure rate. The fiber fabrication and the tubing implementation are assumed to be consistent for all of the encapsulated fibers. Therefore, the increase in fiber fracture by encapsulation with the YSZ deposits cannot be considered random noise or independent of the deposition process. The YSZ deposit cannot be used for fiber attachment due to the harsh processing conditions that caused deformation. The tubing did not provide sufficient protection of the sensor head, although the cross sectional images show that the tubing is resistant to deformation from processing. Future testing should be completed to analyze if the tube's placement can prevent fracture during processing.

The closed porosity of the YSZ deposit might add more compliance to the system without providing a path for corrosive species. However, the lack of a lamellar structure decreases the deposit's ability to relax by non-catastrophic failure modes. The micro-cracks nucleate at the pores. Interlamellar voids would allow for the micro-cracks to be vertical and more effectively add compliance to the system. The

random nature of the pores cannot increase the Young's modulus as effectively as seen in other YSZ systems.

A more defined lamellar structure is observed within the Ni-based alloy system. The Ni-based alloy deposit system benefits from the relaxation mechanisms dominate in metallic coatings and lamellar microstructures. Creep and plastic flow will relieve the system at elevated temperatures and decrease the need for catastrophic failure modes at low temperatures. The porosity of the Ni-based alloy may cause corrosive cohesion failure. These interlamellar voids could introduce oxide deposits sites, which lead to brittle fracture. Corrosion studies should be completed to determine how the porosity affects the cyclic lifetime of the deposit.

The Raman spectroscopy data suggests that the YSZ deposit does relax at elevated temperatures. However, the monoclinic peaks indicate that the material will experience a phase change under the operational temperatures. The associated phase change could introduce large thermal stresses, which cause failure.

Micro-cracking is the dominant relaxation mechanism in ceramic coatings but is insufficient to relieve the entire system. Interfacial sliding is another non-catastrophic failure mechanism that can be employed in ceramic systems under compressive stress but cannot be used by these YSZ deposits due to their microstructure. The system could not fully relax, and the compressive forces began to build with each subsequent thermal load to eventually cause failure by buckling. The Ni-based alloy showed only local failure during scratch testing and did not allow detachment during thermal cycling. The failure modes of the deposit allow for fiber attachment for long term operation.

The calculated stresses from modeling show the importance of both the stiffness and the CTE of the components. The ductility of the deposit lowers the thermal stress in the system as well as allowing for

favorable dominant relaxation mechanisms. A moderate CTE value is desirable for the deposit to allow for a lower CTE mismatch with the substrate and reduce the stresses along the fiber. A high melting point metallic deposit, similar to the Ni-based alloy, is desirable for fiber optic attachment due to its ductility, CTE value, and dominant relaxation mechanisms.

The protective tubing imposes large strains on the fiber, which can cause fracture. The tubing length and material need to be altered to allow for protection of the fiber during processing and for use at elevated temperatures. Hastelloy B-2, a nickel-based superalloy, or alumina tubing may maintain the integrity of the fiber while lowering the stress at the substrate-deposit interface. Studies should be done to determine if the tubing actually does provide protection of the fiber during processing and if the placement can be optimized. Other restraining techniques should be investigated if the tubing does not provide protection.

The debonding of the fibers at elevated temperatures may hurt the resolution of the sensor. Many models have been devised for embedded fibers to determine the absolute stresses imposed to cause debonding. However, there has not been sufficient research documented on the effect of debonding on the strain accuracy. Future studies should be completed to determine the sensitivity of the IFPI sensors to separation from the host.

7. References

1. Sirkis, J., T.A. Berkoff, R.T. Jones, H. Singh, A.D. Kersey, E.J. Friebele, and M.A. Putnam, *In-line fiber etalon (ILFE) fiber-optic strain sensors.* Lightwave Technology, Journal of, 1995. **13**(7): p. 1256-1263.
2. Li, H.-N., D.-S. Li, and G.-B. Song, *Recent applications of fiber optic sensors to health monitoring in civil engineering.* Engineering Structures, 2004. **26**(11): p. 1647-1657.
3. Measures, R.M., *Structural monitoring with fiber optic technology*. 2001, San Diego, CA: Academic.
4. Udd, E., *Fiber optic smart structures*. 1995, New York: Wiley.
5. Henkel, D.P. *Microstructure of high temperature smart materials*. in *Smart Structures and Materials 1993: Smart Materials*. 1993. Albuquerque, NM: The Society.
6. Wnuk, V.P., A. Mendez, S. Ferguson, and T. Graver, *Process for mounting and packaging of fiber Bragg grating strain sensors for use in harsh environment applications*. in *Smart Structures and Materials 2005: Smart Sensor Technology and Measurement Systems*. 2005. San Diego.
7. Narendran, N. and J.M. Weiss, *Field Mountable Fiber Optic Sensor*. 1997, Electric Power Research Institute: United States.
8. Rao, Y.-J., *Recent progress in fiber-optic extrinsic Fabry–Perot interferometric sensors.* Optical Fiber Technology, 2006. **12**(3): p. 227-237.
9. Taylor, H.F., *Fiber Optic Sensors Based upon the Fabry-Perot Interferometer*, in *Fiber Optic Sensors, Second Edition*, S. Yin, P.B. Ruffin, and F.T.S. Yu, Editors. 2008, CRC Press: Boca Raton, Florida. p. 35-64.
10. Bhatia, V., K.A. Murphy, R.O. Claus, T.A. Tran, J.A. Greene, *Recent developments in optical-fiber-based extrinsic Fabry-Perot interferometric strain sensing technology.* Smart Materials and Structures, 1995. **4**(4): p. 246.
11. Habel, W.R. and A. Bismarck, *Optimization of the adhesion of fiber-optic strain sensors embedded in cement matrices; a study into long-term fiber strength.* Journal of Structural Control, 2000. **7**(1): p. 51-76.
12. Farshad, M., *Intelligent Materials and Structures.* Scientia Iranica, 1995. **2**(1): p. 65-68.
13. Measures, R.M., K. Liu, and S. Melle. *Fiber Optic Sensing System Critical Issues and Developments for Smart Structures*. in *ADPA AIAA ASME Spie Conference on Active Materials and Adaptive Structures*. 1992. Alexandria, Virginia: Institute of Physics Pub.
14. Hadjiprocopiou, M., G.T. Reed, L. Hollaway, A.M. Thorne, *Optimization of coating properties for fiber optic smart structures using finite element analysis*. 1995: The Society.
15. Highsmith, A.L., D. Shin, and R.A. Naik, *Local stresses in metal matrix composites subjected to thermal and mechanical loading*, in *Thermal and Mechanical Behavior of Metal Matrix and Ceramic Matrix Composites*, J.M. Kennedy, H.H. Moeller, and W.S. Johnson, Editors. 1990, Americal Society for Testing and Materials: Philadelphia, PA. p. 3-19.
16. Natesan, K., *Applications of coatings in coal-fired energy systems.* Surface and Coatings Technology, 1993. **56**(3): p. 185-197.
17. Heimann, R.B., *Plasma-spray coating : principles and applications*. 1996, Weinheim; New York: VCH.
18. Stern, K.H., *Metallurgical and ceramic protective coatings*. 1996, London; New York: Chapman & Hall.
19. Kesler, O., M. Finot, S. Suresh, and S. Sampath, *Determination of processing-induced stresses and properties of layered and graded coatings: Experimental method and results for plasma-sprayed Ni---Al2O3.* Acta Materialia, 1997. **45**(8): p. 3123-3134.
20. Grattan, K.T.V. and T. Sun, *Fiber optic sensor technology: an overview.* Sensors and Actuators A: Physical, 2000. **82**(1–3): p. 40-61.

21. Measures, R.M., *Fiber optic sensing for composite smart structures.* Composites Engineering, 1993. **3**(7–8): p. 715-750.
22. Chen, X., F. Shen, Z. Wang, Z. Huang, A. Wang, *Micro-air-gap based intrinsic Fabry-Perot interferometric fiber-optic sensor.* Appl. Opt., 2006. **45**(30): p. 7760-7766.
23. Wang, Z., *Intrinsic Fabry-Perot interferometric fiber sensor based on ultra-short Bragg gratings for quasi-distributed strain and temperature measurements*. 2006, Virginia Polytechnic Institute and State University: Blacksburg, VA. p. 129.
24. Kuang, K. and W. Cantwell, *Use of conventional optical fibers and fiber Bragg gratings for damage detection in advanced composite structures: A review.* Applied Mechanics Reviews, 2003. **56**(5): p. 493-513.
25. Levin, K. and S. Nilsson. *Analysis of the local stress field in a composite material with an embedded extrinsic Fabry-Perot interometer (EFPI) sensor*. in *Second European Conference on Smart Structures and Materials*. 1994. Glasgow, United Kingdom: SPIE - International Society for Optical Engineering.
26. Ansari, F., *Structural health monitoring with fiber optic sensors.* Frontiers of Mechanical Engineering in China, 2009. **4**(2): p. 103-110.
27. Kennedy, J.M., H.H. Moeller, and W.S. Johnson, eds. *Thermal and Mechanical Behavior of Metal Matrix and Ceramic Matrix Composites*. 1990, Americal Society for Testing and Materials: Baltimore.
28. Zhou, G. and L.M. Sim, *Damage detection and assessment in fibre-reinforced composite structures with embedded fibre optic sensors-review.* Smart Materials and Structures, 2002. **11**(6): p. 925.
29. Kelley, K.C., *Ceramic Adhesive*. 1995, Caterpillar Inc.: United States.
30. Latini, V., V. Striano, F. Venditti, G. Coppola, and I. Rendina, *Fiber Optic Health Monitoring System for Aerospace Hot Structures*. in *Thermal Protection Systems and Hot Structures*. 2006. Noordwijk, The Netherlands: European Space Agency.
31. Huston, D., *Distributed and Noncontact Sensors*, in *Structural Sensing, Health Monitoring, and Performance Evaluation*. 2010, Taylor & Francis. p. 77-174.
32. Sampath, S. and H. Herman, *Rapid solidification and microstructure development during plasma spray deposition.* Journal of Thermal Spray Technology, 1996. **5**(4): p. 445-456.
33. Davis, J.R., Associates, and A.S.M.I.T.S.S.T. Committee, *Handbook of thermal spray technology*. 2004, Materials Park, OH: ASM International.
34. Steffens, H.D., B. Wielage, and J. Drozak, *Interface phenomena and bonding mechanism of thermally-sprayed metal and ceramic composites.* Surface and Coatings Technology, 1991. **45**(1-3): p. 299-308.
35. Parco, M., L. Zhao, J. Zwick, K. Bobzin, E. Lugscheider, *Investigation of particle flattening behaviour and bonding mechanisms of APS sprayed coatings on magnesium alloys.* Surface and Coatings Technology, 2007. **201**(14): p. 6290-6296.
36. Houben, J., *Relation of the adhesion of plasma sprayed coatings to the process parameters size, velocity and heat content of the spray particles*. 1988, Technische Universiteit Eindhoven: Eindhoven.
37. Bahbou, M., P. Nylén, and J. Wigren, *Effect of grit blasting and spraying angle on the adhesion strength of a plasma-sprayed coating.* Journal of Thermal Spray Technology, 2004. **13**(4): p. 508-514.
38. Pawlowski, L., *Science and Engineering of Thermal Spray Coatings (2nd Edition)*, John Wiley & Sons. p. 475.
39. Fauchais, P., A. Vardelle, and M. Vardelle, *Modelling of plasma spraying of ceramic coatings at atmospheric pressure.* Ceramics International, 1991. **17**(6): p. 367-379.
40. Terry, S.G., J.R. Litty, and C.G. Carlos, *Evolution of porosity and texture in thermal barrier coatings grown by EB-PVD*, in *Elevated temperature coatings: Science and technology III; Sumposium on High Temperature Coatings III*. 1999: San Diego, CA. p. 13-25.

41. Berndt, C.C., J. Karthikeyan, Y.D. Jun, and R. Ratnaraj, *Material Property Variations in Thermally Sprayed Coatings*, in *Thermal Spray Coatings: Properties, Processes and Applications*, T.F. Bernecki, Editor. 1991: Pittsburgh, PA.
42. Bordeaux, F., R.G. Saint-Jacques, C. Moreau, S. Dallaire, and J. Lu, *Thermal Shock Resistance of TiC coatings Plasma-Sprayed on Macroroughened Substrates*. in *Thermal spray coatings; properties, processes, and applications*. 1991. Pittsburg, PA: ASM International.
43. Padture, N.P., K.W. Schilichting, T. Bhatia, A. Ozturk, B. Cetegen, E.H. Jordan, M. Gell, S. Jiang, T.D. Xiao, P.R. Strutt, E. Garcia, P. Miranzo, and M.I. Osendi, *Towards durable thermal barrier coatings with novel microstructures deposited by solution-precursor plasma spray.* Acta Materialia, 2001. **49**(12): p. 2251-2257.
44. Levit, M., I. Grimberg, and B.Z. Weiss, *Residual stresses in ceramic plasma-sprayed thermal barrier coatings: measurement and calculation.* Materials Science and Engineering A, 1996. **206**(1): p. 30-38.
45. Matejicek, J., S. Sampath, P.C. Brand, and H.J. Prask, *Quenching, thermal and residual stress in plasma sprayed deposits: NiCrAlY and YSZ coatings.* Acta Materialia, 1999. **47**(2): p. 607-617.
46. Miller, R.A. and C.E. Lowell, *Failure mechanisms of thermal barrier coatings exposed to elevated temperatures.* Thin Solid Films, 1982. **95**(3): p. 265-273.
47. Gill, S. and T. Clyne, *Stress distributions and material response in thermal spraying of metallic and ceramic deposits.* Metallurgical and Materials Transactions B, 1990. **21**(2): p. 377-385.
48. Kuroda, S. and T.W. Clyne, *The quenching stress in thermally sprayed coatings.* Thin Solid Films, 1991. **200**(1): p. 49-66.
49. Teixeira, V., M. Andritschky, W. Fischer, H.P. Buckremer, and D. Stover, *Analysis of residual stresses in thermal barrier coatings.* Journal of Materials Processing Technology, 1999. **92–93**(0): p. 209-216.
50. Nied, H.A. *Edge stress concentrations in layered ceramic-metal composites due to thermal mismatch*. in *Thermal spray coatings: properties, processes and applications*. 1991. Pittsburg, PA: ASM International.
51. Ho, S. and E. Lavernia, *Thermal residual stresses in functionally graded and layered 6061 Al/SiC materials.* Metallurgical and Materials Transactions A, 1996. **27**(10): p. 3241-3249.
52. Finot, M. and S. Suresh, *Small and large deformation of thick and thin-film multi-layers: Effects of layer geometry, plasticity and compositional gradients.* Journal of the mechanics and physics of solids, 1996. **44**(5): p. 683-721.
53. Teixeira, V.,M. Andritschky, W. Fischer, H.P. Buchkremer, and D. Stover, *Effects of deposition temperature and thermal cycling on residual stress state in zirconia-based thermal barrier coatings.* Surface and Coatings Technology, 1999. **120-121**(0): p. 103-111.
54. Wiklund, U., J. Gunnars, and S. Hogmark, *Influence of residual stresses on fracture and delamination of thin hard coatings.* Wear, 1999. **232**(2): p. 262-269.
55. Tang, F. and J.M. Schoenung, *Evolution of Young's modulus of air plasma sprayed yttria-stabilized zirconia in thermally cycled thermal barrier coatings.* Scripta Materialia, 2006. **54**(9): p. 1587-1592.
56. Povirk, G.L., A. Needleman, and S.R. Nutt, *An analysis of residual stress formation in whisker-reinforced Al・SiC composites.* Materials science & engineering. A, Structural materials : properties, microstructure and processing, 1990. **125**(2): p. 129-140.
57. Taylor, T.A. and R.E. Taylor, *Testing of stability and thermal properties of thermal barrier coatings*, in *ASM Handbook - Surface Engineering*, A.I.H. Committee, Editor. 1994, ASM International: Materials Park, OH. p. 654-659.
58. Jones, R.L., *Improved tetragonal phase stability at 1400°C with scandia, yttria-stabilized zirconia.* Surface & coatings technology, 1996. **86-87**: p. 94-101.
59. Scott, H.G., *Phase relationships in the zirconia-yttria system.* Journal of Materials Science, 1975. **10**(9): p. 1527-1535.
60. Schuh, C.A., *Nanoindentation studies of materials.* Materials Today, 2006. **9**(5): p. 32-40.

61. Bull, S.J., *Nanoindentation of coatings.* Journal of Physics D: Applied Physics, 2005. **38**(24): p. R393.
62. Jang, B.-K. and H. Matsubara, *Influence of porosity on hardness and Young's modulus of nanoporous EB-PVD TBCs by nanoindentation.* Materials Letters, 2005. **59**(27): p. 3462-3466.
63. Lu, X.J., X. Wang, and P. Xiao, *Nanoindentation and residual stress measurements of yttria-stablized zirconia composite coatings produced by electrophoretic deposition.* Thin Solid Films, 2006. **494**(1–2): p. 223-227.
64. Matejicek, J., S. Sampath, and J. Dubsky, *X-ray residual stress measurement in metallic and ceramic plasma sprayed coatings.* Journal of Thermal Spray Technology, 1998. **7**(4): p. 489-496.
65. Sue, J.A. and G.S. Schajer, *Stress Determination for Coatings*, in *ASM handbook*, A. Committee, Editor. 1994, ASM International: Materials Park, OH. p. 647-653.
66. Das, R.S. and Y.K. Agrawal, *Raman spectroscopy: Recent advancements, techniques and applications.* Vibrational Spectroscopy, 2011. **57**(2): p. 163-176.
67. Tomimatsu, T., Y. Kagawa, and S.J. Zhu, *Residual stress distribution in electron beam-physical vapor deposited ZrO(2) thermal barrier coating layer by Raman spectroscopy.* Metallurgical and materials transactions. A, Physical metallurgy and materials science, 2003. **34A**(8): p. 1739.
68. Saber-Samandari, S. and K.A. Gross, *Nanoindentation reveals mechanical properties within thermally sprayed hydroxyapatite coatings.* Surface and Coatings Technology, 2009. **203**(12): p. 1660-1664.
69. Drory, M.D. and J.W. Hutchinson, *Measurement of the Adhesion of a Brittle Film on a Ductile Substrate by Indentation.* Proceedings of the Royal Society of London. Series A: Mathematical, Physical and Engineering Sciences, 1996. **452**(1953): p. 2319-2341.
70. Berndt, C.C. and C.K. Lin, *Measurement of adhesion for thermally sprayed materials.* Journal of Adhesion Science and Technology, 1993. **7**(12): p. 1235-1264.
71. American Society for, T. and Materials, *Annual book of ASTM standards.* Annual book of ASTM standards., 1970.
72. Chalker, P.R., S.J. Bull, and D.S. Rickerby, *A review of the methods for the evaluation of coating-substrate adhesion.* Materials Science and Engineering: A, 1991. **140**: p. 583-592.
73. Xie, Y. and H.M. Hawthorne, *A model for compressive coating stresses in the scratch adhesion test.* Surface and Coatings Technology, 2001. **141**(1): p. 15-25.
74. Das, D.K., M.P. Srivastava, S.V. Joshi, and R. Sivakumar, *Scratch adhesion testing of plasma-sprayed yttria-stabilized zirconia coatings.* Surface and Coatings Technology, 1991. **46**(3): p. 331-345.
75. Pawlowski, L., D. Lombard, and P. Fauchais, *Structure-thermal properties---relationship in plasma sprayed zirconia coatings.* Journal of Vacuum Science & Technology A: Vacuum, Surfaces, and Films, 1985. **3**(6): p. 2494-2500.
76. Kipp, D.O., *Metal Material Data Sheets*. 2011, MatWeb - Division of Automation Creation, Inc.
77. Bansal, N.P. and R.H. Doremus, *Handbook of glass properties*. 1986, Orlando: Academic Press.
78. Kingery, W.D., H.K. Bowen, and D.R. Uhlmann, *Introduction to Ceramics*. 2nd Edition ed. 1960, New York: John Wiley & Sons, Inc.
79. Sodeoka, S., M. Suzuki, and K. Ueno, *Effects of high-pressure plasma spraying for yttria-stabilized zirconia coating.* Journal of Thermal Spray Technology, 1996. **5**(3): p. 277-282.
80. Cai, J., *Stabilized cubic zirconia: A Raman study under uniaxial stress.* Applied Physics Letters, 1993. **62**(22): p. 2781.
81. Hass, D.D., *Directed Vapor Deposition of Thermal Barrier Coatings*. 2000, University of Virginia: Charlottesville. p. 256.
82. Robin, P.,F. Gitzhofer, P. Fauchais, and M. Boulos, *Remaining Fatigue Life Assessment of Plasma Sprayed Thermal Barrier Coatings.* Journal of Thermal Spray Technology, 2010. **19**(5): p. 911-920.
83. Thompson, J.A. and T.W. Clyne, *The effect of heat treatment on the stiffness of zirconia top coats in plasma-sprayed TBCs.* Acta Materialia, 2001. **49**(9): p. 1565-1575.

84. Cao, G. and Y. Wang, *Nanostructures & nanomaterials : synthesis, properties, and applications*. 2011, New Jersey: World Scientific.

Appendix A: Fabrication Process and Description of Intrinsic Fabry-Perot Interferometric (IFPI) Sensors

The sensors were fabricated at the Center for Photonics Technology at Virginia Tech out of single mode fused silica fibers (SMF-28^{TM} by Corning®) according to Chen et al. [22]. The fibers were etched with hydrofluoric acid of either 5wt% or 50wt%. Then two different etched fibers were fused together by splicing. The splicing process allows for different fibers to be aligned and fused together to make one coherent fiber. An air gap is created in between the fibers because the end faces are not flat after etching, as depicted in Figure A1.

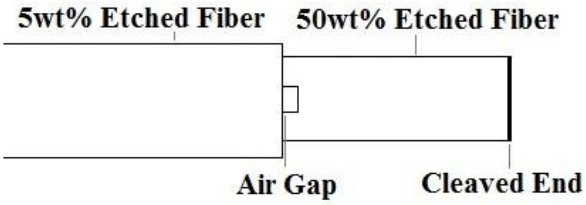

Figure A1: Diagram of IFPI sensors created for strain measurement.

The air gap provides a region with a different index of refraction from the rest of the fiber to create two distinct boundaries for reflection. The sensors were made by Xiaohua Lei, a student from Tianjin University, at Virginia Tech. An image of a spliced fiber is shown in Figure A2, where the splice is circled.

Figure A2: Image of spliced fiber with the spliced region circled in blue.

Appendix B: Sensor Signals from Before and After Encapsulation

The optical spectra below were collected by Xiaohua Lei at the Center of Photonics Technology at Virginia Tech using the system described in Section 4.2. Sensors 1-7 were encapsulated with the Ni-based alloy and sensors 8-14 were encapsulated with YSZ. The signals collected before and after encapsulation for the Ni-based alloy samples can be found in Figure B1 and the signals for the YSZ encapsulated sensors can be found in Figure B2.

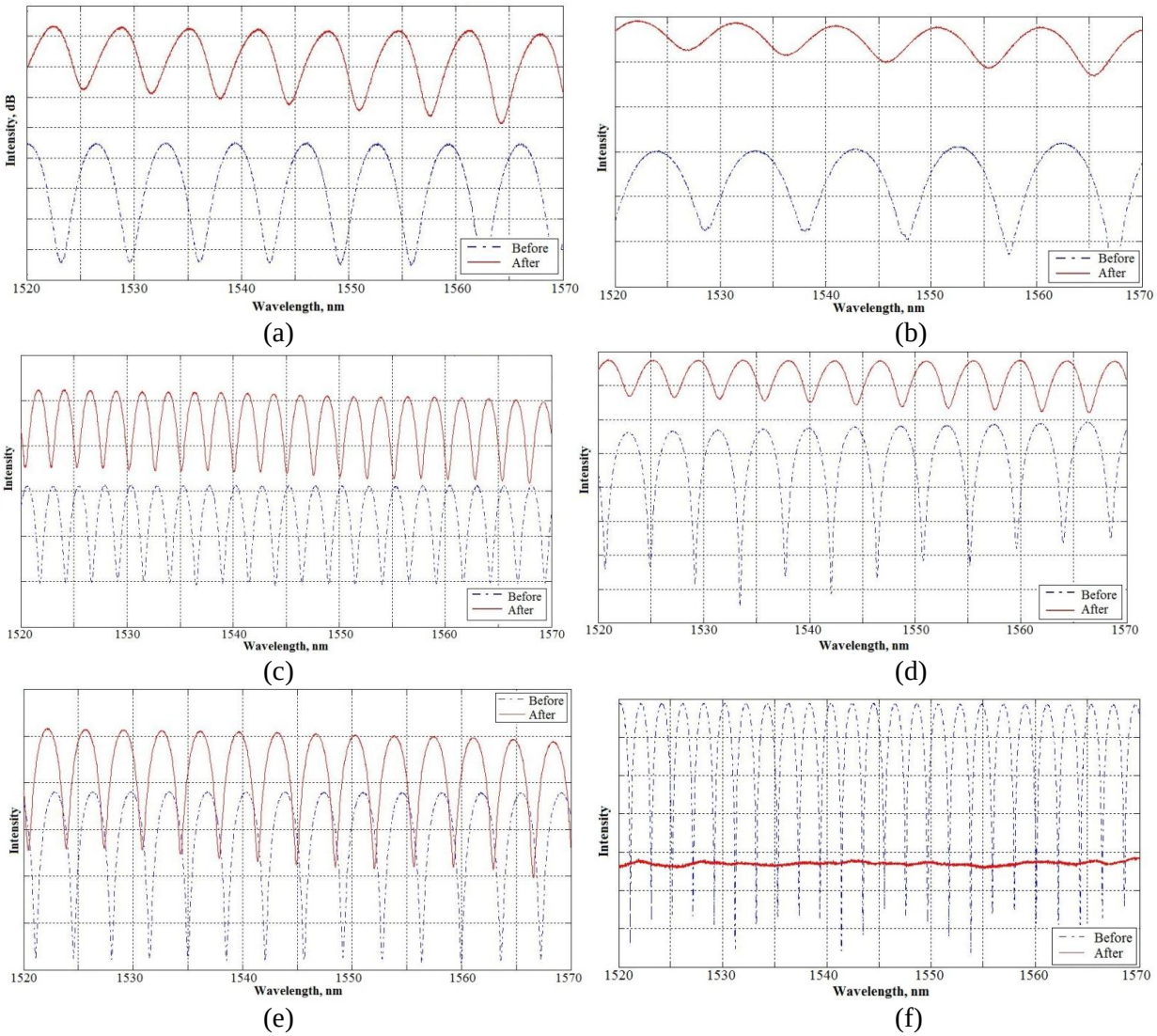

Figure B1: Spectra collected from sensors (a) #1, (b) #2, (c) #3, (d) #5, (e) #6, and (f)#7 before and after encapsulation by Ni-based alloy. Only (f) sensor #7 was broken during encapsulation.

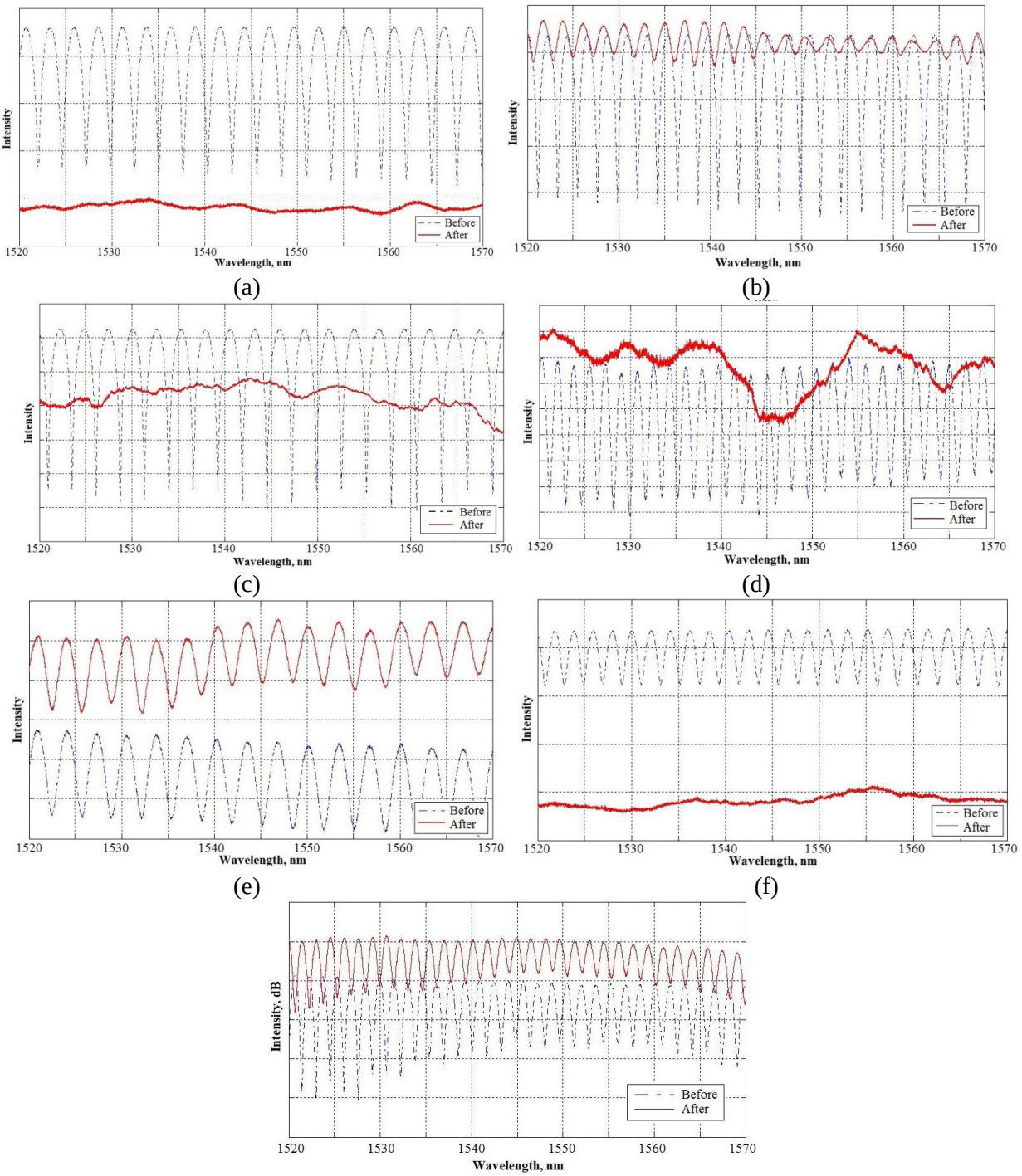

Figure B2: Spectra collected from sensors (a) #8, (b) #9, (c) #10, (d) #11, (e) #12, (f)#13 and (g) #14 before and after encapsulation by Ni-based alloy. Only sensors (e)#12 and (g) #14 remained intact after encapsulation.

Appendix C: Porosity measurements with ImageJ

The porosity was evaluated by creating binary images of each of the micrographs to identify pores. Prior to the image manipulation, the image was calibrated to the correct scale by using the number of pixels along the micron bar produced by the SEM software. The following image, Figure C1, shows the binary image produced in ImageJ from the original micrograph.

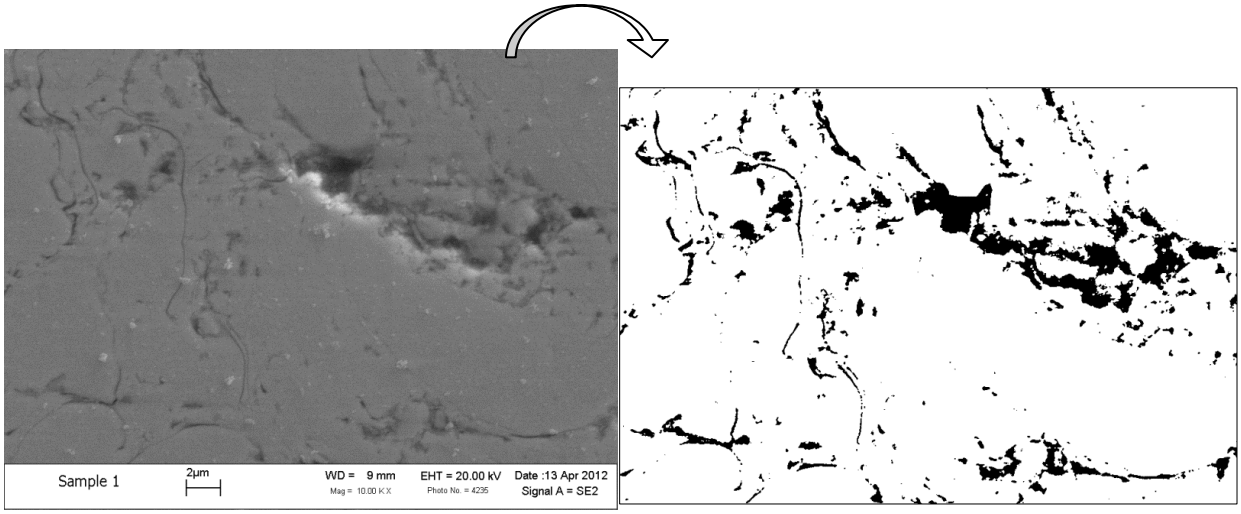

Figure C1: Micrograph of Ni-based alloy deposit taken on the SEM before and after modification to binary image in ImageJ.

The image was converted by altering the contrast to reduce the effect of shadow and noise. The grayscale threshold of the image was then altered to allow only specified shades of gray to appear as black and turn the rest of the image white. The analyze particles function in ImageJ was then utilized to measure and describe all the "particles" or black regions in the image. The function reports the particle area fraction in the image that can be interpreted as the porosity for this analysis. To avoid noise caused from shadows, all "particles" or pores that had a radius less than two pixels was deleted from the image. Images where shadows created large error in the transformation to a binary image were edited by hand by overlaying the produced binary image and the original micrograph.

Figure C1 shows that there is some error when transforming the images. Therefore, the porosity measurements have low accuracy but can provide general information about the deposits. Some error is also introduced by sample preparation effects such as particle pull out and surface contaminates covering small pores.

Appendix D: Nanoindentation – Determining Maximum Load

Previous results show that the penetration depth of an indent, determined by the maximum load, can change the mechanical properties significantly. Figure D1 shows that the change in Young's modulus and hardness from changes in penetration depth produced by a YSZ/Alumina composite coating. The chosen maximum applied load should correspond to a penetration depth that shows consistent mechanical properties.

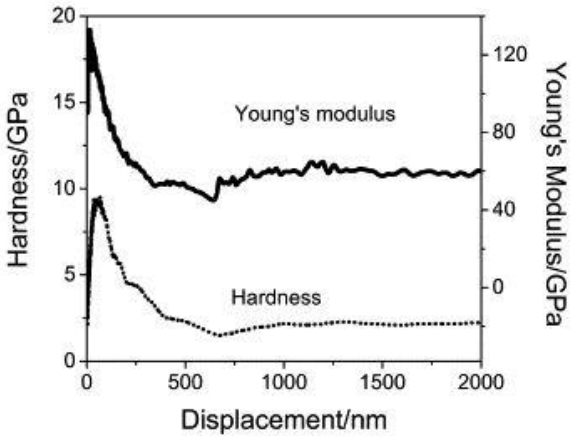

Figure D1: Measured mechanical properties as a function of the displacement of the nano-indent [63].

A YSZ deposit was tested with applied maximum loads of 20mN, 35mN, and 50mN, each at six locations. The 20mN and 50mN load indents were completed at the same location by applying the 20mN load first, removing the load, then reapplying the 50mN load. The indents can be analyzed individually since only the unloading curve and the maximum plastic displacement are used in the analysis. The 35mN maximum load indents were completed at different locations and far enough apart to avoid any edge effects. The porosity of the deposit made it impossible to find or collect images of the indents. Table D1 shows the average hardness and Young's modulus for each of the maximum applied loads.

Table D1: The mechanical properties measured for various applied maximum loads and their respective penetration depths.

Load (mN)	20	35	50
Penetration Depth (nm)	360	480	640
Hardness (GPa)	10.8±4.8	9.3±1.6	8.4±3.4
Young's Modulus (GPa)	159±30	148±18	132±26

The variation in the data is believed to be due to the porosity of the deposits. The F-test ($\alpha = 0.1$) was performed to confirm that the mechanical properties do not change with the tested applied maximum loads. The 35mN maximum applied load was chosen because all of the tested applied maximum loads are believed to produce the same mechanical properties and it provides a lower cyclic load for the indenter. The 50mN load would be causing more pressure and therefore damage the indenter tip and limit the accuracy of the measurement. The 20mN was not chosen because it may be close to the penetration depth that could cause drastic change in mechanical properties.

Appendix E: Mathematica Code to Define Material Properties

The following code, seen in Figure E1, was used to determine the temperature dependent functions used for CTE and thermal conductivity of the materials during the time dependent study.

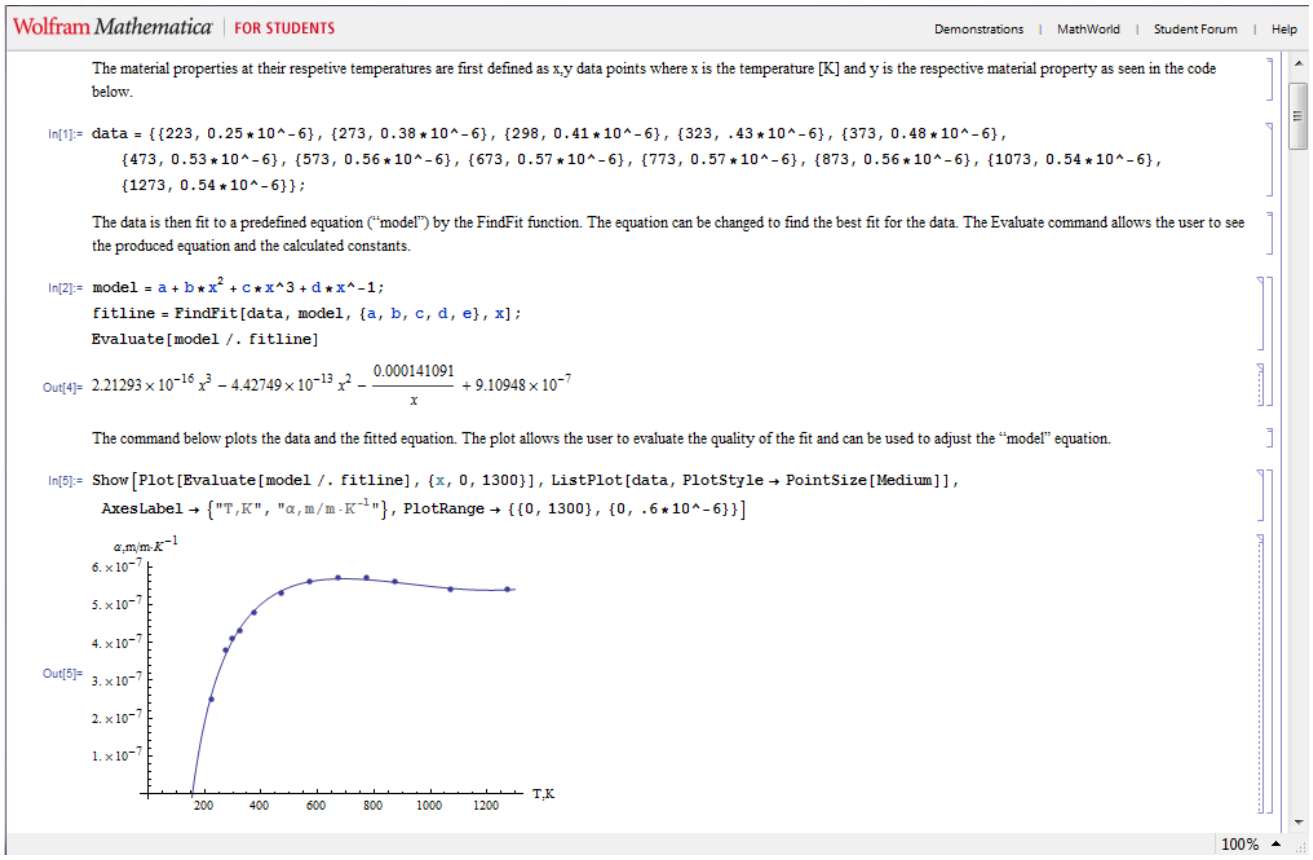

Figure E1: Mathematica window showing the code used for fitting the data.

The fit equations varied depending on the type of material and the material propert,y but the same method was employed.

Appendix F: Material Properties for Protective Tubing

The material properties can be found below, in Table F1.

Table F1: Material properties for different protecting tubes modeled.

Material	Heat Capacity, J/(kg·K)	Density, kg/m^3	Young's Modulus, GPa	Poisson's Ratio
Fused Silica	703	2203	73.1	0.17
Sialon	880	3240	288	0.25
Aluminum Nitride	740	3260	308	0.24
Alumina	880	3690	300	0.21
Hastelloy B-2	380	9220	217	0.30
Inconel 601	448	8110	207	0.27
Copper	385	8940	115	0.31
Invar 36	515	8050	141	0.29

The temperature dependent CTE and thermal conductivity equations can be found in Table F2. The equations are also a function of the temperature equation seen below Table 4.3.

Table F2: Temperature dependent properties for the different material tubes.

Material	CTE, 1/K	Thermal Conductivity, W/(m·K)
Fused Silica	$2.21x10^{-16}\cdot T^3-4.43x10^{-13}\cdot T^2-1.41x10^{-4}/T+9.11x10^{-7}$	1.38
Sialon	$3.0x10^{-6}$	17.5
Aluminum Nitride	$4.5x10^{-6}$	$(126000\cdot T)/(2.57\cdot T^2-320\cdot T)$
Alumina	$8.1x10^{-6}$	18
Hastelloy B-2	$-4.02x10^{-12}\cdot T^2+7.88x10^{-9}\cdot T+7.961x10^{-6}$	11.1
Inconel 601	$7.98x10^{-13}\cdot T^2+2.57x10^{-9}\cdot T+1.28x10^{-5}$	$-3.23x10^{-7}\cdot T^2+1.74x10^{-2}\cdot T+6.19$
Copper	$5.00x10^{-12}\cdot T^2-1.23x10^{-9}\cdot T+1.68x10^{-5}$	391
Invar 36	$4.88x10^{-11}\cdot T^2-2.66x10^{-8}\cdot T+4.51x10^{-6}$	10.2

The temperature functions were developed using the same method as described in Section 3.5.3 and Appendix E.